Thesis for the Degree of Doctor of Philosophy

Fast Microwave Tomography Algorithm for Breast Cancer Imaging

Samar Hosseinzadegan

CHALMERS

Department of Electrical Engineering
Chalmers University of Technology

Göteborg, Sweden 2021

Fast Microwave Tomography Algorithm for Breast Cancer Imaging

Samar Hosseinzadegan

ISBN 978-91-7905-449-6

Doktorsavhandlingar vid Chalmers tekniska högskola
Ny serie nr 4916
ISSN 0346-718X

Department of Electrical Engineering
Chalmers University of Technology
SE–412 96 Göteborg
Sweden
Telephone: +46 (0)31 – 772 1000
Email: samarh@chalmers.se

Front Cover: The figures on the front cover show the reconstructed relative permittivity (left) and conductivity (right) images obtained for a cylindrical phantom with the newly developed tomographic algorithm based on the two-dimensional discrete dipole approximation.

Typeset by the author using LaTeX.

Chalmers Reproservice
Göteborg, Sweden 2021

To my family

Abstract

Microwave tomography has shown promise for breast cancer imaging. The microwaves are harmless to body tissues, which makes microwave tomography a safe adjuvant screening to mammography. Although many clinical studies have shown the effectiveness of regular screening for the detection of breast cancer, the anatomy of the breast and its critical tissues challenge the identification and diagnosis of tumors in this region. Detection of tumors in the breast is more challenging in heterogeneously dense and extremely dense breasts, and microwave tomography has the potential to be effective in such cases. The sensitivity of microwaves to various breast tissues and the comfort and safety of the screening method have made microwave tomography an attractive imaging technique.

Despite the need for an alternative screening technique, microwave tomography has not yet been introduced as a screening modality in regular health care, and is still subject to research. The main obstacles are imperfect hardware systems and inefficient imaging algorithms. The immense computational costs for the image reconstruction algorithm present a crucial challenge. 2D imaging algorithms are proposed to reduce the amount of hardware resources required and the imaging time. Although 2D microwave tomography algorithms are computationally less expensive, few imaging groups have been successful in integrating the acquired 3D data into the 2D tomography algorithms for clinical applications.

The microwave tomography algorithms include two main computation problems: the forward problem and the inverse problem. The first part of this thesis focuses on a new fast forward solver, the 2D discrete dipole approximation (DDA), which is formulated and modeled. The effect of frequency, sampling number, target size, and contrast on the accuracy of the solver are studied. Additionally, the 2D DDA time efficiency and computation time as a single forward solver are investigated. The second part of this thesis focuses on the inverse problem. This portion of the algorithm is based on a log-magnitude and phase transformation optimization problem and is formulated as the Gauss-Newton iterative algorithm. The synthetic data from a finite-element-based solver (COMSOL Multiphysics) and the experimental data acquired from the breast imaging system at Chalmers University of Technology are used to evaluate the DDA-based image reconstruction algorithm. The investigations of modeling and computational complexity show that the 2D DDA is a fast and accurate forward solver that can be embedded in tomography algorithms to produce images in seconds. The successful development and implementation in this thesis of

2D tomographic breast imaging with acceptable accuracy and high computational cost efficiency has provided significant savings in time and in-use memory and is a dramatic improvement over previous implementations.

Keywords: breast cancer, microwave tomography, discrete dipole approximation, forward solver, Jacobian matrix, inverse problem, computational cost.

Preface

This is a thesis for the degree of Doctor of Philosophy at Chalmers University of Technology, Sweden.

The thesis is based on work carried out between November, 2015, and December, 2020, in the Biomedical Electromagnetics group, Division of Signal Processing and Biomedical Engineering, at the Department of Electrical Engineering, Chalmers. Professor Paul Meaney at Dartmouth College, Hanover, USA and Chalmers University of Technology, Gothenburg, Sweden, and Associate Professor Andreas Fhager at Chalmers University of Technology, Gothenburg, Sweden, have been the supervisors and examiners.

The work presented in this thesis is financially supported by a Chalmers Foundation Excellence grant.

Acknowledgments

I thank all who in one way or another contributed to the completion of this thesis. I could not have done it without your support.

First, I would like to thank my supervisor Professor Paul Meaney. You always encourage, direct, and guide me. At all times, even at Dartmouth College and under the current COVID situation, you have been available for help, guidance, and discussions, which I greatly appreciate. Your patience towards younger researchers including me is endless and definitely helped me in finding my place in this research field. Thank you for giving me the opportunity to work with you on this project. I have learned so much from you.

I also want to express my deep gratitude to my co-supervisor Associate Professor Andreas Fhager. Thank you for your constant support and feedback. I appreciate you listening to all my complaints, worries, ideas, etc. Thank you for understanding me even in the hard situations. I would like to thank Professor Mikael Persson. I truly appreciate your support and advice during my PhD studies. I also would like to thank Research Associate Shireen Geimer for fruitful discussions, and support, and for creating remarkable memories for me while visiting Dartmouth College.

I am thankful to my colleagues in the Biomedical Electromagnetics group. I would especially like to thank Hana Dobsicek Trefna, Xuezhi Zeng, Stefan Candefjord, Shantanu Padhi, Markus Johansson, and Abdullah-Al Amin. Thank you for all the nice conversations during our group meetings and the technical discussions when I needed them. I also wish to thank Ann-Christine Lindbom; thank you for all your administrative help and support when I did not know to whom my questions should be addressed. A special thanks goes to my partner-in-crime colleagues: Pegah, Tomas, Max, Morteza, Laura, and Moein. You were great company during our fika and lunch breaks and helped me enjoy myself more when studying during these years. Thanks for all the interesting conversations, encouragement to keep going, and for making the office a much better place for me.

I would like to acknowledge all the colleagues at the Electrical Engineering department. You have made Chalmers an excellent workplace for me. I would especially like to thank my antenna family: Abolfazl, Aidin, Carlo, Jinlin, Madeleine, Navid, Oleg, Parastoo, Sadegh, and Wan-Chun. Thanks for all the great memories that you created for me, especially during our fika and lunch times at work and also after work hours.

I would like thank all my Iranian friends at Chalmers for their companionship, in particular: Taha, Ebrahim, Mohammad Ali, Maryam, Fatemeh, Bita, Kamran, Alireza, Masoud, and Ahad. Thank you all for reminding me of home, when I am so far from it.

A very special word of thanks goes to my great friends, Abbas, Astrid, Sepideh, and Sina. I have shared so many moments of happiness and also sadness with you. Thank you for breakfasts, parties, and advice—you were always there with a word of encouragement or a listening ear, especially during the hard times. Given the difficult COVID situation, you proved that I can always rely on you and ask for anything.

To my dearest family. Mami and Babayi, Thank you for all your unconditional encouragement, support, and care every single day of my life. You have always been supportive of my dreams. I could not have done it without you. I am forever grateful. My sisters, Dorreh and Samane, you always listen to me with patience, offer invaluable support and care, and make me believe in myself. Thank you for being there when I needed you the most. I love you all so much.

Thank you Ramin. I can't expresses how grateful I am for your support and love. Thank you for never giving up on me and encouraging me in the hardest situations when I had no hope. Thank you for being a comfort when I needed it the most. I love you.

Samar
Göteborg, January 2021

List of Publications

This thesis is based on the work contained in the following appended papers:

Paper A
Samar Hosseinzadegan, Andreas Fhager, Mikael Persson, and Paul Meaney, "Application of Two-Dimensional Discrete Dipole Approximation in Simulating Electric Field of a Microwave Breast Imaging System," in *IEEE Journal of Electromagnetics, RF and Microwaves in Medicine and Biology*, vol. 3, no. 2, pp. 80-87, June 2019.

Paper B
Samar Hosseinzadegan, Andreas Fhager, Mikael Persson, and Paul Meaney, "A Discrete Dipole Approximation Solver Based on the COCG-FFT Algorithm and Its Application to Microwave Breast Imaging," in *International Journal of Antenna and Propagation*, vol. 2019, 2019, Art. no. 9014969.

Paper C
Samar Hosseinzadegan, Andreas Fhager, Mikael Persson, Shireen Geimer, and Paul Meaney, "Expansion of the Nodal-Adjoint Method for Simple and Efficient Computation of the 2D Tomographic Imaging Jacobian Matrix," in *Sensors*, vol. 21, no. 3, p. 729, January 2021.

Paper D
Samar Hosseinzadegan, Andreas Fhager, Mikael Persson, Shireen Geimer, and Paul Meaney, "Discrete Dipole Approximation-Based Microwave Tomography for Fast Breast Cancer Imaging," accepted for publication in *IEEE Transactions on Microwave Theory and Techniques.*

Other related publications of the Author not included in this thesis:

- **Samar Hosseinzadegan**, Andreas Fhager, Mikael Persson, and Paul Meaney, "Comparison of two forward models for electric field of microwave imaging systems," *2017 IEEE International Symposium on Antennas and Propagation & USNC/URSI National Radio Science Meeting*, San Diego, USA. 2017.

- Paul Meaney, **Samar Hosseinzadegan**, Andreas Fhager, and Mikael Persson, "Examination of the phase and log magnitude measurement projections and the implications for tomographic image reconstruction behavior," *2017 First IEEE MTT-S International Microwave Bio Conference (IMBIOC)*, Göteborg, Sweden. 2017.

- **Samar Hosseinzadegan**, Andreas Fhager, Mikael Persson, and Paul Meaney, "Integrating the discrete dipole approximation forward solver with a microwave tomography algorithm," *2018 IEEE International Symposium on Antennas and Propagation & USNC/URSI National Radio Science Meeting*, Boston, USA. 2018.

- **Samar Hosseinzadegan**, Andreas Fhager, Mikael Persson, and Paul Meaney, "On the electric field of microwave imaging systems using discrete dipole approximation," *2018 IEEE Conference on Antenna Measurements & Applications (CAMA)*, Västerås, Sweden. 2018.

- **Samar Hosseinzadegan**, Andreas Fhager, Mikael Persson, and Paul Meaney, "Optimization of a microwave tomography algorithm using the DDA as a fast forward solver," *2019 IEEE International Symposium on Antennas and Propagation & USNC/URSI National Radio Science Meeting*, Atlanta, USA. 2019.

- **Samar Hosseinzadegan**, Andreas Fhager, Mikael Persson, and Paul Meaney, "Application of the discrete dipole approximation in microwave breast imaging," *2019 International Conference on Electromagnetics in Advanced Applications (ICEAA)*, Granada, Spain. 2019.

Other publications by the Author not related to the thesis:

- Larisa Beilina, **Samar Hosseinzadegan**, "An adaptive finite element method in reconstruction of coefficients in Maxwell's equations from limited observations," *Applications of Mathematics*, vol. 61, no. 3, pp. 253-286, 2016.

Acronyms

2D	two-dimensional
3D	three-dimensional
BIM	Born iterative method
BiCG	bi-conjugate gradient
CG	conjugate gradient
CM	Clausius-Mossotti
CSI	contrast source inversion
CT	computed tomography
COCG	conjugate orthogonal conjugate gradient
COCR	conjugate orthogonal conjugate residual
DBIM	distorted Born iterative method
DCIS	ductal carcinoma in situ
DDA	discrete dipole approximation
FE	finite element
FD	finite-difference
FDTD	finite-difference time-domain
FFT	fast Fourier transform
GA	genetic algorithm
GCO	Global Cancer Observatory
GN	Gauss-Newton
IDC	invasive ductal carcinoma
ILC	invasive lobular carcinoma
ILU	incomplete lower-upper
IARC	International Agency for Research on Cancer

LCIS	lobular carcinoma in situ
LU	lower-upper
MoM	method of moments
MRI	magnetic resonance imaging
NLLS	non-linear least square
OLS	ordinary least square
OLS_{log}	logarithmic-based ordinary least square
PDE	partial differential equation
PET	positron emission tomography
PSO	particle swarm optimization
QMR	quasi-minimal residual
RMSE	root mean square error
RR	radiative reaction
rRMSE	relative root mean square error
SCBiCG	symmetric complex bi-conjugate gradient
SSOR	symmetric successive over-relaxation
TSAR	tissue sensing adaptive radar
WHO	World Health Organization

Notation and Units

Physical quantity	Symbol	SI(MKSA)
Frequency	f	hertz (Hz)
Angular frequency	ω	rad/s
Electric charge	q	coulomb (C)
Electric charge density	ρ	C/m^3
Electric current	I	ampere (A)
Electric current density	J	A/m^2
Electric potential		volt (V)
Electric field	E	V/m
Electric displacement field	D	C/m^2
Polarization	P	C/m^2
Magnetic flux	Φ	weber (Wb)
Magnetic flux density	B	tesla (T)
Magnetic field	H	A/m
Electric dipole moment	p	$\mathrm{C}{\cdot}m$
Green's function	G	m^{-3}
Polarizability	α	m^3
Free-space permittivity	ϵ_0	$8.854{\times}10^{-12}$ $\mathrm{C/V}{\cdot}m$
Inductance		henry (H)
Free-space permeability	μ_0	$4\pi \times 10^{-7}$ H/m
Conductance		siemens (S)
Conductivity	σ	S/m
Wavenumber	k	$1/m$

Contents

Part I

Introductory Chapters

Chapter 1

Introduction

1.1 Problem description and motivation

Cancer is recognized as a dominant cause of fatalities worldwide, accounting for an estimated 9.6 million deaths in 2018 [1]. The World Health Organization (WHO) has reported breast cancer as the most common cancer in women. WHO has also recently noted a growth in breast cancer cases due to contemporary lifestyles. Implementation of prevention policies together with early detection has been found highly effective in reducing the cancer burden [1]. Many cancers are curable if they are diagnosed in the early stages and treated while the tumors are small [1]. The key to increasing the chance of survival in breast cancer is regular monitoring [2, 3].

Conventional imaging technologies suffer from several drawbacks, and improving state-of-the-art imaging techniques or introducing new screening technologies is needed for more exact detection. X-ray mammography is the golden standard for breast screening, but it suffers from a relatively high rate of false negatives; i.e., tumors are present in the breasts but not detected. The rate of false positives is also high [4, 5]. Moreover, the use of ionizing X-rays constitutes a small potential risk of inducing cancer.

In today's care, breast imaging is usually performed for detection, diagnosis, and progression monitoring. For breast cancer imaging applications, the devices should be designed to be portable, cost effective, sensitive to various tissue types, user-friendly, harmless and comfortable for patients [6]. Microwave technology has a great potential to meet these requirements, but it is still being developed, and has not yet been fully translated to the clinical setting. The benefit of a non-ionizing technique that does not require breast compression is particularly appealing for patient safety and comfort. Besides, microwaves show a high level of sensitivity to even small tumors and have demonstrated a good ability to distinguish malignant and benign tumors [7, 8]. Compared to the other methods such as magnetic resonance imaging (MRI) and nuclear medicine, microwave imaging is a low-cost alternative [6]. Despite the

potential held by microwave imaging, there are still no convenient and fast imaging devices available at clinics. Developing such imaging devices will require developing a fast and accurate electromagnetic solver.

Breast imaging with microwaves can be done in two different ways: either imaging of patterns and shapes (qualitative imaging) or imaging of dielectric properties and their spatial distribution (quantitative imaging). The qualitative imaging methods are usually less complex in terms of modeling and computations, but they are not as informative as quantitative images. In breast imaging, shape and position as well as the physical properties of tumors are of interest since all three contain information that is useful for discrimination between malignant and healthy regions.

Microwave tomographic imaging is categorized as quantitative imaging. The internal structure of the breast is imaged in the form of spatial maps of permittivity and conductivity values. A major challenge for microwave tomography is inherited from the physics of the electromagnetic scattering problem. First, the inverse problem (recovering the unknown parameters from the data) is ill-posed and requires a regularization procedure [9]. Second, due to the high contrast variations of the dielectric properties of breast, tumors, and the surroundings, multiple scattering phenomena occur, resulting in a non-linear problem [10]. Non-linear reconstruction algorithms require large computational resources and increase the computational cost significantly, particularly for three-dimensional (3D) imaging. Consequently, two-dimensional (2D) models and reconstruction algorithms become more attractive. In general, a priori information can be used to encourage global convergence, but the absence of such information in breast imaging presents a third challenge [11].

These well-known obstacles associated with tomographic imaging systems and algorithms have delayed adoption of this new imaging modality. Accomplishing this goal will require a continued and substantial attention to both hardware and software components of microwave imaging technology.

1.2 Breast cancer overview

Cancer is a group of diseases caused by an uncontrolled cell-growth of normal body cells due to mutations (changes to a cell's DNA) in genes. These mutations interfere with regulation in the cell and cause irregular and chaotic cell division. The result is a massive growth of cells which eventually transforms into a tumor.

Female breasts are made of fatty, fibrous, and glandular tissue. The anatomy of a healthy breast is shown in Figure 1.1.a . Breast cancer tumors form mainly in the fibroglandular tissue, including the lobules and the ducts. In addition, fatty tissue (adipose) within the breast can also be involved [12,13]. Figures 1.1.b-c and 1.2 show cancer formed in various parts of the breast. Although it's rare, men can also be diagnosed with breast cancer.

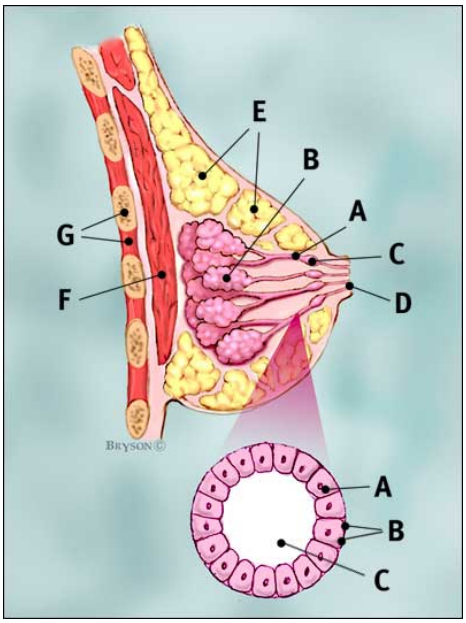

(a) Anatomy of a healthy breast

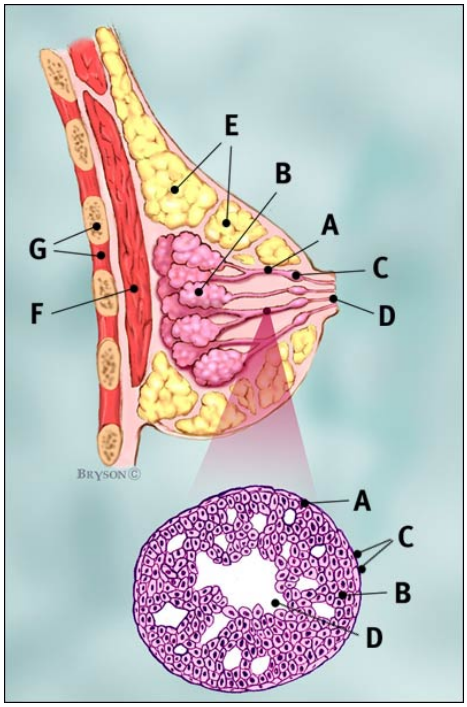

(b) Normal breast with non-invasive ductal carcinoma in situ (DCIS) in an enlarged cross-section of the duct.

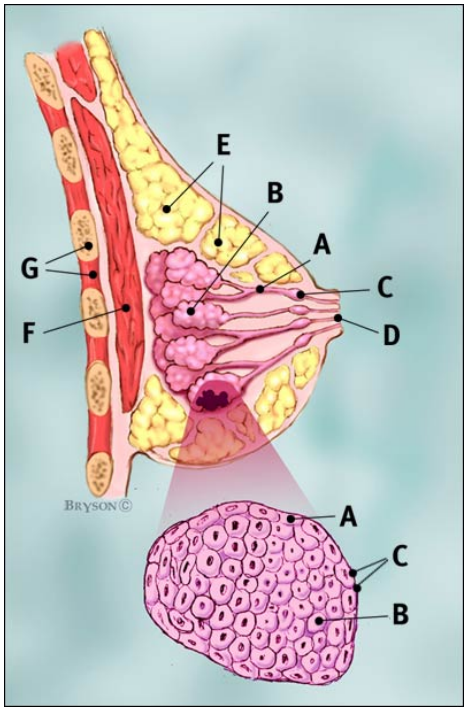

(c) Normal breast with lobular carcinoma in situ (LCIS) in an enlarged cross-section of the lobule.

Figure 1.1: Used with permission from Breastcancer.org [14]

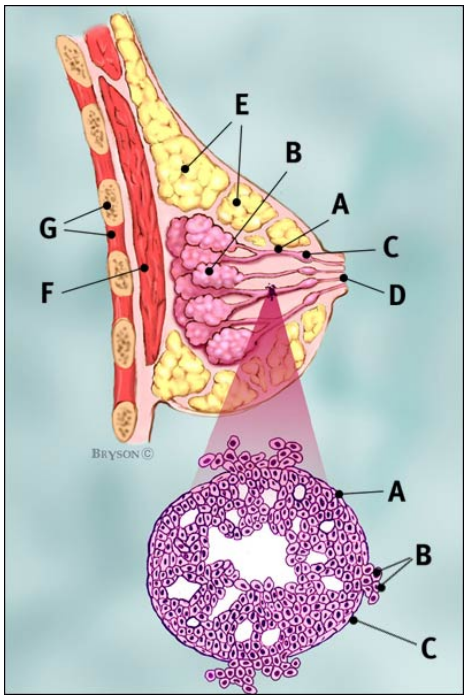

(a) Normal breast with invasive ductal carcinoma (IDC) in an enlarged cross-section of the duct.

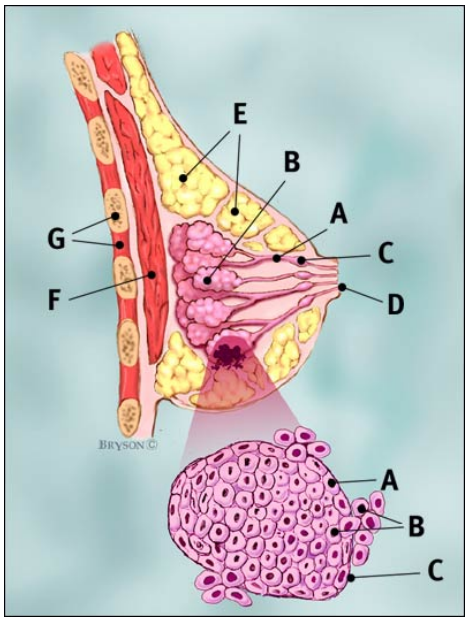

(b) Normal breast with invasive lobular carcinoma (ILC) in an enlarged cross-section of the lobule.

Figure 1.2: Used with permission from Breastcancer.org [14]

1.2.1 Classification

Breast cancer types are mainly categorized according to their growth patterns and location. They are categorized as either invasive or non-invasive (in situ). These two main categories are divided into subcategories based on the location within the breast as [15]:

- Ductal carcinoma in situ (DCIS)
- Lobular carcinoma in situ (LCIS)
- Invasive ductal carcinoma (IDC)
- Invasive lobular carcinoma (ILC)

Figures 1.1 and 1.2 show the four most common breast cancer types together with the anatomy of a healthy breast. Among these types, the most common type is the invasive ductal carcinoma (IDC), which initially forms in ducts and in later stages invades the surrounding tissues, shown in Figure 1.2.a. Furthermore, breast cancer is staged based on the spread of the tumor from 0 to 4, where stage 0 refers to non-invasive, in situ, i.e., a tumor that is localized to its original location. In stage 4, the tumor has metastasized to nearby tissues as well as possibly to distant organs including lungs, brain, liver, or bones [16].

1.2.2 Risk factors

The incidence and mortality patterns are an indication of risk factors. According to the study performed by P. Maisonneuve [17, 18], breast cancer risk factors can be divided into three main groups: 1) demographic, lifestyle, and environmental, 2) reproductive and hormonal, and 3) genetic.

The two main factors in the first group are age and race/ethnic group. Breast cancer is common in women over the age of 50 and its incidence increases until age 70 and then decreases [17, 18]. Breast cancer rates are also higher among White women compared to Black women. Moreover, the incidence is lower among those of Asian and Pacific Islander origin [17, 18]. In addition to age and race/ethnic group, other demographic and lifestyle factors such as obesity, diet, and physical activity can also affect breast cancer risk. One illustrative case is presented in Figure 1.3, which shows that a non-negligible number of cases of postmenopausal breast cancer could have been prevented if the body mass of women, at the population level, remained constant throughout their life time. Breast cancer risk is also related to reproductive and hormonal changes, such as menarche, pregnancy, breastfeeding, etc., and the age at which these take place. These changes stimulate cell growth and consequently affect the risk of breast cancer. Women with a parent, sibling or off-spring diagnosed with breast cancer are more likely to develop breast cancer [17, 18].

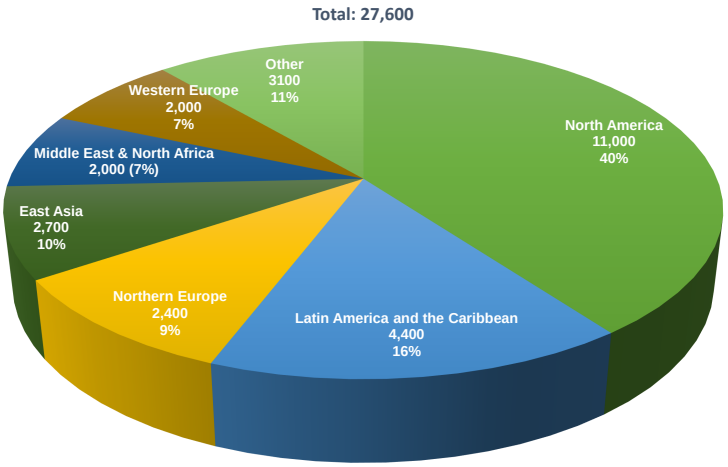

Figure 1.3: The postmenopausal breast cancer cases among women in 2012 that could have been prevented if mean population-level body mass index values had remained constant since 1982 by region and percentages of all such preventable postmenopausal breast cancer cases. Image generated from data available at GLOBOCAN 2018, IARC.

1.2.3 Statistics

Global breast cancer statistics are reported by the Global Cancer Observatory (GCO) [19] through the platform GLOBOCAN maintained by the International Agency for Research on Cancer (IARC) [20]. Breast cancer is the most common type of cancer among women; with a 24% share of all cases, see Figure 1.4a. This disease also kills more women than any other cancer, constituting about 15% of all cancer deaths among women per year, see Figure 1.4b. Furthermore, the breast cancer incidence is expected to increase by about 46 % over 20 years [19]. This implies that the number of new cases and deaths will grow rapidly in the near future and emphasizes the need for prevention strategies and early detection.

Figures 1.5 and 1.6 present the comparison of the breast cancer incidence and mortality rates for women worldwide. In these figures, the darker colors correspond to higher incidence/mortality rates. It is notable that even though the highest incidence rates occur in the industrialized world including North America, Australia, Northern and Southern Europe, the highest mortality rates are found in developing regions such as Africa. These data illustrate that mortality rates could be reduced with improved economic development and a corresponding expansion of welfare and health care sectors. However, lack of public healthcare in some of the developing regions might be a reason why cancers can remain undetected and therefore not appear in any statistics. Data from these countries are therefore prone to high uncertainties. Other factors such as genetics can also impact the incidence and mortality rates.

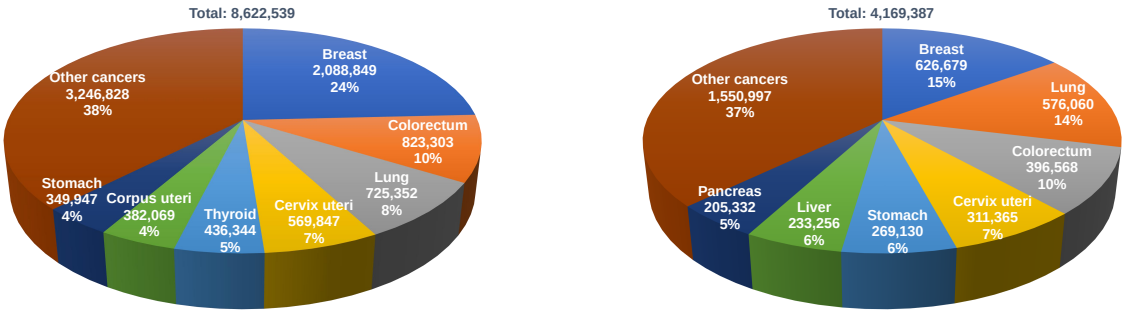

(a) (b)

Figure 1.4: Estimated number of a) new cancer cases and b) cancer deaths worldwide for females in 2018. Images generated from data available at GLOBOCAN 2018, IARC.

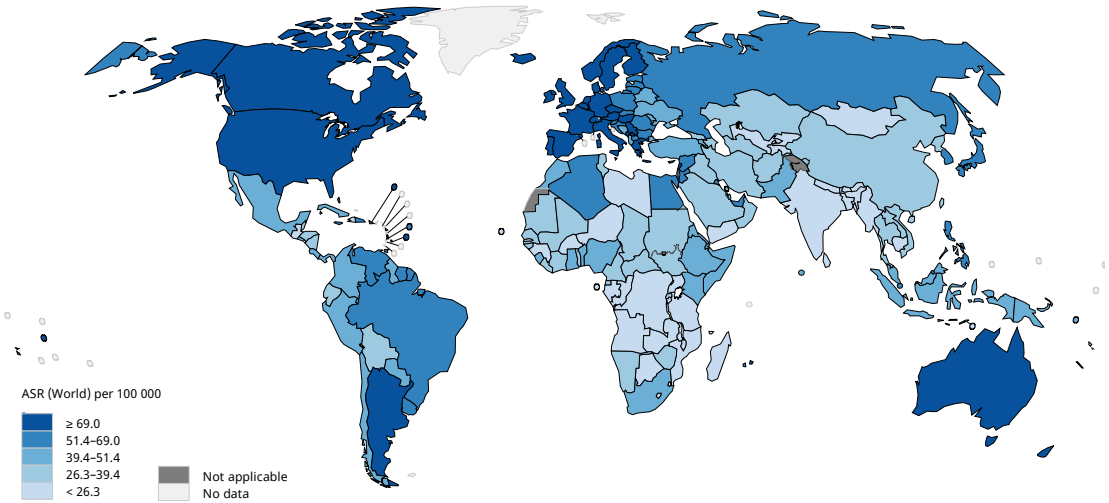

Figure 1.5: Estimated age-standardized incidence rates for 2018 worldwide for female breast cancer in all ages. Image reprinted from GLOBOCAN 2018, IARC.

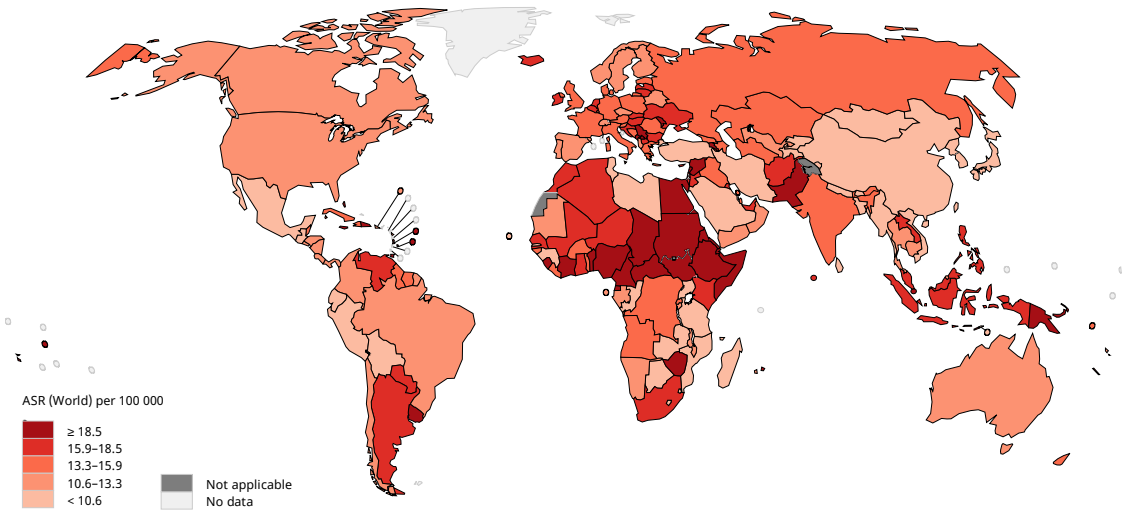

Figure 1.6: Estimated age-standardized mortality rates for 2018 worldwide for female breast cancer in all ages. Image reprinted from GLOBOCAN 2018, IARC.

1.3 Technologies for breast imaging

Early detection of breast cancer is the key to increasing the chance of survival [21–25]. Two major studies regarding the impact of regular breast monitoring were done in Sweden in 1985 [22] and 1993 [26], followed by more recent studies [23, 24]. In Tabár et al. [22], a randomized controlled trial was done on 162, 981 women ages 40 and above for about 8 years. The objective was to investigate if mass screening with mammography reduces the mortality due to breast cancer. The enrolled population was divided in two randomized groups: study and control. The women in the study group were offered screening every 2 or 3 years, depending on age. Women in the control group were not offered screening. In this study, they concluded that there was a 31% reduction in mortality from breast cancer. In addition, the rate of advanced breast cancers in the study group was reduced by 25%. Nyström et al. [26] also proved the effect of regular mammography in reducing mortality. This study explored the impact of screening on breast cancer mortality for all age groups. The largest reduction of breast cancer mortality (29%) was observed among women ages 50-69; other age groups were also found to benefit from regular screening but to a lesser extent.

Breast imaging is usually performed for detection, diagnosis (after the clinician has seen an abnormality in a mammogram), and tumor progression monitoring during treatment. Conventional imaging techniques include X-ray-based mammography screening, computed tomography (CT scan), MRI, and positron emission tomography (PET scan). In addition, newer techniques such as digital breast tomosynthesis, contrast mammography, and contrast-enhanced MRI can be used in both screening and

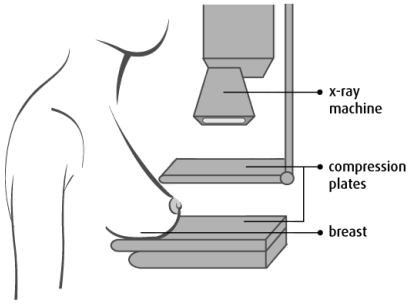

Figure 1.7: Imaging system for mammography. Image reprinted from [28].

diagnosis [18, 27]. Currently, the primary method for routine breast cancer screening is X-ray mammography.

1.3.1 Mammography

In mammography, the patient stands in front of the equipment such that her breast is placed on a flat plate and another plate compresses the breast, as shown in Figure 1.7. During the examination, X-rays are radiated through the breast and captured by a detector located on the opposite side. The operating principle for mammography is based on imaging of the contrast between various tissue types within the breast as a grey-scale image, i .e., low-density tissue such as fat appears darker on the image and higher density tissue such as tumor produces a lighter region in the image. This type of image is called a mammogram. A standard mammogram constitutes two-dimensional projections of the breast from two different angles, craniocaudal (CC: top-bottom view) and mediolateral oblique (MLO: side view at a specific angle). Additional CC views or spot compression can be performed in cases where an abnormality is identified. This technique requires firm and even compression to ensure optimal exposure and maximize image resolution and contrast. Unfortunately, many patients consider mammography uncomfortable and painful.

Rosenberg et al. [29] investigated mammography sensitivity (the true positive rate, i.e., the number of true positives divided by the sum of true positives and false negatives) based on a database of 183, 134 screening mammograms. The authors concluded that sensitivity varies significantly with ethnicity, use of estrogen replacement therapy, mammographic breast density, and age. Specifically, sensitivity was most notably reduced in women younger than 40 years with dense breasts. Another study, performed by Berg et al. [30], showed that mammography had an accuracy (the sum of the true positives and true negatives divided by the study population) of about 70.2%, with 67.8% in sensitivity (i.e., true positive rate) and 75% in specificity (i.e. true negative rate), respectively [30]. Distracting lesions and breast density are primary confounding features for missing a breast tumor. Moreover, due to the

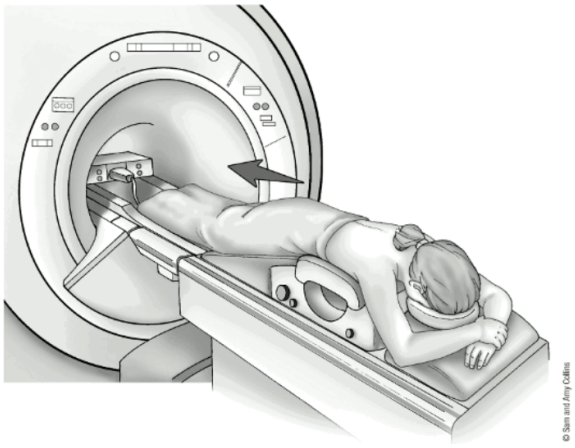

Figure 1.8: MRI device. Image reprinted from [32].

radiation exposure, young women are sometimes not screened regularly because of the risk/benefit trade-off.

1.3.2 Magnetic resonance imaging (MRI)

In MRI, the patient is positioned inside a large magnetic tunnel and exposed to magnetic fields, see Figure 1.8. MRI utilizes the fact that the human body is mainly composed of water (H_2O) and fat, which both contain hydrogen atoms (protons). The protons spin around their axes randomly in nature, but when they are exposed to a magnetic field they align with it. After alignment, an RF-coil emits radio frequency pulses which cause proton spins to flip. When the radio pulse is turned off, proton spins relax and re-align with the magnetic field. The relaxation rates as well as the amount of released energy provide information about the tissue types [31].

MRI is an option for breast imaging and is mostly used as a complement to mammography for further evaluation of suspicious findings. One of the advantages of MRI over X-ray mammography is that it is insensitive to normal dense breast tissue [33]. However, it is used with a gadolinium contrast agent which can be toxic to women with compromised kidneys [34]. The contrast agent accelerates the relaxation process and results in an image where the lesions are easier to identify. This technique is frequently used for screening and diagnosing young women. MRI is, however, significantly more expensive than other imaging methods and is therefore not suitable for use in mass screening. Another problem is a high rate of false positives, which leads to over diagnosis in screening [33, 35, 36].

1.3.3 Ultrasound

During an ultrasound examination, the patient is in the supine position. A small probe called a transducer is placed directly on the skin and is used to produce the

images. The probe sends high-frequency sound waves into the breast, and it also records the reflected echoes for further processing and image generation [37]. Ultrasound screening can be used as a complement to both X-ray mammography and MRI. One caveat about ultrasound screening is that its precision is highly operator-dependent, which introduces considerable risk of errors in the diagnosis. It is also known to have a high number of false positives. Berg et al. [38] investigated the impact of combined screening with ultrasound and X-ray mammography, compared to X-ray mammography alone. In that study, they concluded that while ultrasound may reveal small and node-negative breast cancers not visible in mammography, the increased number of false positives is significant [38].

1.3.4 Computed tomography (CT)

During breast CT scanning, the patient lies in the prone position as a scanner rotates around the breast. A CT scanner encircles the body and creates an image from measured X-ray projections at a large number of angles. The measured projections are processed to create cross-sectional images of the body and produce gray-scale images [39]. CT scanning is usually not used for screening, but for investigations of patients who have already been diagnosed, for example in order to detect metastasis in nearby tissues, such as the chest [39]. The main reason for not using CT in screening is to avoid unnecessarily high doses of X-ray exposure.

1.3.5 Positron emission tomography (PET)

PET scanning reveals tissue function by showing metabolic activity. In this method, a radioactive sugar is injected into the patient. Its decay produces radioactivity that is measured outside the body with detectors encircling the body. This imaging technique is mostly used during treatment planning since the metabolic activity frequently reveals changes during treatment before morphological changes such as tumor size can be seen [18, 40–42]. PET imaging is usually combined with other imaging modalities to be more informative. Similar to X-ray CT, PET scanning is also not completely harmless and not recommended for regular screening.

The aforementioned drawbacks in conventional imaging techniques illustrate the need and room for developing new image acquisition techniques to further improve diagnosis. Microwave imaging appears to be a promising technique for this situation. The technology is harmless, non-invasive, cost-effective, convenient for the patient, and sensitive enough to various tissue types. These characteristics make it an intriguing candidate to complement or replace other modalities.

1.4 Microwave imaging: status and challenges

Microwave imaging uncovers information about an invisible object. The information could be just position, shape, and size, or also include dielectric properties. The recovered information about an object varies by application. The interests range from detection and localization of the object to its full reconstruction, which usually engages its physical properties. The operating principle is based on transmitting electromagnetic waves through the object and then measuring and processing the forward and scattered waves at limited observation points. For biomedical purposes, the most common interest is to completely image the electromagnetic parameter distributions (i.e., dielectric permittivity, electric conductivity) of the tested objects [43].

Microwave imaging has been studied for multiple applications over recent decades. These applications range from medical diagnosis, e.g., breast imaging [44–46], brain imaging [47–49], kidney imaging [50], cardiac imaging [51], and bone density measurements [52] to other fields including geophysical monitoring [53], civil engineering [54], and industrial engineering [55]. Microwave imaging for medical applications has been investigated since the 1970s. One of the earliest medical microwave imaging systems was introduced by Larsen and Jacobi, who used microwave signals to image canine kidneys [50, 56]. From the 1970s until now, multiple imaging systems have been built, and their drawbacks and limitations have been investigated extensively. Although several clinical trials have been conducted, this imaging technique has not yet been widely transferred to clinical practice or deployed for regular use in healthcare. Microwave imaging systems used for biological tissues suffer from signal power loss, limited penetration depth, low resolution, and a need for enormous computational resources [57]. Additionally, the physics of the inverse scattering involves the non-linearity and ill-posedness of Maxwell's equations. Aside from these known challenges, medical microwave imaging has been introduced as an alternative or complement to conventional imaging systems such as mammography.

As mentioned, microwave imaging methods can be divided into at least two categories, qualitative and quantitative, based on the recovered information and content of the output image. In qualitative imaging methods, the reconstructed information is restricted to location, size, and shape of the object. One advantage of these methods is their computational efficiency and short reconstruction time. A disadvantage is that they require broad band measurements [58, 59]. This could lead to longer measurement times depending on the techniques used. Conversely, quantitative imaging methods aim at reconstructions of dielectric maps of the tested object. These methods are known to be computationally demanding and in many implementations restricted to cases where a priori information about the object is available (see Chapter 5 in [43]). Qualitative methods that have been researched include holography and radar-based imaging. Quantitative methods are usually refered as tomography.

Multiple radar-based systems have been developed and tested in both experiments and clinical settings, and their fundamental operating principle is based on the differences between dielectric properties of healthy and malignant tissues over the microwave frequency range. In active radar-based imaging, the target is illuminated by signals transmitted and received by an array of antennas. Data are also acquired in multiple planes and are simultaneously processed to produce the whole 3D image via a reconstruction algorithm [57]. The operating principle is based on transmission and reception of pulses. Short high-energy pulses are transmitted and the returning echoes are recorded. The more recently developed radar-based imaging systems include the Tissue Sensing Adaptive Radar (TSAR) at the University of Calgary [46], the MARIA system [60] at the University of Bristol, the McGill University system [61], and the Wavelia system by MVG industries [62].

Another microwave-based imaging technique, microwave holography, has also been used to image dielectric targets [63]. This technique is relatively new in the field of medical imaging but has been employed to detect concealed weapons and contraband at airports and other secure locations [64]. In modern microwave holography, coherent back-scattered signals are acquired on a surface, and the reconstruction is performed through multiple direct and inverse Fourier transformations. Unlike in tomography, the reconstructions are not typically done in 2D slices. The measured data from the surface is processed into a 3D distribution of the target [63, 65]. The system developed at McMaster University belongs to this category [63].

Microwave tomography utilizes scattered electric field data from an object to reconstruct quantitative maps of the property distributions, usually permittivty and conductivity. For breast cancer detection, this technology aims at imaging the differences in properties between healthy and malignant tissues. Systems typically operate in the frequency range of 500 MHz - 3 GHz. Microwave tomography is under development and has reached the stage of clinical trials in some cases [44, 52]. Historically, the large contrast in the properties of different biological tissues has been a major barrier in microwave tomography [66, 67]. A number of methods and algorithms have been investigated by multiple research groups since the possibility of employing microwave signals for medical imaging was first studied [44, 68–70]. Despite the focus on these algorithms, they have scarcely been translated into the real world. This is principally due to the low efficiency of various numerical methods and the presence of a high contrast among different tissue types [71, 72]. Imaging-system design and improvements in measurement accuracy can contribute to future success or usefulness of microwave tomography. Moreover, in medical imaging, high sensitivity and specificity are desirable, and these characteristics generally narrow the choice of algorithm.

Computation times and imaging costs present a challenge in microwave tomography. Multiple research groups have worked on reducing the cost while producing acceptable imaging; their attempts include research on the hardware part of the

imaging system, i.e., contributions in system design and also in developing efficient algorithms, i.e., in the mathematical formulation of the forward and inverse problems. The choice of 2D or 3D algorithms impacts the computational cost and whether the tomographic imaging is feasible in real time. Previously, Grzegorczyk at al. [73] successfully employed the 3D discrete dipole approximation (DDA) for fast breast imaging in under 20 minutes. This has inspired our further studies using the 2D DDA to enable additional reductions in reconstruction times. The imaging system used in this thesis has previously been shown to work particularly well with 2D imaging algorithms. Although a majority of studies presently focus on 3D imaging, in this thesis, we show that 2D imaging based on the DDA is a good solution to further decrease the computational burden without sacrificing accuracy. More details justifying the choice of 2D imaging will be given in the following chapters.

1.5 Image reconstruction in microwave tomography

The microwave tomographic reconstruction algorithms include two problems, the forward and inverse. The forward problem is to find the electromagnetic field distributions when the dielectric properties in the domain are known. The inverse problem is to recover a hidden object with respect to its position, shape, and dielectric properties in the domain when limited observations at the boundary of the domain are made through forward solutions. The inverse problem is, in the general case, an iterative process and therefore requires calculation of forward solutions at each iteration. In this way, the forward solver and its computational complexity has a significant impact on the overall computational burden of the inverse solver and should be addressed. Additionally, the inverse problem is ill-posed due to the large property contrasts among tissues and is also non-linear. Therefore, computationally expensive iterative optimization algorithms are required. The forward and inverse problems are further discussed in the next chapters.

1.6 Properties of breast tissue in microwave region

In the context of breast imaging, breast tissues are typically categorized as normal or tumorous. Normal tissue comprises adipose (mostly consisting of fat) and fibroglandular tissue. Tumorous tissue is further classified as benign or malignant. The dielectric properties of these tissues vary in the microwave frequency region and create a contrast between tissues that enables imaging of the breast.

Multiple studies have been conducted to determine the dielectric properties of normal and tumorous breast tissues. One early study by Chaudhary et al. in 1984 investigated the dielectric properties of normal and malignant tissues for 15 patients

in the frequency range of 3 MHz to 3 GHz [71]. In the same decade, Surowiec et al. [74] studied the dielectric properties of normal and malignant tissues for 7 patients in the frequency range of 20 kHz to 100 MHz. Later, other research groups conducted small studies of these tissues in various frequency ranges [75–77]. In 2007, Lazebnik et al. [7] performed ex vivo studies of the dielectric properties of adipose, glandular, and malignant tissues in 196 patients in a broad frequency range of 500 MHz to 20 GHz. Martellosio et al. [78, 79] and Sugitani et al. [80] have also reported on these properties. More recently, Cheng et al. [8] reported on the properties for a large number of samples. To the best of our knowledge, the latest study is that by Hussein et al. in 2019 [81].

Figure 1.9 shows a summary of various research groups' reports on the dielectric properties of breast tissues. We note that Rydholm [82] re-produced the figure based on the fact that, since different breast densities are reported in [7, 79], the low densities have been grouped together with adipose tissue of other studies and the high densities are grouped together with the fibroglandular tissue [82], and normal tissue studied by Cheng et al. [8] contain both adipose and fibroglandular tissue. The reported properties differ from each other. Even if the exact numbers vary among the studies, the general conclusion is that the dielectric properties of breast tissues vary significantly and that this contrast can be used to map the dielectric properties of this region.

1.7 Aim of the thesis

The thesis focuses on the microwave tomography technique for breast cancer detection. It is devoted to investigating the computational aspects and to addressing the heavy computational burden of microwave tomographic reconstruction algorithms. The thesis investigates a new forward solver, i.e., the 2D discrete dipole approximation (DDA). A mathematical formulation is developed and adapted for modeling the imaging systems at Chalmers University of Technology in Sweden and Dartmouth College in the U.S. More specifically, the 2D DDA is developed and studied for inhomogeneous and lossy media. In particular, the accuracy and computational complexity have been studied and optimized. The thesis also investigates an inverse solver and image reconstruction. A 2D reconstruction algorithm is developed based on the DDA forward solver and a log-magnitude and phase formulation of the optimization problem. The tomographic algorithm is tested and validated with data from several simulation studies and phantom experiments. In order to obtain the greatest possible increase in the speed of the reconstruction algorithm, both the forward solver and the Jacobian matrix computation are optimized to minimize the computational burden. As a result, the overall computational complexity of the reconstruction algorithm is significantly reduced, and a substantial speed-up is obtained. The thesis concludes that the tomographic microwave images with a high level of accuracy can

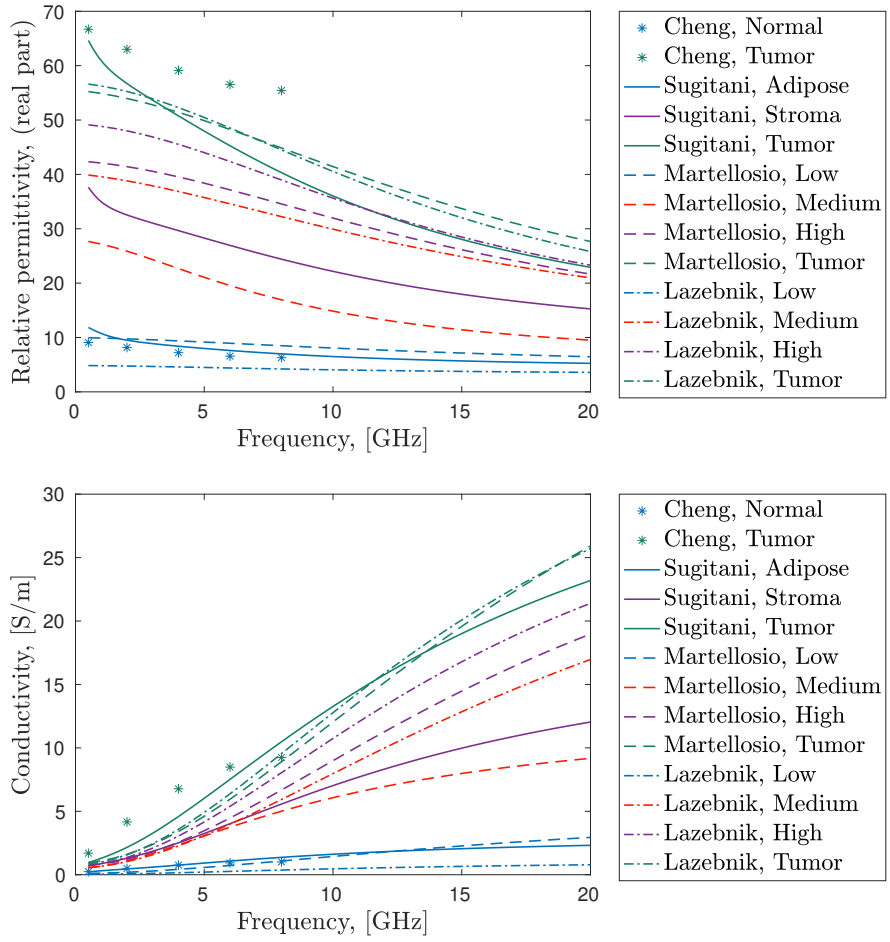

Figure 1.9: Dielectric properties as reported in different studies:(a) relative permittivity and (b) conductivity. Figure reprinted with permission from [82].

be obtained in real-time when accurate and effective solvers are combined with our imaging systems.

1.8 Thesis outline

The thesis contains two parts. Part I introduces the problem, provides the background, discusses the research area, and presents the overall results. Part II contains the main contributions by the author in the form of appended papers.

Part I has 6 chapters. Chapter 1 focuses on the problem, provides background for a better understanding, states the aim of thesis, and highlights the contributions of the author. Chapter 2 gives an overview of the forward problem, specifically the 2D DDA numerical solver for the breast microwave tomography system. Chapter 3 presents an overview of the inverse problem and discusses the log-magnitude and phase reconstruction algorithm as well as the Jacobian matrix employed in the image reconstruction algorithms. Chapter 4 discusses the general challenges facing microwave breast imaging systems and describes the microwave breast imaging systems available at Chalmers University of Technology and at Dartmouth College. Chapter 5 gives a summary of the appended papers in Part II. Chapter 6 concludes the thesis and discusses possible directions for future work.

1.9 Contributions of the author

This section states the contributions of the author to the appended papers.

- **Paper A**: The author developed the 2D DDA method, implemented 2D DDA, performed the simulations and measurements, and took the main responsibility as a lead author in writing the paper.
- **Paper B**: The author formulated the 2D DDA combined with the fast Fourier transform (FFT), implemented 2D DDA-FFT, did the analysis and simulations, and took the main responsibility as a lead author in writing the paper.
- **Paper C**: The author implemented the Jacobian matrix for the 2D DDA and performed the simulations related to the 2D DDA method. The first and last authors of the paper contributed equally in writing the paper.
- **Paper D**: The author implemented the 2D DDA-based image reconstruction algorithm, performed the simulations and measurements, and took the main responsibility as a lead author in writing the paper.

Chapter 2

Forward Problem

Solving the forward problem in electromagnetics requires a thorough understanding of the subject. This chapter reviews theories used in the modeling and formulation of the forward problem in the microwave tomographic algorithms.

2.1 Overview

The forward problem models the electromagnetic field in a specific domain with known dielectric parameters and initial and boundary conditions. For image reconstruction, the forward solution has to be recalculated at each iteration. The bulk of the computational need is therefore due to the forward problem. Accordingly, the formulation of the forward problem and its computational complexity constitute a notable degree of importance for actual medical imaging applications. One computational challenge in image reconstruction is the accurate modeling of the field distributions for the dielectric property distributions within reasonable computation times. The amount of computational resources required for a 3D reconstruction algorithm is exceptionally great in comparison to 2D algorithms. Consequently, some medical microwave tomography research groups have concentrated on 2D tomography, and 3D modeling has largely only been used in simulations, with a few clinical applications. In this thesis, a 2D microwave tomographic algorithm is implemented, and this chapter is devoted to the first important part of a tomographic algorithm, i.e., the forward solver.

2.2 Electromagnetic field theory

Maxwell's equations characterize the physical interactions among fields, fluxes, and material properties in an environment. The complex form of these equations in the

frequency domain is written as

$$\nabla \times E = -j\omega B \tag{2.1}$$
$$\nabla \times H = J + j\omega D \tag{2.2}$$
$$\nabla \cdot D = \rho \tag{2.3}$$
$$\nabla \cdot B = 0 \tag{2.4}$$

where ∇ is curl of a vector field, E is the electric field, B is the magnetic flux density, H is the magnetic field, D is the displacement field, J is the current density, ρ is the electric charge density, ω is angular frequency, and j is the imaginary unit. The following constitutive relationships can be used to replace fields and fluxes:

$$J = \sigma E \tag{2.5}$$
$$B = \mu H \tag{2.6}$$
$$D = \epsilon E \tag{2.7}$$

where σ is the electrical conductivity, $\epsilon = \epsilon_0\epsilon_r$ is the permittivity, which can also have a complex value in the form $\epsilon = \epsilon_0\epsilon_r + \frac{\sigma}{\omega j}$, and $\mu = \mu_0\mu_r$ is the permeability; ϵ_0 and μ_0 denote free-space permittivity and permeability, respectively. ϵ_r and μ_r denote relative permittivity and permeability of the material, respectively.

In the absence of free charge or current, inserting (2.5)-(2.7) into (2.1)-(2.4) gives:

$$\nabla \times E = -j\omega\mu H \tag{2.8}$$
$$\nabla \times H = j\omega\epsilon E \tag{2.9}$$
$$\nabla \cdot (\mu H) = 0 \tag{2.10}$$
$$\nabla \cdot (\epsilon E) = 0 \tag{2.11}$$

Taking the curl of (2.8) and inserting (2.9) into it gives:

$$\nabla \times (\nabla \times E) = \omega^2\mu\epsilon E \tag{2.12}$$

Rearranging this equation results in

$$\nabla(\nabla \cdot E) - \nabla^2 E = k^2 E \tag{2.13}$$

where $k^2 = \omega^2\mu\epsilon$ is the squared wavenumber. The wavenumber can be a real constant for non lossy media or a complex number for lossy media. For a nonmagnetic material (i.e., $\mu_r = 1$) with a complex permittivty ϵ, the squared wavenumber takes the form of

$$k^2 = \omega^2\mu_0\epsilon_0\epsilon_r - j\omega\mu_0\sigma \tag{2.14}$$

In regions where $\rho = 0$, $\nabla \cdot E = 0$, yielding Helmholtz equation

$$\nabla^2 E + k^2 E = 0 \tag{2.15}$$

Solutions to this equation in inhomogeneous media are needed in order to solve the forward problem in microwave tomography. Analytic solutions are typically known for simple geometries such as spheres and infinite cylinders. For more realistic cases, numerical methods have been developed. Some of these numerical solvers will be discussed in Section 2.3.

2.2.1 Scattering problem formulation

The scattering problem refers to calculating the scattered field in the region outside the scattering obstacle, i.e., $\mathbb{R}^d \setminus D$, where $D = D \bigcup \partial D$ and $d = 2, 3$, as shown in Figure 2.1. The modeling involves the Helmholtz equation, a boundary condition on the boundary ∂D, and Sommerfeld's radiation condition. To clarify, general numerical schemes do not specify boundary conditions. Consequently, reflections from the boundaries of the numerical grid occur. One option for modeling open space is to sufficiently enlarge the computational domain so that reflections from the edges of the numerical grid never interfere with the field pattern in the region of interest. An alternative is to employ Sommerfeld's radiation condition or absorbing boundary conditions. For a lossy media, Sommerfeld's radiation condition is satisfied since in this case the fields are sufficiently well attenuated so as not to be reflected at the boundaries of the numerical grid.

The Helmholtz equation can be separated into incident and scattered fields:

$$E_{tot} = E_{inc} + E_{scat} \tag{2.16}$$

The total electric field E_{tot} satisfies (2.15) in $\mathbb{R}^d \setminus D$ as well as the boundary conditions on ∂D. With a given incident field E_{inc} and dielectric properties of the background, the problem is to solve for the unknown scattered field E_{scat}.

2.3 Numerical methods

Different numerical methods have been employed to solve the electromagnetic equations involved in microwave scattering problems. The most popular schemes are the finite-difference (FD), finite-difference time-domain (FDTD), finite element (FE) methods, and method of moments (MoM). Among these numerical methods, the FDTD and FEM methods have been employed as the forward solver for the microwave imaging systems at Chalmers and Dartmouth. A brief overview of these methods is given in Sections 2.3.1 and 2.3.2.

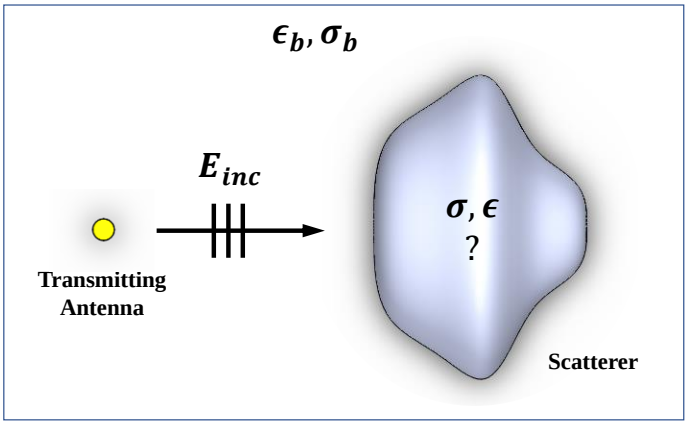

Figure 2.1: Investigation domain.

2.3.1 Finite-difference time-domain method

The FDTD method is one of the numerical solvers most commonly applied to microwave problems. Its popularity is due to it being efficient and straightforward to implement. With the FDTD method, the problem is solved on a structured Cartesian grid, and the equations are formulated in the time domain [83]. The entire solution domain is discretized, and the spacing discretization must be sufficiently small to resolve the object and provide enough resolution over a wavelength. This is necessary both for handling the small electromagnetic wavelengths and the small tumors in the breast. This format yields a very dense computational domain. The computation time scales up rapidly for larger problems. Moreover, modeling some components such as antennas is difficult in FDTD because of their complex geometry requiring even denser meshes than usual, which subsequently adds to the computational complexity.

A related drawback of this method in imaging is its inflexibility in handling geometries of arbitrary shape. Moreover, the boundary conditions are not explicitly considered in the original FDTD scheme. An open space for the electric field calculations is usually needed for imaging purposes, which entails enlarging the computational domain, typically increasing the computational complexity [84].

The FDTD scheme developed for the Chalmers microwave imaging system has been implemented and tested [84], and a complete description of the implementation of this method is given in [84]. Other microwave imaging research groups have also employed the FDTD method [85–91].

2.3.2 Finite element method

The FE method has been used widely as a numerical solver for the forward problem. In this method, the imaging domain is subdivided into small domains of simple

shapes such as tetrahedra (3D) or triangles (2D) [92]. The resulting sub-domains comprise a complete mesh in this scheme. The unstructured sub-elements have made the FE method a powerful tool in dealing with complex geometries, especially those with an arbitrary form. For example, in a situation where an object with a complex shape resides in a relatively uniform medium, the shape and the area immediately surrounding it can be finely discretized, while the more homogeneous zones can be more coarsely sampled without loss of accuracy. The electric field within the imaging domain is expressed with the help of a linear polynomial on each of these meshes. For an accurate approximation to the electric field distributions, a minimal size of elements is necessary, and the finer meshes result in a massive system of equations with a huge number of unknowns. Consequently, the computational complexity increases in this case, and producing an image takes many hours. However, these costs are largely mitigated by the fact that the resulting matrices are banded for which there are numerous efficient computation methods. Another drawback is that the method also uses large computer resources. The FE method usually requires more CPU time and memory compared to FDTD for the 3D setting but are comparable in 2D problems for similar resolution.

The Dartmouth imaging research group has used the FE scheme for calculating the electric field of the clinical imaging system. They implemented the dual mesh approach [93] to image tissue properties. First, a uniform, dense mesh is used to calculate the electric field distributions over the entire domain, and then a less dense mesh is used to represent the dielectric property distributions in the imaging domain. In this way, they have successfully obtained images in near real time. The FE method has also been used by other microwave imaging research groups [94–96].

2.3.3 Other numerical methods

There are other numerical solvers in addition to the finite difference and finite element methods; these are usually some format of integral equations. The integral equations are typically converted into a linear system of equations, which are solved to obtain the electric field in the domain. The MoM and the DDA belong to this category.

2.4 Discrete dipole approximation

This section provides an overview of the discrete dipole approximation (DDA) and describes the underlying principles and possible applications and implementations.

2.4.1 Introduction to the DDA

The idea of the discrete dipole approximation was first introduced in 1964 to study the optical properties of monomer units, such as molecular aggregates, molecular crystals,

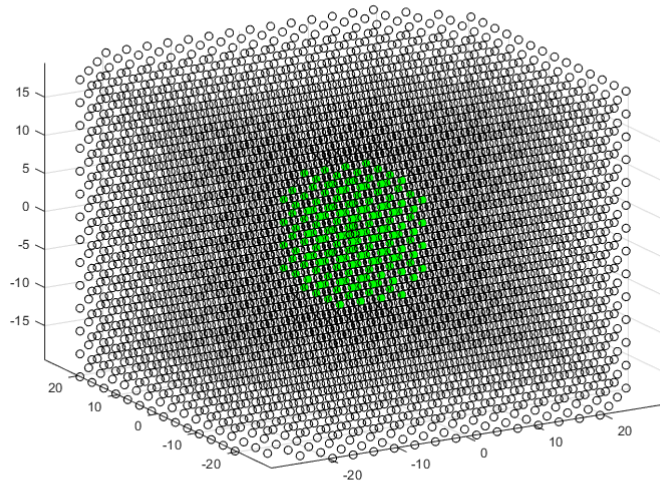

Figure 2.2: The discretized forward model zone. Each circle represents a centre point of a dipole.

or polymers [97]. In 1973, this method was proposed by Purcell and Pennypacker [98] to calculate absorption and scattering for dielectric grains of arbitrary shapes using a set of point dipoles, but they did not use the current terms, the discrete dipole approximation or coupled dipole approximation. Later, Draine and his colleagues also explored this method [99–102]. They implemented the DDA and made it publicly available as a computer code named DDSCAT [101,103]. The more theoretical aspects of the convergence and accuracy of the DDA and comparisons of available open source codes for the DDA were studied in further detail by Yurkin and his colleagues [104–106], who also developed another open source code, ADDA [107], with additional improvements in computational efficiency. One good comprehensive review of the development of the DDA is given in [108]. To the best of our knowledge, a more recent comprehensive review paper on the DDA does not exist.

The DDA, sometimes referred to as the coupled dipole method or approximation, is used to calculate the light scattering properties of an object with an arbitrary geometry. The principle behind the DDA is the idea of replacing the object with an array of dipoles (Figure 2.2).

The DDA can be formulated and developed in different ways [109]. Although other derivations deviate from the original implementation by Purcell and Pennypacker, and have typically not been referred to as DDA, their equivalence has been proven [110, 111], and Yurkin [109] has explained and compared these derivations briefly.

2.4.2 DDA and the 2D forward problem

The forward problem in microwave tomography requires solving the scattering problem in a domain comprising a coupling medium, a scatterer, and set of antennas

enclosing a scatterer. The electric field is formulated and solved as a sum of the incident and scattered electric fields according to (2.16). In this thesis, the 2D DDA method is used to calculate the scattered electric fields, instead of the more conventional FDTD or FE schemes.

In the DDA, the forward model zone is replaced with arrays of dipoles equally spaced in N small cells such that

$$D = \lim_{N\to\infty} \bigcup_{i=1}^{N} D_i \tag{2.17}$$

where D and D_i represent the forward model zone and cells, respectively. The two-dimensional incident electric field from a transmitting antenna is caused by a vertical electrical line source (ELS) and is described as [112]

$$E_{inc}(r_i) = \frac{I_0 \omega \mu_0}{4} H_0^{(2)}(k_b R_i) \tag{2.18}$$

where $E_{inc}(r_i)$ denotes the incident electric field at any dipole location r_i. I_0, ω, and μ_0 are the current amplitude, operating angular frequency, and free-space permeability, respectively. $H_0^{(2)}$ is the zero-order Hankel function of the second kind, k_b is the background wavenumber, and R_i are the dipole distances from the transmitting antenna. Moreover, the scattered electric field at a particular location can be formulated as the joint responses from all other dipoles such that:

$$E_{scat}(r_i) = \sum_{\substack{j=1 \\ j\neq i}}^{N} G_{ij} P_j \tag{2.19}$$

The operator G contains the information about all dipole interactions (i.e., G_{ij} are the elements of the interaction matrix for all i and j), and the term P_j is the polarization at each dipole location. Its value represents the material properties, which are assumed to be constant inside each of these cells. Using (2.16), (2.17), and (2.19) produces the total electric field at any dipole location r_i [101]:

$$E_{tot}(r_i) = E_{inc}(r_i) + \sum_{\substack{j=1 \\ j\neq i}}^{N} G_{ij} P_j \tag{2.20}$$

The G_{ij} term from the Green's function for the 2D Helmholtz equation [43, 113] describes the interactions between two dipoles located at r_i and r_j and is written as

$$G_{ij} = \frac{-j}{4} H_0^{(2)}(k_b r_{ij}) \tag{2.21}$$

where r_{ij} is the distance between nodes i and j. Moreover, at the macroscopic level, the total electric field is proportional to the polarization P via

$$P = \epsilon_0 \chi E_{tot} \tag{2.22}$$

where χ is electric susceptibility. The vector P and the total electric field in the microscopic analysis are also related to each other via

$$P = N\epsilon_0 \alpha E_{loc} \tag{2.23}$$

where N is the number of molecules per unit volume and α is the polarizability term, see the next section. E_{loc} is the microscopic electric field sensed by each molecule and is also the field that polarizes them to exhibit dipole moment p. In this format, using (2.22) and (2.23), (2.20) converts in SI units to:

$$\epsilon_0 E_{inc}(r_i) = \frac{P_i}{\alpha_i} - \sum_{\substack{j=1 \\ j \neq i}}^{N} G_{ij}\, P_j \tag{2.24}$$

It is worth noting that there is an ambiguity in the definition of molecular polarizability following previous studies [114]. Depending on the author, ϵ_0 is sometimes included in the definition of α. Knowing this ambiguity, the term α can have a unit of m^3 or $C \cdot m^2/V$ depending on the definition. In (2.23) and (2.24), the scalar α has a unit of $C \cdot m^2/V$. CGS units are also used in many articles on the DDA method, and (2.24) converts to:

$$E_{inc}(r_i) = \frac{P_i}{\alpha_i} - \sum_{\substack{j=1 \\ j \neq i}}^{N} G_{ij}\, P_j \tag{2.25}$$

This equation is based on the definition, $P = N\alpha E_{loc}$, corresponding to (2.23). The system of equations (2.24) is solved for vector P, and then (2.20) is used to calculate the total electric field in the forward model zone.

The solution to the linear system of equations can be obtained via direct or inverse solvers. Such solvers are discussed further in Section 2.4.4.

2.4.3 Dipole polarizability: possibilities and challenges

The term α expresses the relationship between the susceptibility as a macroscopic parameter and the molecular polarizability as a microscopic parameter. The polarizability term α is commonly modeled via the Clausius-Mossotti relation (CM) and relates the relative permittivity ϵ_r of a dielectric to the polarizability α of the molecules constituting the dielectric property. For a spherical inclusion located in free space, the dipole polarizability is [100, 115]

$$\alpha_{CM} = 3v \frac{\epsilon_r - 1}{\epsilon_r + 2} \tag{2.26}$$

Here ϵ_r and v are the relative permittivity and the volume of the sphere. In [73], this equation is generalized to an arbitrary background as

$$\alpha_{CM,3D} = 3v\frac{\epsilon_t - \epsilon_b}{\epsilon_t + 2\epsilon_b} \tag{2.27}$$

where ϵ_b and ϵ_t are the complex permittivities of the background and target, respectively. The applicability of this formulation to the 3D case has been tested in [73]. The challenge associated with the CM relation is that it is only exact for static fields and for studies with finite frequencies. For microwave tomography, for instance, a correction to the CM relation is necessary. In such a case, the CM relation is a good initial value but not very accurate [116]. The accuracy of the forward solution from the DDA impacts the electric field distribution and especially perturbations around the scatterers; consequently, the recovered images of electrical properties (i.e., dielectric permitivity and conductivity). To ensure that the optical theorem is satisfied, Draine improved the CM relation by including the "radiative reaction (RR)" term, which converts the general CM relation to

$$\alpha_{RR} = \frac{\alpha_{CM}}{1 - (\frac{2}{3})jk^3\alpha_{CM}} \tag{2.28}$$

where k is the wavenumber and j is the imaginary unit [100]. This formulation is known as the CM plus radiative reaction [100].

In addition to the CM relation or one of its modified versions, the Maxwell-Garnett mixing formula [117] can also be used to model the polarizability for a microwave tomography system. The main reason is that the breast imaging system contains an imaging tank that is filled with a coupling medium, a mixture of glycerin and water, as shown in Figure 2.3. The scatterers also have different complex dielectric coefficients, and such cases can be treated according to the mixing rules for multiple complex dielectrics. Sihvola [118] proposed multiple approaches for modeling such scenarios, including the Maxwell-Garnett relation. The most common version of the Maxwell-Garnett mixing rules suggests that

$$\alpha_{MG,3D} = f\frac{\epsilon_{t,i} - \epsilon_{b,i}}{\epsilon_{t,i} + 2\epsilon_{b,i}} \tag{2.29}$$

where f is the volume fraction of the scatterer in the mixture. This formula is called the Rayleigh mixing formula [118]. The formula is typically satisfactory if the scattering phenomena can be ignored. For breast imaging, the situation is more complicated given the strong dielectric contrast between healthy tissue and tumours and also having heterogeneously dense breasts. In this case, a more generalized version of (2.29) is proposed to deal with the heterogeneities [118].

$$\frac{\epsilon_{mix} - \epsilon_b}{\epsilon_{mix} + 2\epsilon_b} = \sum_{k=1}^{K} c_k \frac{\epsilon_k - \epsilon_b}{\epsilon_k + 2\epsilon_b} \tag{2.30}$$

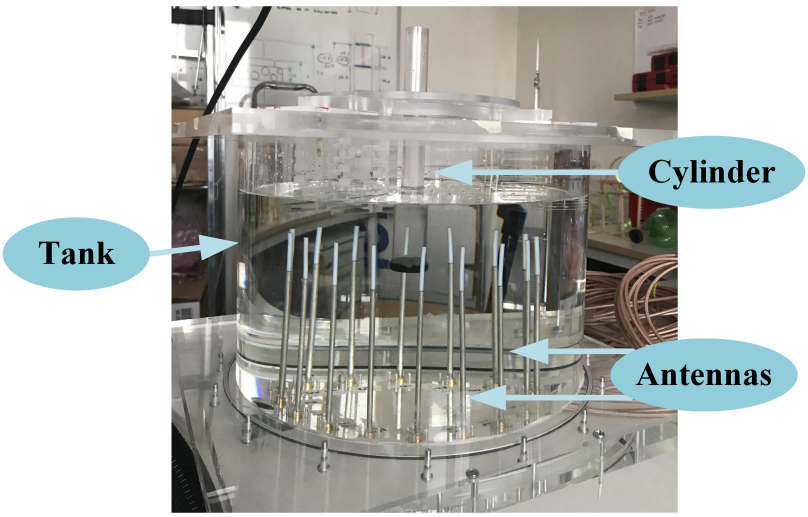

Figure 2.3: The measurement set-up including the tank, antennas, and the simplistic phantom. The image is from Paper B.

In (2.30), ϵ_{mix} denotes the composite medium consisting of K media with permittivities, ϵ_k. The coefficients, c_k, defined as $\frac{m}{M_r V}$ where V, m, M_r are volume, mass, and the molecular weight of the inclusion, respectively.

The other challenge in modeling the polarizability for our tomographic algorithm lies in deducing the 2D model from the existing 3D models. To achieve a fast imaging process, a 2D reconstruction algorithm is superior to 3D imaging, while the polarizability and the corresponding formulas from a 3D algorithm are expected to be valid with respect to their physical theories. One study on reducing the 3D models to 2D suggests a general formula for the dimensionless α in d dimensions as [119]

$$\alpha = d\frac{\epsilon_t - \epsilon_b}{\epsilon_t + (d-1)\epsilon_b} \tag{2.31}$$

Combining this study with the CM imaging relation, we have that the polarizability of a circle can be calculated via

$$\alpha_{CM,2D} = 2\frac{\epsilon_{t,i} - \epsilon_{b,i}}{\epsilon_{t,i} + \epsilon_{b,i}} \tag{2.32}$$

The main deviation from the other formulas is that this relation considers normalized polarizability [119] (i.e., the scaling coefficient in the CM relation is discarded). Based on (2.30) and (2.31), the two dimensional α in the form of the Maxwell-Garnett formula is expressed as:

$$\alpha_{2D} := \frac{\epsilon_{mix} - \epsilon_b}{\epsilon_{mix} + \epsilon_b} = \sum_{k=1}^{K} c_k \frac{\epsilon_k - \epsilon_b}{\epsilon_k + \epsilon_b} \tag{2.33}$$

The concentration coefficients c_k are modified based on the area of the inclusion for the 2D case.

In addition to the mentioned approaches, based on the study performed by Steffan and Richter [120], it appears realistic to propose computation of the polarizability term via

$$\alpha_{2D,imaging} = \frac{\pi}{6}\left(\frac{\epsilon_{r,t} - \epsilon_{r,b}}{\epsilon_{r,t} + \epsilon_{r,b}} + j\frac{\sigma_t - \sigma_b}{\sigma_t + \sigma_b}\right) \tag{2.34}$$

where $\epsilon_{r,t}$, $\epsilon_{r,b}$, σ_t, and σ_b are the relative permittivities and conductivities of the target and background, respectively. For all of these formulations, it is notable that for the purpose of imaging where the actual properties are unknown, the properties of the target are replaced with those computed iteratively on the parameter mesh.

2.4.4 Overview of direct and iterative solvers

In general, a system of equations is represented in the form of

$$Ax = b \tag{2.35}$$

where A is the given coefficient matrix, x is the unknown vector, and b is also known. A linear system of equations can be solved via direct or iterative solvers. The direct solver refers to methods such that the solutions are obtained in one step. One way to obtain x is to invert the matrix A and multiply the right hand side, b, by it. This approach is problematic in certain conditions including:

- matrix A is not invertible;
- matrix A is not square;
- matrix A is singular or close to singular.

Even if A is invertible, calculation of its inversion matrix, A^{-1}, is usually very expensive, especially for large numbers of unknowns. In such cases, other direct solvers are used. Common methods to directly calculate the solution include Gaussian elimination, LU decomposition, Cholesky, and QR decomposition, see [121] for details. Direct solvers are not practical if the matrix size is large. For example, if the matrix is of size n, Gaussian elimination has complexity of $\mathrm{O}(n^3)$. For systems with many unknowns, iterative solutions are often favored instead. Iterative solutions start by assuming an approximate solution for the unknown x and require multiple intermediate steps to determine the exact solution for the system. Due to their computational efficiency, Krylov subspace-based methods, such as the conjugate gradient (CG) algorithm and its variants, are popular for solving linear systems of equations.

If the matrix A in (2.35) is positive definite, the system of equations can be solved with the CG method. For the cases where these properties are not satisfied, other

CG-type methods are typically used. The body of iterative algorithms consists of three main parts: initialization, inside loop, and iteration check. The inside loop reveals that the matrix-vector multiplication is the most computationally expensive operation in an iterative method. Therefore, substantial attention needs to be devoted to it in order to limit the computation time.

2.4.5 The 2D DDA as a system of equations

The following system of equations is used to calculate the polarization P [99]:

$$E_{inc}(r_i) = \frac{P_i}{\alpha_i} - \sum_{\substack{j=1 \\ j \neq i}}^{N} G_{ij}\, P_j \tag{2.36}$$

The system of equations (2.36) can be reduced to the following master relationship [73]:

$$\alpha_i E_{inc}(r_i) = P_i - \alpha_i \sum_{j \neq i} G_{ij} P_j \tag{2.37}$$

This can be rearranged in matrix format to produce:

$$\begin{bmatrix} 1 & -\alpha_1 G_{12} & -\alpha_1 G_{13} & \dots & -\alpha_1 G_{1N} \\ -\alpha_2 G_{21} & 1 & -\alpha_2 G_{23} & \dots & -\alpha_2 G_{2N} \\ -\alpha_3 G_{31} & -\alpha_3 G_{32} & 1 & \dots & -\alpha_3 G_{3N} \\ \vdots & \vdots & \vdots & \ddots & \vdots \\ -\alpha_N G_{N1} & -\alpha_N G_{N2} & -\alpha_N G_{N3} & \dots & 1 \end{bmatrix} \begin{bmatrix} P_1 \\ P_2 \\ P_3 \\ \vdots \\ P_N \end{bmatrix} = \begin{bmatrix} \alpha_1 E_{inc}(r_1) \\ \alpha_2 E_{inc}(r_2) \\ \alpha_3 E_{inc}(r_3) \\ \vdots \\ \alpha_N E_{inc}(r_N) \end{bmatrix} \tag{2.38}$$

Here r_i is the spatial location of each dipole. This is a general square matrix that can be solved with any direct or iterative solver. In this form, the computation time is not substantially less than for other numerical solvers such as FDTD or FE schemes. However, iterative solvers are known to be more time efficient compared to direct solvers. The set of equations in (2.36) can also be rearranged in matrix format as

$$\underbrace{\begin{bmatrix} \frac{1}{\alpha_1} & -G_{12} & -G_{13} & \dots & -G_{1N} \\ -G_{21} & \frac{1}{\alpha_2} & -G_{23} & \dots & -G_{2N} \\ -G_{31} & -G_{32} & \frac{1}{\alpha_3} & \dots & -G_{3N} \\ \vdots & \vdots & \vdots & \ddots & \vdots \\ -G_{N1} & -G_{N2} & -G_{N3} & \dots & \frac{1}{\alpha_N} \end{bmatrix}}_{A_{ij}} \begin{bmatrix} P_1 \\ P_2 \\ P_3 \\ \vdots \\ P_N \end{bmatrix} = \begin{bmatrix} E_{inc}(r_1) \\ E_{inc}(r_2) \\ E_{inc}(r_3) \\ \vdots \\ E_{inc}(r_N) \end{bmatrix} \tag{2.39}$$

where $A = (diag(\frac{1}{\alpha}) - G)$. As mentioned, the matrix-vector multiplication is the most computationally expensive operation in inside loop calculations for iterative solvers. This multiplication is typically performed repeatedly until a converged solution is obtained. To increase the computational efficiency, the matrix A_{ij} is broken into two parts—the diagonal and off-diagonal terms, respectively—such that:

$$A_{ij}P_j = \begin{bmatrix} \frac{1}{\alpha_1} & 0 & 0 & \dots & 0 \\ 0 & \frac{1}{\alpha_2} & 0 & \dots & 0 \\ 0 & 0 & \frac{1}{\alpha_3} & \dots & 0 \\ \vdots & \vdots & \vdots & \ddots & \vdots \\ 0 & 0 & 0 & \dots & \frac{1}{\alpha_N} \end{bmatrix} \begin{bmatrix} P_1 \\ P_2 \\ P_3 \\ \vdots \\ P_N \end{bmatrix} + \begin{bmatrix} 0 & -G_{12} & -G_{13} & \dots & -G_{1N} \\ -G_{21} & 0 & -G_{23} & \dots & -G_{2N} \\ -G_{31} & -G_{32} & 0 & \dots & -G_{3N} \\ \vdots & \vdots & \vdots & \ddots & \vdots \\ -G_{N1} & -G_{N2} & -G_{N3} & \dots & 0 \end{bmatrix} \begin{bmatrix} P_1 \\ P_2 \\ P_3 \\ \vdots \\ P_N \end{bmatrix} \quad (2.40)$$

The first matrix-vector operation on the right-hand side can be performed pointwise as a vector-vector multiplication. The second matrix-vector operation on the right-hand side is the dominant operation in computation time for the iterative CG-type algorithms. The key to handling this matrix-vector operation efficiently lies in the properties of the complex and symmetric matrix G; the next section provides more detail on formulations and implementations.

2.4.6 Krylov subspace methods for the DDA

Krylov subspace algorithms are used to solve large systems of equations iteratively. They have been used for solving linear systems of equations in various applications, including in electromagnetics [122–124]. These methods are most effective for sparse matrices (meaning most elements are zero), which often have narrow bandwidth. The bandwidth of a matrix is determined by the number of non-zero diagonals above and below the main diagonal, where the rest of the elements are zero. Thus a narrow bandwidth matrix only has a few non-zero diagonals. In particular, discretization of partial differential equations (PDEs) with the FE method or FD methods leads to these conditions. These methods are usually referred to as conjugate gradient-based algorithms, where the most commonly used method is the well-known conjugate gradient (CG) algorithm. The iterative CG algorithm is employed for real symmetric positive definite systems, for which $A^T yA > 0$ for an arbitrary vector y. Here A^T indicates the transpose of A. The idea behind iterative CG-type algorithms is to form a (orthogonal) basis for the Krylov subspace.

When solving the forward problem with the DDA method, it is necessary to solve a system of linear equations (2.39), expressed in compact form as

$$Ax = b,\ A = (a_{ij}) \in \mathbb{C}^{n\times n},\ x,\ b \in \mathbb{C}^n \quad (2.41)$$

where A is complex symmetric (non-Hermitian), i.e., $A = A^T \neq A^H$. For such a system of equations, there are different iterative solvers such as the quasi-minimal

residual (QMR) [125], the BiCG-type methods such as the symmetric complex BiCG (SCBiCG) method [122], the conjugate orthogonal conjugate gradient (COCG) [123], and the conjugate orthogonal conjugate residual (COCR) [124]. The COCG and COCR algorithms are preferred over other types in terms of computational efficiency, since they require only one matrix-vector multiplication per iteration. The principles of these algorithms are similar to those of the regular CG algorithm. The main difference is how the basis of the d-dimensional Krylov subspace $K^d(A; r_0)$ is constructed. For a linear system, $r_0 = b - Ax_0$ is the initial residual for the initial guess, x_0. Details in the COCG and COCR methods are reproduced in Algorithms 1 and 2 from [123, 124].

$x \leftarrow x_0$;
$r \leftarrow b - Ax_0$;
$\rho \leftarrow (r, r^t)$;
$p \leftarrow r^t$;
while $\|r\| > TOL$ **do**
  $q \leftarrow Ap$;
  $\mu \leftarrow (p, q^t)$;
  if $\mu = 0$ **then**
    Quit (failure)
  end
  $\alpha \leftarrow \frac{\rho}{\mu}$;
  $x \leftarrow x + \alpha p$;
  $r \leftarrow r - \alpha q$;
  if *x is accurate enough* **then**
    Quit (Convergence);
  else
    $\beta \leftarrow \rho$;
    $\rho \leftarrow (r, r^t)$;
    $\beta \leftarrow \frac{\rho}{\beta}$;
    $p = r^t + \beta p$;
  end
  return x
end

Algorithm 1: The COCG algorithm

$x \leftarrow x_0$;
$r \leftarrow b - Ax_0$;
$\rho \leftarrow (r, r^t)$;
$p \leftarrow r^t$;
$q \leftarrow Ap$;
while $\|r\| > TOL$ **do**
  $\mu \leftarrow (q, q^t)$;
  if $\mu = 0$ **then**
    Quit (failure)
  end
  $\alpha \leftarrow \frac{\rho}{\mu}$;
  $x \leftarrow x + \alpha p$;
  $r \leftarrow r - \alpha q$;
  $r^t \leftarrow r^t - \alpha q^t$;
  $t \leftarrow Ar^t$;
  if *x is accurate enough* **then**
    Quit (Convergence);
  else
    $\beta \leftarrow \rho$;
    $\rho \leftarrow (r, r^t)$;
    $\beta \leftarrow \frac{\rho}{\beta}$;
    $p = r^t + \beta p$;
    $q = t + \beta q$;
  end
  return x
end

Algorithm 2: The COCR algorithm

In Algorithms 1 and 2, the most prominent operations regarding computational aspects are matrix-vector multiplications $A \times p$ and $A \times r^t$, respectively. These operations can be performed in the form of (2.40). Generally, the operator $G \times P$

(matrix-vector multiplication) in (2.36) has a computational cost of order $O(N^2)$. The matrix-vector multiplications can be done efficiently under specific circumstances. One approach is to employ the FFT. Details on this topic are given in following section.

2.4.7 Krylov subspace methods and preconditioning

Although the Krylov subspace methods are usually found to be very efficient iterative solvers with low computational cost, they do not always converge quickly, depending on the coefficient matrix, A in (2.41) [126]. If the coefficient matrix is not well-conditioned and definite, the convergence rate of these methods can be extremely slow. In such cases, these methods need to be used with a preconditioner. The principle of the preconditioning is to reformulate the linear system of equations such that its solution is unchanged, but the condition number of the coefficient matrix is lowered. The mathematical formulation of the preconditioned linear system is given by

$$M^{-1}Ax = M^{-1}b \tag{2.42}$$

where M is non-singular preconditioner matrix. In this example, preconditioning is applied from the left, but preconditioning from the right is also common. Benzi [127] summarized the preconditioning approach and stated that a good preconditioner should satisfy the following criteria [127]:

1. the preconditioned system should be easy to solve;

2. the preconditioner should be cheap to construct and apply.

Criterion 1 assures an acceptable convergence rate, and criterion 2 assures it comes at a moderate computational cost for the iterative solver. The most convenient choice for M^{-1} is the inverse of the coefficient matrix A. However, the computational cost for computing the inverse of A is very high, which makes the preconditioner A^{-1} impractical.

There is no rule of thumb for choosing an appropriate and efficient preconditioner. However, there are many alternatives for selecting the preconditioning matrix. The linear system of equations in (2.41) is complex symmetric and indefinite. For such a system, an option for the preconditioning matrix is the symmetric successive over-relaxation (SSOR) [126, 128]. The SSOR only adds a moderate computational cost to the original problem. Another well-known preconditioner is the incomplete LU factorization, ILU, which attempts to approximate the LU factorization of a matrix in a sparse format [126]. The ILU is usually applicable to symmetric and positive definite matrices. Additionally, the format of coefficient matrices in (2.40) is such that only the diagonal terms ($\frac{1}{\alpha}$) contribute to the ill-conditioned part of the system, and the matrix G does not change. In this way, employing the ILU preconditioning

on the complete coefficient matrix A adds to the computational cost of the iterative solver and diminishes the advantage of the DDA as a fast forward solver. Since the diagonal terms ($\frac{1}{\alpha}$) have large magnitudes and these values are dominant compared to the elements of the G matrix, the Jacobi preconditioner [126] can be employed without adding to the computational cost of the solver. In the Jacobi preconditioner, the diagonal of the matrix is chosen as the preconditioner, i.e., $M = diag(\frac{1}{\alpha})$. The preconditioned COCG algorithm is given in Algorithm 3.

$x \leftarrow x_0$;
$r \leftarrow b - Ax_0$;
$\rho \leftarrow (r, r^t)$;
$p \leftarrow M^{-1}r$;
while $\|r\| > TOL$ **do**
  $q \leftarrow Ap$;
  $\mu \leftarrow (p, q^t)$;
  if $\mu = 0$ **then**
    Quit (failure)
  end
  $\alpha \leftarrow \frac{\rho}{\mu}$;
  $x \leftarrow x + \alpha p$;
  $r \leftarrow r - \alpha q$;
  $M^{-1}r \leftarrow r^t$;
  if *x is accurate enough* **then**
    Quit (Convergence);
  else
    $\beta \leftarrow \rho$;
    $\rho \leftarrow (r, r^t)$;
    $\beta \leftarrow \frac{\rho}{\beta}$;
    $p = r^t + \beta p$;
  end
  return x
end

Algorithm 3: The Jacobi preconditioned COCG algorithm

2.4.8 Matrix-vector multiplication using the FFT

The matrix-vector multiplication can be fast for some structured matrices such as Toeplitz and circulant matrices [129]. These matrices can be multiplied by vectors with a $O(n \log n)$ computational cost, instead of $O(n^2)$. A Toeplitz matrix T has a regular repetition of the individual coefficients, but it is not necessarily symmetric:

$$T = \begin{pmatrix} a & b & c & d & e \\ f & a & b & c & d \\ g & f & a & b & c \\ h & g & f & a & b \\ i & h & g & f & a \end{pmatrix} \tag{2.43}$$

A circulant matrix C is a special case of the Toeplitz matrix of the form

$$C = \begin{pmatrix} a & b & c & d & e \\ e & a & b & c & d \\ d & e & a & b & c \\ c & d & e & a & b \\ b & c & d & e & a \end{pmatrix} \tag{2.44}$$

The unique property of a circulant matrix is that it can be represented by the values in a single row. With respect to computational efficiency, there is a substantial savings in terms of memory requirements. Matrix G in (2.40) is a symmetric block Toeplitz matrix, which means that each of the N portions of size $n \times n$ (where $n = \sqrt{N}$)of the matrix G are themselves Toeplitz matrices (Figure 2.4). The Toeplitz submatrices are symmetric and can be converted to circulant matrices. To accomplish this, columns and rows for the Toeplitz submatrices are padded appropriately to produce circulant matrices in the form of

$$C_1 = \begin{pmatrix} g_1 & g_2 & \cdots & g_{n-1} & g_n & g_{n-1} & \cdots & g_2 \\ g_2 & g_1 & g_2 & \ddots & g_{n-1} & g_n & \cdots & g_3 \\ \vdots & g_2 & g_1 & \ddots & \vdots & g_{n-1} & \ddots & \vdots \\ g_{n-1} & \ddots & g_2 & g_1 & g_2 & \ddots & g_{n-1} & g_n \\ g_n & g_{n-1} & \ddots & g_2 & g_1 & g_2 & \ddots & g_{n-1} \\ g_{n-1} & g_n & g_{n-1} & \ddots & g_2 & g_1 & g_2 & \ddots \\ \vdots & g_{n-1} & g_n & g_{n-1} & \ddots & g_2 & g_1 & g_2 \\ g_2 & \ddots & g_{n-1} & g_n & g_{n-1} & \ddots & g_2 & g_1 \end{pmatrix}$$

The remaining circulant matrices C_i, where $2 \leq i \leq N$ are calculated in a similar way. Consequently, the system of equations with coefficient matrix G is converted to a large circulant linear system.

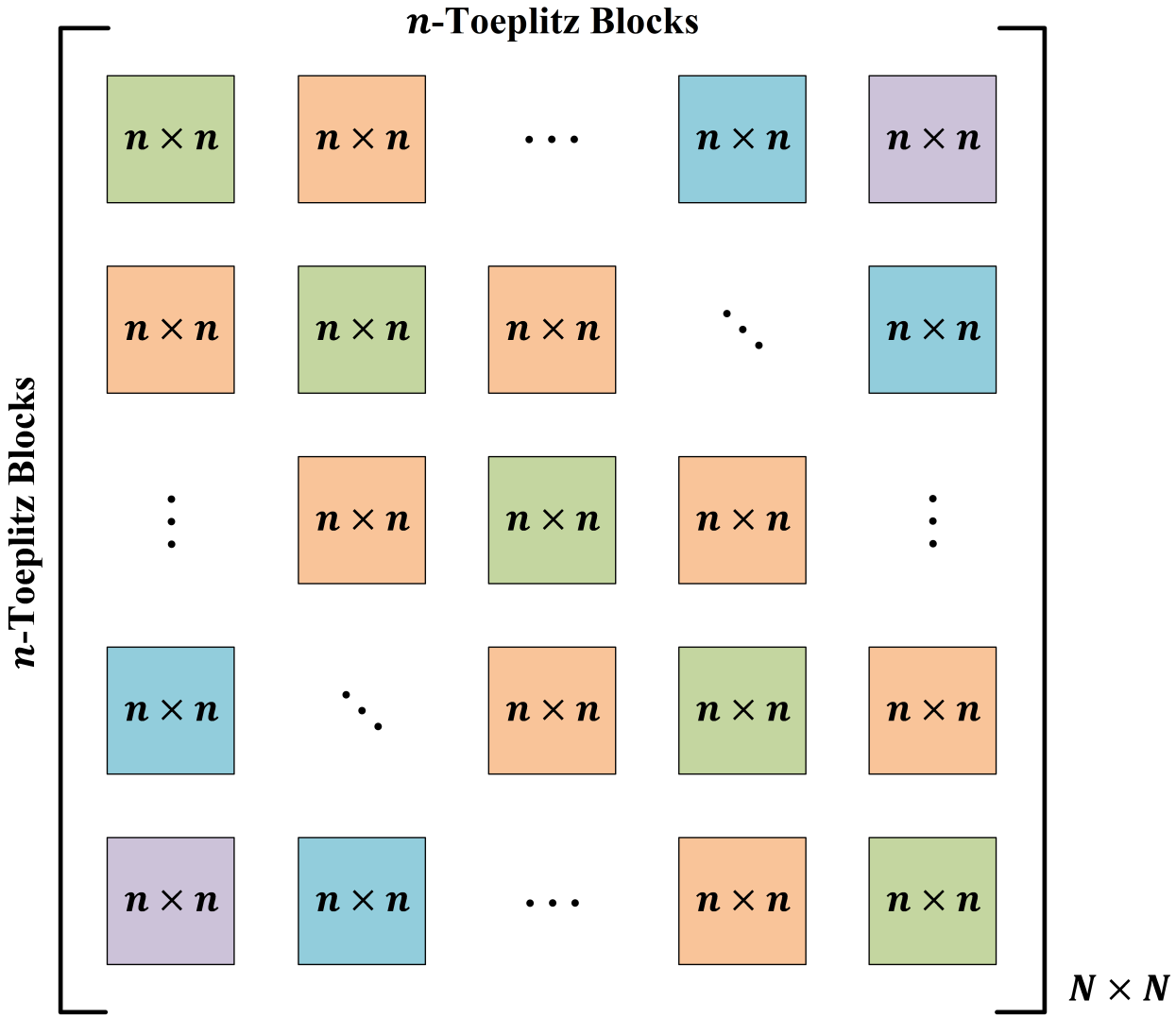

Figure 2.4: Block Toeplitz matrix G. The image is from Paper B.

Multiplication of a vector solution $x = (x_0, x_1, \ldots, x_n)$ by circulant matrices C, is equivalent to an operation called a circular convolution. According to the convolution theorem, this convolution is performed using the n-point Fourier transformation, which means that the Fourier transform of a convolution is the pointwise product of Fourier transforms. This indicates that we can multiply $C \times x$ for any circulant matrix C in $O(n \log n)$ operations. This implies that to multiply $C \times x$, we just need to:

- calculate the fast Fourier transform (FFT) of the first column of the matrix and the vector;
- multiply the two vectors pointwise; and
- take the inverse FFT to recover the result.

In this manner, the matrix-vector multiplication with $\mathrm{O}(N^2)$ computational complexity is reduced to an $\mathrm{O}(N \log N)$ operation. With this formulation, the computation time is reduced dramatically, and it significantly improves overall efficiency in terms of computation time.

2.4.9 Electric field distributions and computation times

Samples of the results from the proposed 2D DDA are presented here. The 2D DDA solver is employed to calculate the electric field distributions in the forward model zone. To accomplish this, an array of dipoles is utilized to model the physical geometry of our imaging system. Figure 2.5 presents a 2D geometry of a uniform grid with different numbers of dipoles. COMSOL Multiphysics, a finite-element-based solver is also used for the baseline results to benchmark the 2D DDA forward solutions.

In the forward model, an extended square modeling zone with side of 40 cm is considered. Two circular inclusions are assumed within the imaging domain. An inclusion (target #1) of diameter 6 cm is at $x = 4$ and $y = -2$, and another inclusion (target #2) of diameter 3 cm is located at $x = -3$ and $y = 4$. The transmitting antenna is located at $x = -7.62$ cm. The 2D DDA forward solutions are investigated with respect to multiple parameters:

- number of dipoles for representing the geometry;
- target size; and
- property contrast.

A comprehensive study of these parameters and their impacts is provided in Paper A. Here, some cases of electric field distributions are presented.

In these simulations, accuracy is tested for either 900 or 3600 dipoles. For two circular inclusions, two cases with different relative permittivities are investigated:

1. relative permittivities of targets #1 and #2 are set to 25 and 45, respectively;

2. relative permittivities of targets #1 and #2 are set to 45 and 25, respectively.

Figures 2.6 and 2.7 show the magnitude and phase distributions for the 900- and 3600-dipole cases along with the COMSOL solution. Our observations show that the 900-dipole case does not capture the perturbation around the objects, while the case with 3600 dipoles does. Additionally, when using adequate numbers of dipoles within the forward model zone, the 2D DDA and COMSOL results are comparable.

The computational aspects of the 2D DDA are studied in Paper B. Here, we present some samples for the computation times. The computation times for the direct and iterative solvers are summarized in Table 2.1. For comparison, computation times for implementations in both MATLAB, as an interpretive language, and C++, a classic compiler-based code, are investigated. The results indicate that it is useful to compare performances of forward solvers with both MATLAB and C++ code. While the interpretive codes struggle in terms of computation time with constructs such as loops, they contain highly optimized matrix operations that can often overcome such disadvantages. These investigations show that the computation time for the 2D DDA is significantly decreased in the iterative approach combined with FFT. The best performance is achieved in C++ using an open source C++ package for fast Fourier transform calculations, denoted FFTW packages [130].

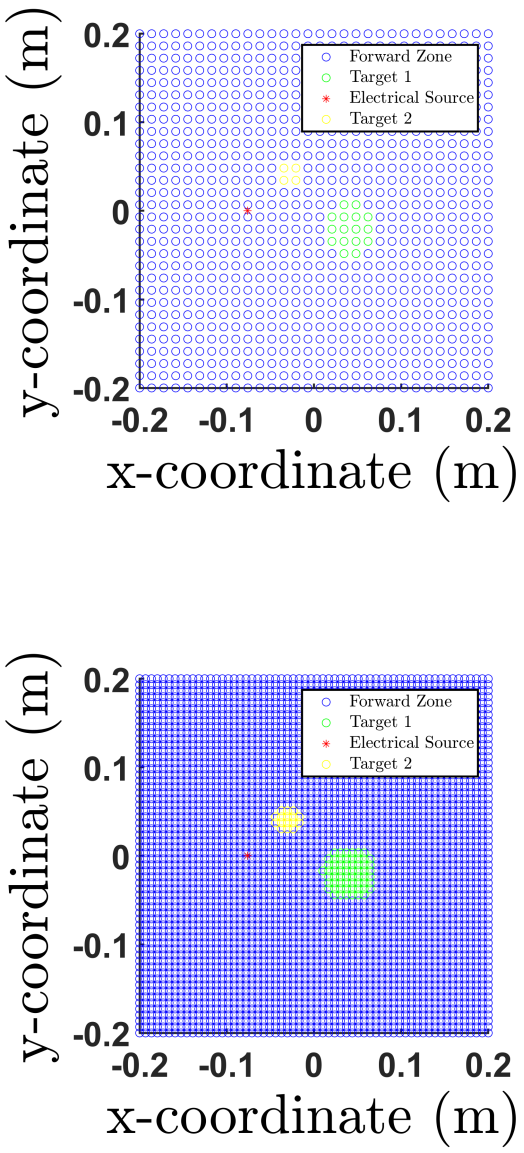

Figure 2.5: Diagrams of the 2D forward model zone utilizing (top) 900, and (bottom) 3600 dipoles, respectively.

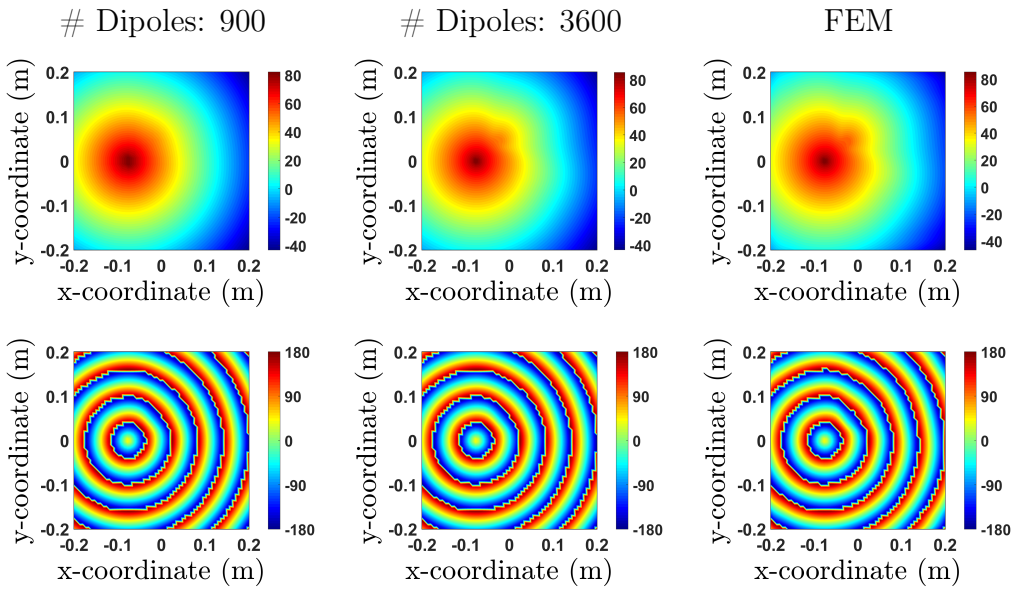

Figure 2.6: Plots of magnitude (top) and phase (bottom) distributions for f =1.0 GHz, $\sigma = 1$, $\epsilon_{r,b} = 22$, $\epsilon_{r,t1} = 25$, $\epsilon_{r,t2} = 45$, $d_1 = 3$ (cm), and $d_2 = 6$ (cm).

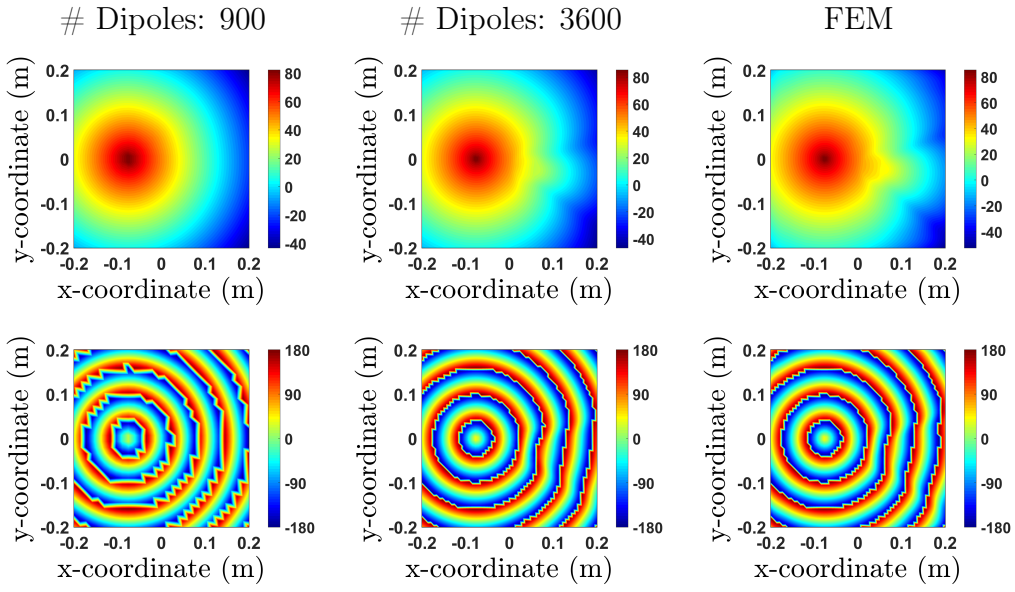

Figure 2.7: Plots of magnitude (top) and phase (bottom) distributions for f =1.0 GHz, $\sigma = 1$, $\epsilon_{r,b} = 22$, $\epsilon_{r,t1} = 45$, $\epsilon_{r,t2} = 25$, $d_1 = 3$ (cm), and $d_2 = 6$ (cm).

Table 2.1: Computation time (s)

Method	#dipoles	code language/Library		
		MATLAB	C++ (Armadillo)	C++ (FFTW)
Direct	900	0.0255	0.3780	n/a
	3600	0.9378	22.9960	n/a
	4225	1.5337	32.2780	n/a
COCG	900	0.01825	0.0317	n/a
	3600	1.1122	1.1027	n/a
	4225	1.4979	1.5455	n/a
COCR	900	0.0229	0.0034	n/a
	3600	1.3329	1.0865	n/a
	4225	1.6131	1.5531	n/a
COCG-FFT	900	0.1884	0.0726	0.0619
	3600	2.1786	1.3015	1.0635
	4225	2.0423	1.3615	0.8012
COCR-FFT	900	0.1898	0.0719	0.0619
	3600	2.1282	1.2035	1.0835
	4225	2.1163	1.3105	0.8142

Chapter 3

Inverse Problem

This chapter gives an overview of the inverse problem and the reconstruction algorithms for solving it. The challenges associated with the inverse problem and possible strategies for meeting these are also discussed.

3.1 Overview

The inverse problem recovers the information about the position, shape, and dielectric properties of an object from the electromagnetic fields on the boundary of the domain. The underlying idea in these types of optimization algorithms is to minimize the difference between the measured data and computed solutions. In each iteration, the dielectric properties within the domain are updated, and the process is repeated until a convergence criterion is satisfied.

The objective of microwave tomography is to create images of the dielectric properties, i.e., permittivity and conductivity. An image is reconstructed by solving an inverse problem of Maxwell's equations. In an inverse problem, material parameters or sources inside a region are calculated from observations of electromagnetic waves at a boundary completely or partially enclosing the region. Importantly, inverse problems can be either well-posed or ill-posed. A well-posed problem satisfies the following postulates [131]:

- existence: a solution to the problem exists;
- uniqueness: the solution is unique; and
- continuity: the solution is continuous with respect to initial conditions and boundary conditions.

These requirements were formulated based on a concept introduced by Jacques Hadamard [131]. The problem is well-posed if all three postulates are satisfied. If at least one of these conditions is not fulfilled, the problem is ill-posed.

The inverse scattering problems in microwave tomography are known to be ill-posed due to the existence of non-unique solutions; additionally, the solutions do not depend continuously on the data. Obtaining a unique solution requires vast amounts of measurement data, and this impacts the size of the tomographic system and the problem. Moreover, the solutions do not depend continuously on data due to the irregular dependency between the dielectric property distribution and the measurement data [132]. A common strategy for overcoming a lack of continuity is to regularize the reconstruction algorithm.

3.2 Microwave tomographic imaging

Microwave imaging of the breast is based on variations in dielectric properties in the tissue. Malignant tissue exhibits a high dielectric contrast in the presence of normal tissue. In general, small, low-contrast objects are known as weakly scattering objects. For these, efficient linear algorithms can often be used for image reconstruction. Large, high-contrast objects are known as strongly scattering objects, and the breast with a tumor is an example of a such situation. In this case, a more computationally demanding iterative reconstruction algorithm is needed, and this is the type of algorithm that is treated in this work.

3.2.1 Microwave tomographic algorithms

Multiple reconstruction algorithms are implemented to solve inverse scattering problems. Born and Rytov approximation methods are typically employed for weakly scattering objects and known as linear tomography [133]. These methods usually solve the reconstruction problem in one single iteration. Other reconstruction algorithms based on Newton and gradient minimization methods have been developed for strongly scattering cases that are known to be mathematically more challenging; these methods are known as non-linear tomography [133]. These methods usually involve an iterative optimization problem.

In the following, different iterative algorithms for high-contrast scenarios will be discussed. The Born iterative method (BIM) is a straightforward extension of a linear Born approximation-based method to a non-linear iterative algorithm. In the BIM, the scattered electric field, as expressed in (2.16), is approximated via Born series [134]. In the first-order Born approximation, the incident electric field is used as initial value for the total electric field. That is, the total electric field is approximated with the incident electric field, yielding a linear expression for the total field [133]. In this method, Green's function remains unchanged in the iterative process [135]. A further development to the BIM is the distorted Born iterative method (DBIM). In this version, Green's function is updated, and, as in BIM, the the total electric field is approximated with the incident electric field. In these iterative approaches, the

forward solver is used in the minimization problem [136], and a low-contrast scenario is assumed such that the nonlinear problem is linearized. This results in less accurate solutions, especially for high-contrast cases [133, 136].

Another class of iterative methods are contrast source inversion (CSI) and gradient-based methods. In the CSI algorithm, the minimization problem involves two equations referred to as the data and the object equations [137, 138]. In this formulation, the cost functions consist of two terms and they are are solved such that the distribution of contrast sources and the distribution of the parameters are iteratively updated [138]. In the local gradient-based methods, e.g., Newton-type methods, the cost function is minimized through an iterative process. The modified Newton method [139] and Gauss-Newton (GN) method [140, 141] are examples of such methods.

In addition to the gradient-based methods (which only have search domains in the direction of the gradients), the global methods can also be employed to solve the problem. In the global methods, known as evolutionary algorithms, the search domain is not limited and expands to the entire domain, allowing for global minima rather than local minima to be found. These methods include genetic algorithms (GA) [142, 143] and particle swarm optimization (PSO) [143, 144]. The global algorithms are known to have higher computational cost compared to local methods and this makes their applicability limited.

Gradient-based methods of the same type as used in this thesis are usually formulated as a non-linear optimization problem where the objective is to determine the unknown material parameters by iteratively minimizing a cost function. It can for example be formulated in terms of the squared complex-valued wave number k^2 in (2.14). The dielectric properties in the region of interest are embedded in k^2, and therefore permittivity and conductivity images are attainable.

Figure 3.1 offers an overview of the reconstruction algorithm implemented in the thesis [145]. This kind of iterative reconstruction algorithm is usually formulated as an ordinary least-square (OLS) minimization problem:

$$\min_{k^2} F(\epsilon, \sigma) := ||E^m - E^c(k^2)||^2 \tag{3.1}$$

where E^m is the measured complex electric field and E^c is the corresponding calculated electric field. Measured data are collected with the help of an array of antennas that surrounds the object under investigation. The measurement data are collected by letting each element in the array of antennas transmit, one by one, at the same time as the remaining antennas operate in receiver mode to measure the scattered electric field. In this way, measurements for each possible antenna pair are made and used to solve the reconstruction problem in (3.1).

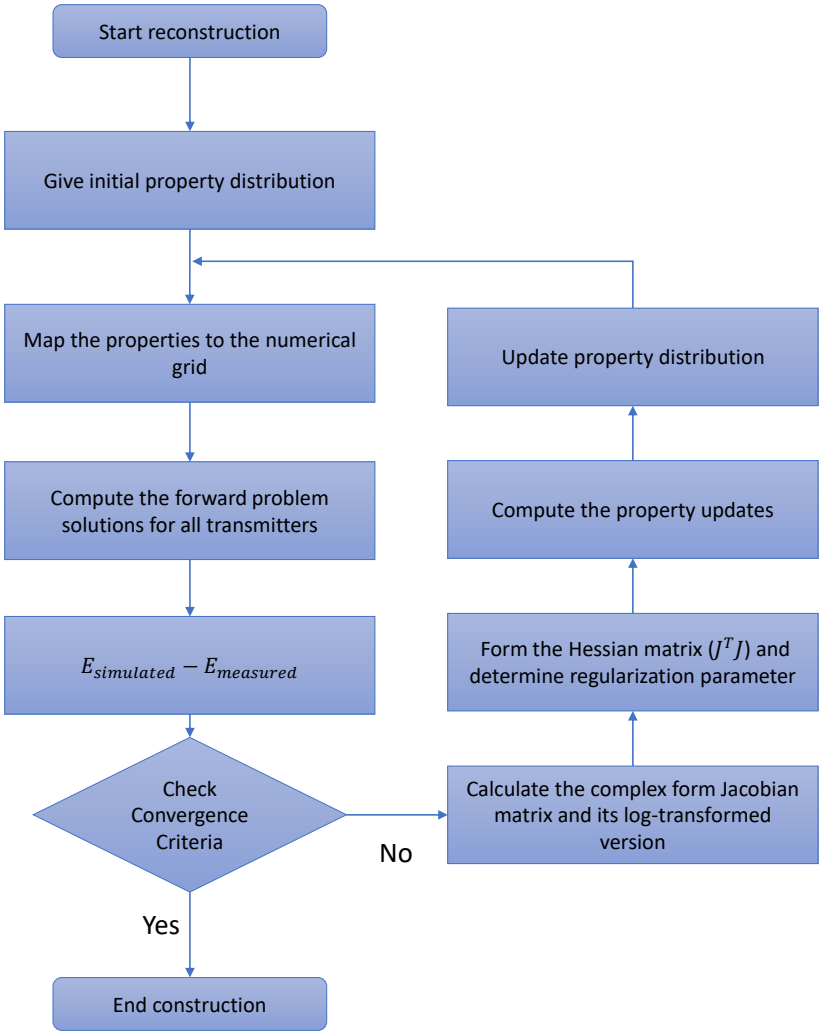

Figure 3.1: Overview of the microwave tomography algorithm.

3.2.2 Log-magnitude and phase reconstruction algorithm

The minimization problem in (3.1) aims at finding the value of k^2 that minimizes the sum of squares of the residuals between the measured and calculated log-magnitude and phase parts of electric fields. Meaney et al. [146] investigated if there are suitable transformations of the OLS problem that may improve the performance of the algorithm. They concluded that without loss of generality the optimization problem in

(3.1) can be formulated as a least-square minimization problem in logarithmic scale (OLS_{log}) with an overall improved performance and rewritten as [146]

$$\min_{k^2} f(k^2) := ||\Gamma^m - \Gamma^c(k^2)||^2 + ||\Phi^m - \Phi^c(k^2)||^2 \tag{3.2}$$

where $\Gamma^m, \Gamma^c, \Phi^m$, and Φ^c are the log-magnitudes and phases for the measured and computed electric fields, respectively. In an ideal case, the minimization problem is solved such that the measured electric fields perfectly match with the computed fields, and the remaining residual is zero. However, this can rarely be realized in practice; instead, the minimization has to be terminated when the residual has reached a specified tolerance level.

The Gauss-Newton algorithm is a well-known gradient-based solver for the non-linear least squares (NLLS) problem and will be discussed in the next section.

3.2.3 Iterative Gauss-Newton algorithm

In the Gauss-Newton method, the Taylor expansion is used to linearize the residuals. Using only the first order Taylor expansion of the calculated electric fields $E^c(k^2)$ gives the following linearization: [147]

$$E^c(k^2_{bath} + \Delta k^2) \approx E(k^2_{bath}) + J_0 \Delta k^2 \tag{3.3}$$

where k^2_{bath} is the squared wave number for the homogeneous bath, Δk^2 expresses changes in properties to the bath in the imaging domain, $E(k^2_{bath})$ is the electric field in the homogeneous bath, and J_0 is the Jacobian matrix at the 0^{th} iteration. The Jacobian matrix describes the changes in the electric fields at the antenna locations with respect to the changes of Δk^2. Iteratively refined estimates of Δk^2 can be calculated with the following formula: [147]

$$\Delta k^2_{new} = \left(J^*_{old} J_{old}\right)^{-1} J^*_{old} \left(E^m - E^c(k^2_{old})\right) \tag{3.4}$$

Here, the measurements E^m are assumed to be true values for the electric fields, J and J^* denote the complex Jacobian matrix and its conjugate transpose, and the properties in each iteration are updated as [148]

$$k^2_{new} = k^2_{old} + S \Delta k^2_{new} \tag{3.5}$$

where the indices *old* and *new* refer to the iterative process. The step size S is typically in the interval $(0, 1)$ and set empirically.

Recovering the properties with the log-magnitude scheme (3.2), requires multiple changes to the scheme in (3.4) and (3.5). To begin, (3.4) is modified in terms of the log-magnitude and phase parts of the electric field, yielding

$$\Delta k^2_{new} = \left(J^*_{old} J_{old}\right)^{-1} J^*_{old} \begin{Bmatrix} \Gamma_{E_m} - \Gamma_{E_c}(k^2_{old}) := \Gamma^m - \Gamma^c(k^2_{old}) \\ \Phi_{E_m} - \Phi_{E_c}(k^2_{old}) := \Phi^m - \Phi^c(k^2_{old}) \end{Bmatrix} \tag{3.6}$$

The log-magnitude and phase of electric fields are approximated using the first order Taylor expansion (3.3) with respect to the real and imaginary parts of the complex k^2 [149]. With the complex k^2 divided into real and imaginary parts ${k_R}^2$ and ${k_I}^2$, (3.6) can be written as [149]

$$\begin{Bmatrix} \Delta k^2_{R,new} \\ \Delta k^2_{I,new} \end{Bmatrix} = \left(J^*_{old} J_{old}\right)^{-1} J^*_{old} \begin{Bmatrix} \Gamma^m - \Gamma^c(k^2_{R,old}, k^2_{I,old}) \\ \Phi^m - \Phi^c(k^2_{R,old}, k^2_{I,old}) \end{Bmatrix} \tag{3.7}$$

We note that the relations (3.6)-(3.7) are only presented here for clarification of the log-magnitude and phase format optimization problem and are not numerically valid with respect to the size of matrices, and the actual update equation is given in Section 3.2.5. The next step is to construct the complex Jacobian matrix and its real format for the log-magnitude electric field and phase of formulation. This will be discussed in the next two sections.

It is worth noting that the Gauss-Newton method only uses the first-order partial derivatives, which is an advantage over the Newton method, which requires the second derivatives [143].

3.2.4 Complex format of the Jacobian

For the tomographic algorithms, calculation of the Jacobian matrix is related to the forward solver and the discretization of the domain. Fang et al. [150] explored the dual mesh-based nodal adjoint method derivation of the Jacobian matrix. In this method, the Jacobian matrix is calculated from the matrix of basis functions (ϕ) times a forward solutions vector (E_s), and then results are multiplied by a solutions vector (E_r), where E_s and E_r are the electric field values due to sources from both antennas s and r. Such a method is typically applied to the FE method. Here, an expansion of the nodal adjoint method is used to form the Jacobian matrix efficiently. The nodal adjoint method for a dual mesh scheme and its expansion on a single domain used for both forward solutions and parameter reconstruction is described in Paper C.

In the expansion of the nodal adjoint method, each row in the Jacobian is reduced to a simple multiplication of the two vector forward solutions due to sources from antennas s and r and also multiplied by a constant,

$$J(s, r) = C E_s \cdot E_r \tag{3.8}$$

where E_s and E_r are the electric field values at all nodes in the parameter mesh due to sources at the locations s and r, and C is a constant. The Jacobian matrix in (3.8) is complex and describes the changes in the field distributions due to a small change in the parameter k^2.

3.2.5 Log-magnitude and phase transformation of the Jacobian

Let us consider the log-magnitude and phase optimization problem in (3.2) with iterative solutions in the form of (3.7). The derivation of the log-magnitude and phase format for the Jacobian matrix is performed with respect to the real and imaginary parts of k^2 [149]. This means that the derivatives for the log-magnitude and phase electric field values due to the change in k^2 are analyzed for real and imaginary parts of k^2 denoted ${k_R}^2$ and ${k_I}^2$, respectively. Meaney et al. [149] calculated the derivatives and showed that the log-magnitude and phase Jacobian matrix, J^{LMPF}, is comprised of four separate real terms as

$$J^{LMPF} = \begin{bmatrix} \partial k_R \Gamma_E & \partial k_I \Gamma_E \\ \partial k_R \Phi_E & \partial k_I \Phi_E \end{bmatrix} \tag{3.9}$$

where ∂k_R and ∂k_I represent first derivatives of the calculated solutions with respect to each element of ${k_R}^2$ and ${k_I}^2$ in the parameter mesh. As an example, each element of $\partial k_R \Gamma_E$ is made up of $\partial k_{Ri} \Gamma_{Ej}$, where the index i refers to the number of nodes in the parameter mesh and the index j refers to the number of measurements. The first set of elements in the matrix in (3.9) is expressed as [149]

$$\partial k_{Ri} \Gamma_{Ej} = \frac{E_{Rj} \partial k_{Ri} E_{Rj} + E_{Ij} \partial k_{Ri} E_{Ij}}{E_{R_j}^2 + E_{I_j}^2} \tag{3.10}$$

where the log-magnitude and phase derivatives in (3.10) are described with respect to the real and imaginary parts of the electric field, i.e., E_R and E_I, respectively. The three remaining sets of elements in J^{LMPF} are also formed similarly and are explained in [149].

Given the log-magnitude and phase format of the Jacobian matrix, the iteratively updated solution (3.7) to the minimization problem (3.2) becomes

$$\begin{Bmatrix} \Delta k_{R,new}^2 \\ \Delta k_{I,new}^2 \end{Bmatrix} = \left(J_{old}^T J_{old} \right)^{-1} J_{old}^T \begin{Bmatrix} \Gamma_{E_m} - \Gamma_{E_c}(k_{old}^2) := \Gamma^m - \Gamma^c(k_{old}^2) \\ \Phi_{E_m} - \Phi_{E_c}(k_{old}^2) := \Phi^m - \Phi^c(k_{old}^2) \end{Bmatrix} \tag{3.11}$$

where J and J^T are the real log-magnitude and phase format Jacobian matrix and its transpose, respectively.

3.2.6 Regularization scheme

The purpose of a regularization technique is to transform an ill-posed problem into a well-posed one by restricting the possible solutions and forcing it into a priori known shapes [151]. In microwave tomography, only a limited number of observations, referred to as measurement data, are available. This deteriorates image uniqueness

and data independence properties and results in an ill-posed inverse problem. In an ill-posed problem, the use of regularization is essential to the success of image reconstruction.

Tikhonov regularization is a common regularization technique applied to ill-posed problems [152]. In this method a penalty term is usually added to the cost function (3.1). However, in microwave tomography algorithms, the regularization is often instead performed by regularizing the solution-update, i.e., Δk^2 in (3.4) [133]. In this way, the update to solution (3.11) is then found as

$$\begin{Bmatrix} \Delta k^2_{R,new} \\ \Delta k^2_{I,new} \end{Bmatrix} = \left(J^T_{old} J_{old} + \alpha_{tik} L^T L\right)^{-1} J^T_{old} \begin{Bmatrix} \Gamma^m - \Gamma^c(k^2_{R,old}, k^2_{I,old}) \\ \Phi^m - \Phi^c(k^2_{R,old}, k^2_{I,old}) \end{Bmatrix} \tag{3.12}$$

Here, the identity matrix I is chosen as the regularization matrix such that $L^T L = I$, and the parameter $\alpha_{tik} > 0$ is also chosen such that it decreases iteratively and is proportional to normalized errors of the calculated electric fields at the measurement sites. The parameter α_{tik}, described in detail in [153] and [154], is formed as

$$\alpha_{tik} = \beta \; E_r \; \frac{Trace(D^T D)}{N} \tag{3.13}$$

where the arbitrary parameter β has a value in the range of $(0, 1)$, $Trace()$ refers to the sum of the diagonal elements of a matrix, D is the diagonal of the Jacobian matrix J, D^T is the diagonal of J^T, and N is the number of reconstruction parameters, i.e., nodes in the parameter mesh. The parameter E_r is the relative error of the field values (magnitude and phase) normalized to the relative error of the 0^{th} iteration (E_{rr0}, i.e., the starting error), and is calculated as

$$E_r = \sqrt{\frac{||E^m - E^c||^2}{||E_{rr0}||^2}} \tag{3.14}$$

where $||\cdot||$ denotes the Euclidean norm.

Levenberg-Marquardt regularization is also a well-known regularization technique that has been applied to the ill-posed tomographic algorithm [149]. Marquard [155] proposed an algorithm for least-square estimation of non-linear parameters in a optimization problem formulated as in (3.2). It has been shown that solution (3.11) to the optimization problem (3.2) can be reformulated as [155]

$$\left((J^T_{old} J_{old})^* + \lambda I\right) \begin{Bmatrix} \Delta k^{*2}_{R\ ,new} \\ \Delta k^{*2}_{I\ ,new} \end{Bmatrix} = \left(J^T_{old} \begin{Bmatrix} \Gamma^m - \Gamma^c \\ \Phi^m - \Phi^c \end{Bmatrix} \right)^* \tag{3.15}$$

where I is the identity matrix, and the arbitrary parameter $\lambda > 0$ is added to all diagonal terms. The notation of (3.15) can be simplified as

$$\big(H^* + \lambda I\big)(\Delta k^{2*}_{new}) = d^* \tag{3.16}$$

where H^* and d^* are a scaled matrix and vector, respectively, such that

$$H^* = (h^*_{ij}) = \big(\frac{h_{ij}}{\sqrt{h_{ii}}\sqrt{h_{jj}}}\big) \tag{3.17}$$

$$d^* = (d^*_i) = \big(\frac{d_i}{\sqrt{h_{ii}}}\big) \tag{3.18}$$

where i and j denote the indices of matrix elements. After solving (3.16) for Δk^{2*}_{new}, the updated solution vector needs to be unnormalized such that

$$\Delta k^2_{new} = (\Delta k^2_{new,i}) = \big(\frac{\Delta k^{2*}_{new,i}}{\sqrt{h_{ii}}}\big) \tag{3.19}$$

The applied regularization scheme can be summarized as follows. First, the α_{tik} term is added to the diagonal of the Hessian matrix H. Next, the new matrix is normalized as given by (3.17), and the λ constant is added to all diagonal terms. The right-hand vector d is also normalized as in (3.18). Finally, after solving for the unknowns, the new vector is unnormalized as in (3.19).

3.2.7 Unwrapping procedure for phase

The idea of unwrapping is to map the phase values into only a $-\pi$ to $+\pi$ Riemann sheet so that the changes in phase between iterations are limited to the $-\pi$ to $+\pi$ range. The phase unwrapping procedure for the log-magnitude and phase optimization problem was previously applied to microwave breast tomography by the Dartmouth imaging group [149, 156]. Meaney et al. [157] report in detail how the procedure is done for both measured and computed cases. Grzegorczyk et al. also applied the phase unwrapping to the microwave tomographic imaging [158].

To calibrate the data, the measured electric field values (i.e., magnitudes and phases) for the homogeneous bath are subtracted from the actual measurements in the presence of the object. This is done for all pairs of transmitter/receiver antennas. Unwrapping of phases is applied to the calibrated measured and the computed phases. For the computed phases, at each iteration the phases are compared with values from the previous iteration. If the differences are greater than π, multiples of 2π are subtracted from the more recent iteration until the differences reach the $-\pi$ to $+\pi$ range. For the measured phases at a single frequency, multiples of 2π are subtracted from the measured phases greater than π to make sure that they are within the $-\pi$ to $+\pi$ range.

3.2.8 Reconstructed images with synthetic data

The log-magnitude and phase reconstruction algorithm based on the 2D DDA is discussed in detail in Paper D, which demonstrates and exemplifies the image reconstruction algorithm and results. Computation times for the Jacobian matrix and the complete reconstruction process are also reported and discussed.

This section describes and illustrates the calibration and image reconstruction procedures. Examples of reconstructed images are also shown, where synthetically generated data from a FE-based solver (COMSOL Multiphysics) are used as measurements. Given the synthetic simulated data, relative permittivity and conductivity values are reconstructed with the iterative Gauss-Newton algorithm.

As was described, in the calibration procedure, the signals received for the homogeneous domain are subtracted from the signals for the inhomogeneous solutions. The calibrated data are used as measured data. When one antenna transmits, all the remaining antennas receive. A set of calibrated received data is called a projection. These projections are separated into magnitude Γ_m in dB and phase Φ_m in degrees. The amplitude and phase projections of the observed signals, i.e., two sets of 16×15 observations for all combinations of transmitters/receivers, are used as the known measurement data. Figure 3.2 shows the schematic representation for a study case from Paper D. In this configuration, the background relative permittivity has value of $\epsilon_{r,b} = 25.4$, with conductivity $\sigma_b = 1.44$ (S/m) at 1.3 GHz. Two cylindrical objects are used as targets in the imaging zone. The permittivity of Object 1 is $\epsilon_{r,obj} = 18.5$, with a conductivity of $\sigma_{obj} = 0.9$ (S/m); the object is positioned at $x = -3.0$ and $y = 3.0$ cm and has a diameter of $d = 2.0$ cm. The permittivity of Object 2 is $\epsilon_{r,obj} = 30$, with a conductivity of $\sigma_{obj} = 1.8$ (S/m); the object is positioned at $x = 2.0$ and $y = -2.0$ cm and has a diameter of $d = 3.0$ cm.

For the synthetic data generated with the FE-solver, the electric fields are considered to be noisy to resemble a real-case measurement scenario with noise. To generate noisy simulated measured data, noise is added to the measurements to both the homogeneous measurements and inhomogeneous measurements, assuming that the transmit antenna transmits 0 dB, i.e., 1 mW. Noise is added at multiple power levels of -120, -100, and -80 dBm, to illustrate realistic conditions. This method for generating noisy data is similar to that in Meaney et al. [146].

Figure 3.3 presents the magnitude and phase projections at relative receivers for transmitters #1, #5, #9, and #13. This means that the relative receiver antennas for numbering the antennas on the x-axis of the plots are used. For example, if antenna #11 transmits, the antennas placed next (in a clockwise direction) i.e., antennas #12 to #16 and #1 to #10, are considered relative receivers and are numbered relative receivers #1 to #15, as presented in Figure 3.4.

The 1.3 GHz reconstructed relative permittivity and conductivity images as a function of iteration number are shown in Figure 3.5. We observe that the circular objects appear in the relative permittivity and conductivity images in all iterations.

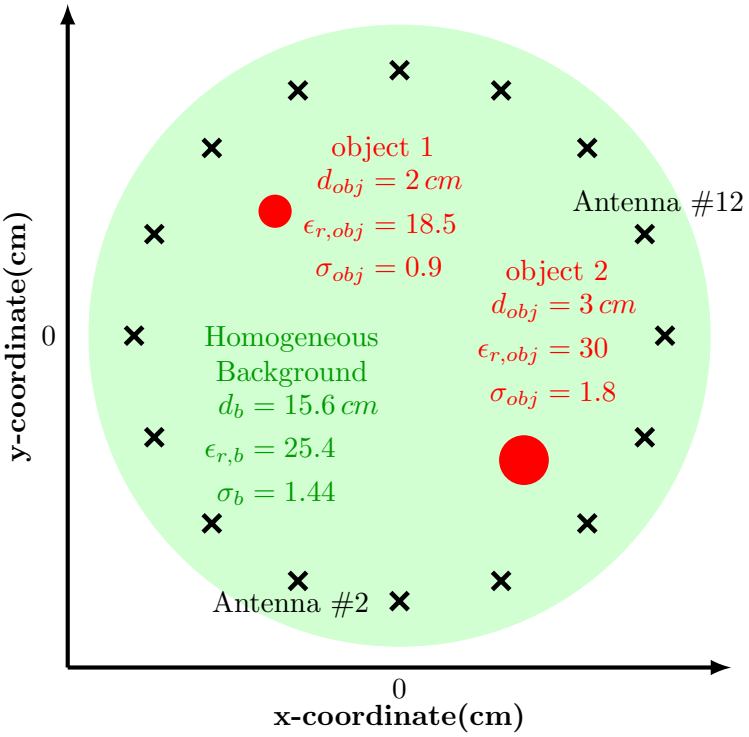

Figure 3.2: Schematic representation of the simulation setup. Two circular objects at (2,-2) and (-3,3) cm. The image is from Paper D.

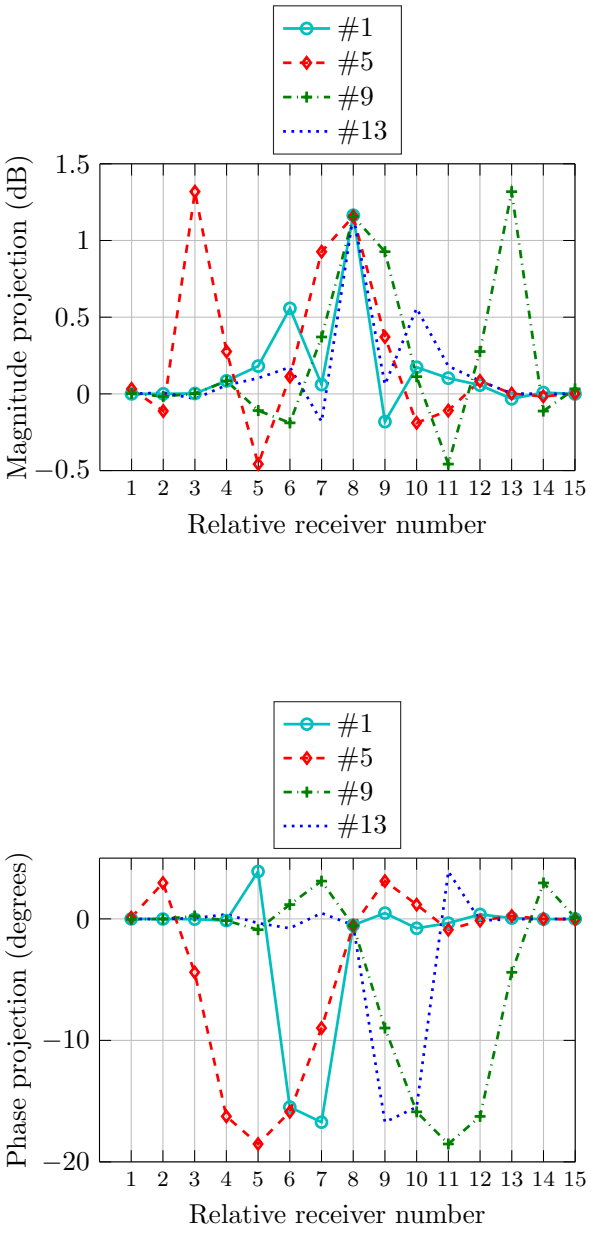

Figure 3.3: Magnitude and phase projections for four transmitters. Projections are calculated via the 2D-DDA.

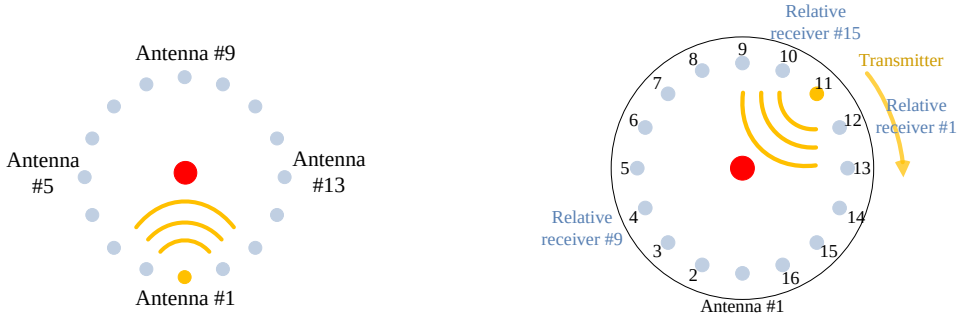

(a) Global antenna numbering (b) Relative antenna numbering

Figure 3.4: Schematic representation of the antenna array. The images are from Paper D.

The actual and reconstructed values on the cross sectional lines through Object 2 are shown in Figure 3.6.

The relative root mean square error (rRMSE) is a quantitative measure of the image reconstruction accuracy. The rRMSE error $\tilde{\varepsilon}$ between the reconstructed and true dielectric properties in the imaging domain is defined

$$\tilde{\varepsilon} = \sqrt{\frac{1}{N}\sum_{i=1}^{N}\left(\frac{\epsilon_{r,R}^{i} - \epsilon_{r,e}^{i}}{\epsilon_{r,e}^{i}}\right)^{2}} \tag{3.20}$$

where $\epsilon_{r,R}^{i}$ and $\epsilon_{r,e}^{i}$ denote the reconstructed and exact relative permittivity at node i, and N is the number of nodes in the parameter mesh. A similar formula can be used for the conductivity images in case of a lossy medium. Table 3.1 shows the relative RMSE in percentage for reconstructed relative permittivty and conductivity in the imaging domain at the final iterations. The table shows that the image error is influenced by the noise level considered for these synthetic data.

Figure 3.7 shows calculated magnitude and phase projections at selected iterations together with the actual measured data. The projections converge to the measured projections, and the general pattern appears to be similar during the reconstruction.

Table 3.1: rRMSE for reconstructed parameters.

Reconstructed parameter	no noise	-120 dBm	-100 dBm	-80 dBm
Relative permittivity	3.5%	3.5%	3.8%	16.7%
Conductivity	5.9%	5.9%	6.0%	16.3%

The 2D reconstruction algorithm takes advantage of the simplicity and low computational cost compared to a 3D version. Even though the forward problem is typically the most time-consuming portion of a tomographic algorithm, employing the DDA

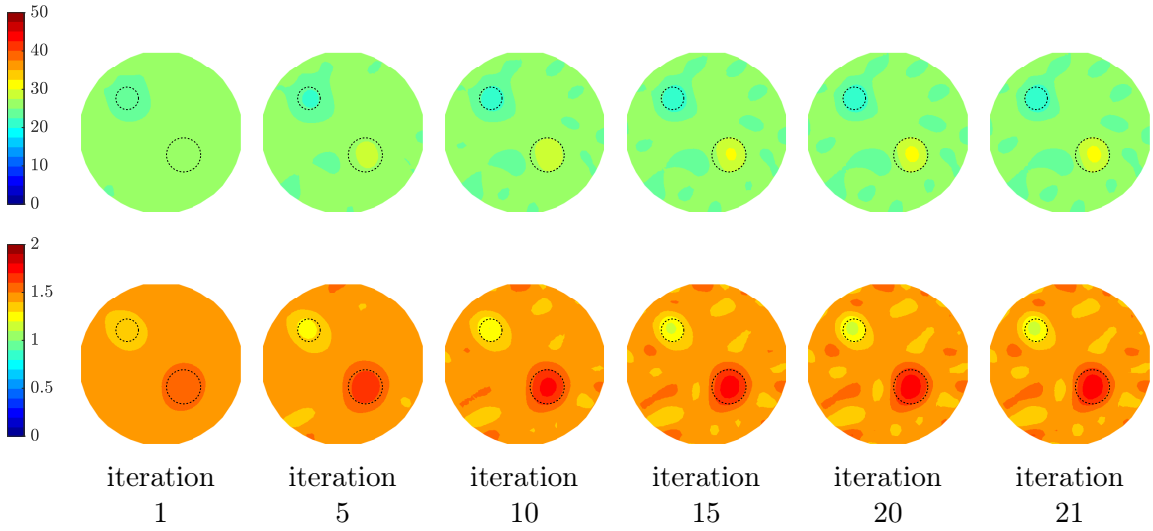

Figure 3.5: Images of reconstructed relative permittivity (top row) and conductivity (S/m) (bottom row) at 1.3 GHz as a function of iteration number. The FE solutions with noise level -100 dBm are used as measurements.

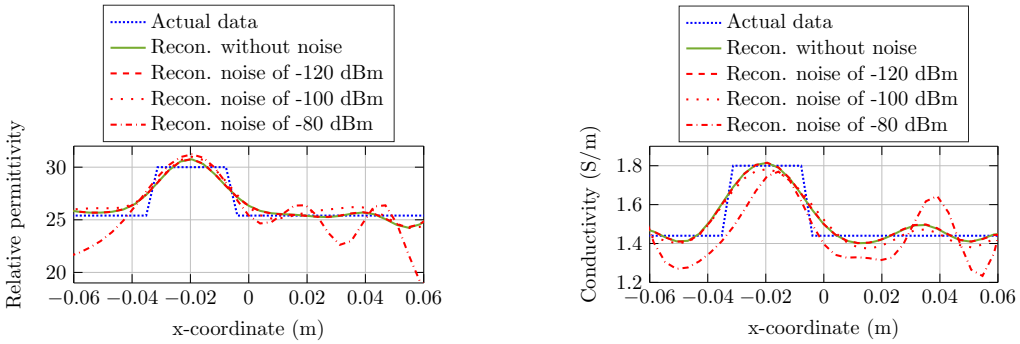

Figure 3.6: Reconstructed and actual data along the line through the center of Object 2 located at (2,-2) cm at a frequency of 1.3 GHz.

solver combined with FFT decreases the computational burden substantially. The iterative solver, preconditioned COCG-FFT, used for the forward solutions during the reconstruction, takes less than a second, which is considerably less than previous implementations such as FE and FDTD methods. It is worth pointing out that one reason for the speedup is the iterative nature of the algorithm. In each iteration of the reconstruction algorithm, the forward solution only changes marginally. The forward solutions are generated with the COCG-FFT method, which requires a starting estimate. In subsequent solutions, initial estimates from previous iterations can therefore be used to reduce the number of the COCG-FFT iterations and to improve the convergence speed of the forward solver itself as the reconstruction algorithm iterates and converges. It is also shown that preconditioning of the system can be used

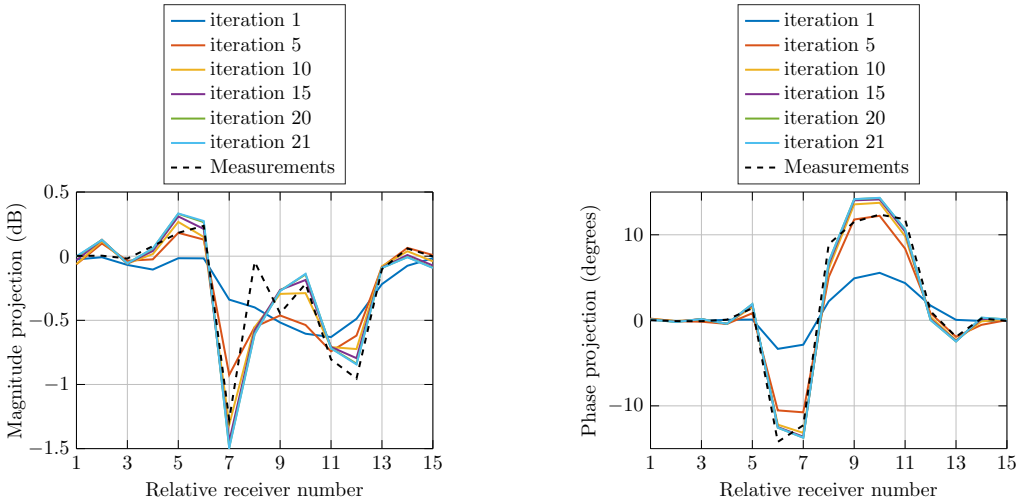

Figure 3.7: Comparison of calculated magnitude and phase projections of the signals transmitted from Antenna 1 for multiple iterations as a function of the receiver number. The FE solutions with noise level -100 dBm as the baseline measurements are also shown.

to moderate the convergence rate, and thus the computation time. In addition to the forward solver, the Jacobian matrix is also formulated such that the reconstruction time is not increased. Combination of the fast forward solver and the simple and efficient Jacobian matrix construction has resulted in image reconstruction on the order of 8 seconds for 20 iterations. The average computation time for each iteration in the image reconstruction for parameter mesh $N = 1085$ with 240 measurements is on the order of 0.42 seconds on a machine with a mobile processor ($\text{i7} - 4600$ U), 4 cores of 2.1 GHz and RAM of 8 GB. In Paper D, the computation times and memory requirements, run on a more advanced machine, are reported for both DDA and FE solvers.

Chapter 4

The Experimental System

This chapter reviews experimental microwave tomography systems and the principles of their functionality. The chapter also describes the Chalmers microwave breast imaging system used in the studies included in this thesis.

4.1 Overview

To summarize earlier discussions about principles of microwave tomography, the imaging domain is illuminated with microwave signals from multiple directions, and the resulting scattered signals are measured at multiple locations [44, 159]. The illumination is made by consecutive transmissions from one antenna at a time in an array of antennas enclosing the imaging region. Antenna arrays are often configured in a circular pattern, but other configurations are possible [44, 145, 160–163]. In the Chalmers system, all antennas act as both transmitters and receivers, where the antennas that are not currently transmitting act as receivers [162, 164]. Measurements are repeated until all possible combinations of transmitting and receiving antennas have been used. The acquired data are processed by an iterative algorithm to reconstruct the spatial dielectric map in the imaging domain. A schematic representation of such systems is illustrated in Figure 4.1.

The practical challenges that need to be addressed when building the experimental system are high signal power loss, limited penetration depth, low resolution, and a need for enormous computational resources for the image reconstruction algorithm [57]. These challenges have hindered the development process of real imaging systems and practical reconstruction algorithms for a long time. Most of the experimental study cases in biomedical microwave tomography indicate limitations in the use of measured data for successful image reconstruction. One challenge is the use of 2D reconstruction algorithms integrated with actual 3D measured data. The clinical prototype developed at Dartmouth College has been used successfully in 2D imaging [44]. The imaging group at Chalmers has also been able to produce 2D images using

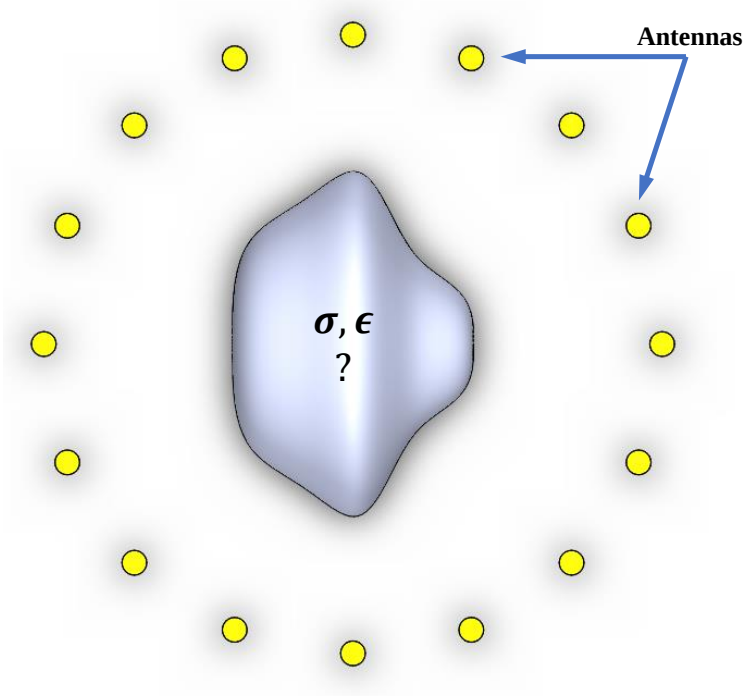

Figure 4.1: Schematic representation of an imaging system.

the 3D data acquired with the prototype system [162, 164].

4.2 Coupling medium

If a biological tissue is placed in air, it exhibits a significant contrast to the background and thus a high degree of scattering from the air/skin interface. With a lower coupling medium contrast, waves are better able to penetrate, allowing for higher signal strength inside the body. This makes possible more accurate measurements of signals that reach into the body. In microwave imaging it is important to optimize power penetration through the skin and into the body as well as efficient wave propagation between the antennas and the skin. The coupling liquid also has an impact on the image resolution. A better resolution (the smallest distinguishable pixel), requires a higher frequency, i.e., a shorter wavelength, albeit at the price of a shallower penetration depth. This in turn presents a challenge for imaging applications, especially for deep-body organs. Even the coupling liquid is usually lossy (conductive) and, in combination with the high losses in biological tissues, both the penetration depth and the usable frequency range are limited for every practical experimental system. Two hypotheses have been suggested and employed to enable deeper penetration [57]. The first approach is based on a principle introduced by Larson and Jacobi [50]. In their experimental setup, the antennas and the organ are immersed in water, which then

acts as a coupling liquid. Many different coupling liquids such as water, glycerin, and others have subsequently been explored. For example, the Dartmouth group used saline in their first clinical prototype [44]. However, the authors noted that a desirable medium should match the dielectric properties of the tissue. Saline with a high contrast can compromise the imaging ability by causing large reflections at the breast surface. To avoid this problem, Meaney et al. [44] proposed adjustments to saline as a coupling medium based on the properties of in vivo tissue. The coupling liquid used in the current imaging system is a mixture of glycerin and water. This coupling liquid also ensures that the surface waves and the undesirable multi-path signals are virtually eliminated by the high-conductivity nature of this liquid. The disadvantages of using coupling liquids at all include additional power loss in the wave propagation and additional complexity over a dry system in terms of maintenance and use [57]. The second approach is to place antennas in direct contact with the body to provide high coupling efficiency. In this case, signal power loss is less of an issue.

4.3 Phantoms and tissue-like media

Microwave imaging is based on the dielectric properties of breast tissue, so phantoms should be designed with similar permittivity and conductivity to breast tissue. Phantoms can be made out of liquids, e.g., glycerin [165], Triton X-100 [166], gels, e.g., [167], rubber-like mixtures [168], and solid materials, e.g., the GeePs-L2S phantom developed at the Supelec institute [166]. Among these phantoms, the glycerin-based phantoms and GeePs-L2S phantom have been tested in the imaging system at Chalmers [162, 164].

In this thesis, glycerin-water mixtures have been used as the phantom media, previously used in the imaging system at Chalmers [162,164]. The dielectric properties of such mixtures are related to their constituents' ratio and have been reported over the frequency range of 100 MHz - 25 GHz by Meaney et al. [165]. Glycerin-water mixtures are capable of representing breast tissue, i.e., adipose, fibroglandular, and tumors. To achieve this, various constituents' ratios and concentrations of mixture can be employed to characterize the dielectric properties of various breast tissues. The measured dielectric properties for selected glycerin-water ratio over the frequency range of 500 MHz - 2 GHz are presented in Figure 4.2. The measurements were performed with a dielectric probe (Agilent 85070 Performance Probe).

4.4 Chalmers/Dartmouth breast imaging system

The first clinical microwave breast tomography system was developed at Dartmouth College [44]. The system consisted of 16 monopole antennas configured into a circular

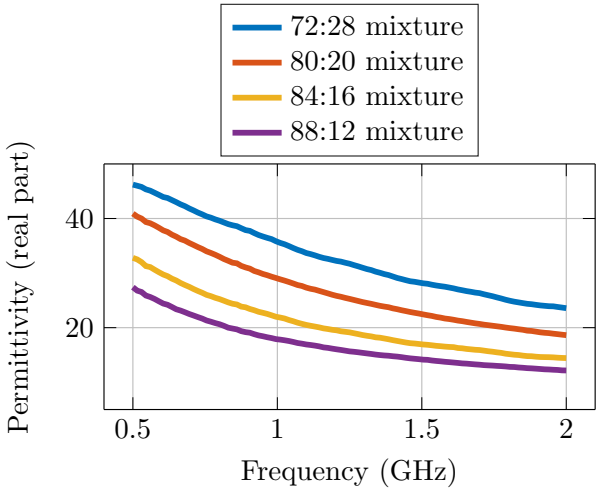

(a)

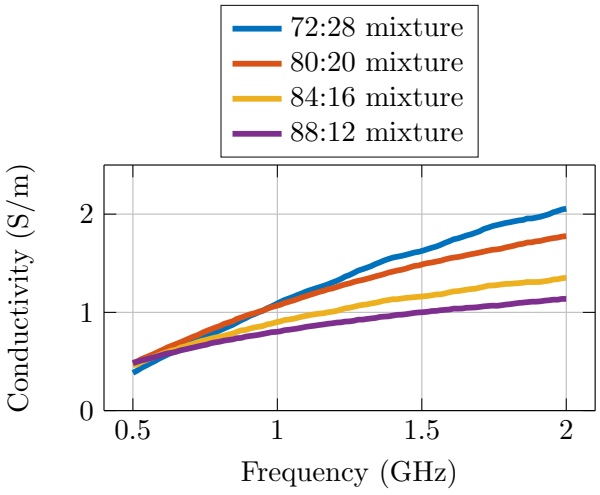

(b)

Figure 4.2: Dielectric properties of the glycerin-water mixtures measured via an external probe, (a) relative permittivity (real part), (b) conductivity (S/m).

array. A saline solution was used as coupling medium, and the system operated in the frequency range of 300 to 900 MHz. The antennas could move up and down, which enabled measurements of multiple cross-sections from the patient chest wall to the nipple.

Since then, several generations of systems have been developed at Dartmouth [44,52]. Recently, researchers at Chalmers built a system based on the same principles [162, 164]. That system comprises 16 antennas in a equiangularly spaced circular configuration of diameter 15.2 cm. The antennas are mounted in a tank filled with the coupling liquid, in this case a mixture of glycerin and water. Figure 4.3 shows the measurement system. The antennas are visible in the tank and connected to the Rohde & Schwarz ZNBT8 16 channel vector network analyzer (VNA). The VNA operates in the frequency range 9 kHz to 8.5 GHz and has a dynamic range up to 140 dB.

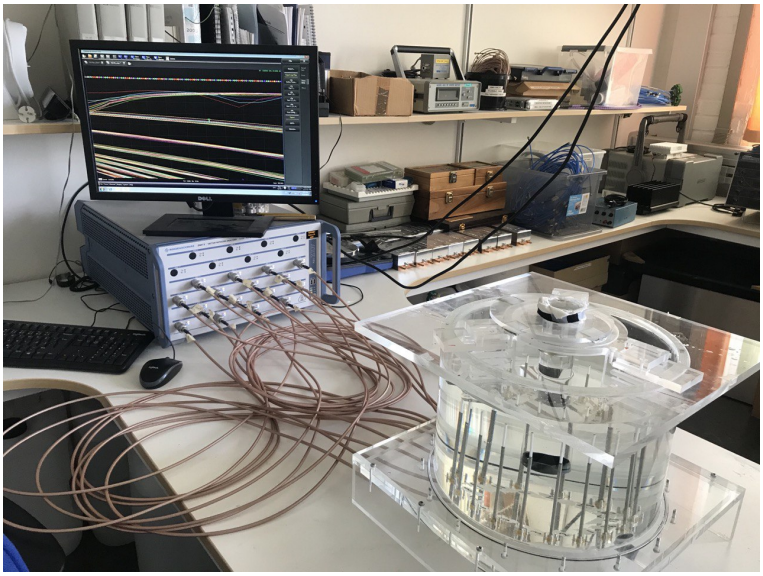

Figure 4.3: The imaging system at Chalmers University of Technology. The image is from Paper D.

4.4.1 2D imaging and the Chalmers/Dartmouth system

The Dartmouth research group has succeeded in producing 2D and 3D images of breasts, in both experimental and clinical studies [44,157,169]. Although 2D imaging has limitations, Meaney et al. [169] conclude that 2D imaging certainly remains an attractive solution for this system. Their extensive studies on 2D and 3D imaging algorithms prove that 2D is a suitable approximation in this system. They conclude that two main factors have made 2D imaging of this system feasible. First, the antennas are small and placed close to the target. In principle, wave propagation

from an antenna has to be described in 3D. However, the closer antennas are to each other, the more accurate a 2D representation of the field propagation between them. The second factor that has made imaging this system feasible is the use of a lossy bath. When part of the signal propagates out of the desired imaging plane, by the time it reflects back into the plane, it is quite heavily attenuated. This suggests that out-of-plane contributions are minimized. Previous studies at Dartmouth [157] also indicate that the 2D computed data match the 3D measurement data well, and since the inverse algorithms minimize the difference between the measured and computed values, use of 2D algorithms is considered a cost-effective and feasible option for fast breast imaging.

4.4.2 Reconstructed images with experimental data

The 2D DDA-based tomographic algorithm and the reconstructed images are discussed in detail in Paper D. The current section shows an example from that paper to demonstrate image reconstruction with real measured data from the Chalmers imaging system. In this case, the imaging tank is filled with a mixture of 80% glycerin and 20% water. A cylindrical phantom with a diameter of 4 cm is positioned in front of antennas #6 and #7. It is filled with an 84:16 glycerin-water mixture. The measurement setup is shown in Figure 4.4.

At 1.5 GHz, the dielectric properties corresponding to the different water-glycerin mixtures in the imaging tank and phantom object are $\epsilon_{r,b} = 20.9$, $\sigma_b = 1.35$ (S/m), $\epsilon_{r,obj} = 16.9$, and $\sigma_{obj} = 1.15$ (S/m), respectively.

Figure 4.5 shows the reconstructed relative permittivity and conductivity images as a function of iteration number. The circular object is visible in both permittivity and conductivity images in all iterations at an off-centered position. The sequence of images illustrates how the algorithm locates the object in the first few iterations and then gradually refines it.

Figure 4.6 shows the magnitude and phase projections due to a single transmitter at selected iterations and compares them to the actual measured data. The projections at all iterations are of similar shapes as the measured data and monotonically converge towards them. Figure 4.7 shows how the error of the optimization process, defined as in (3.14), decreases with increasing iteration number. This is also an illustration and confirmation of the convergence of the iterative reconstruction algorithm, where the error drops to 0.135 in 18 iterations from a normalized value of 1 at the start. The stopping criterion is met when the decrease in error from one iteration to the next is less than 1e-3.

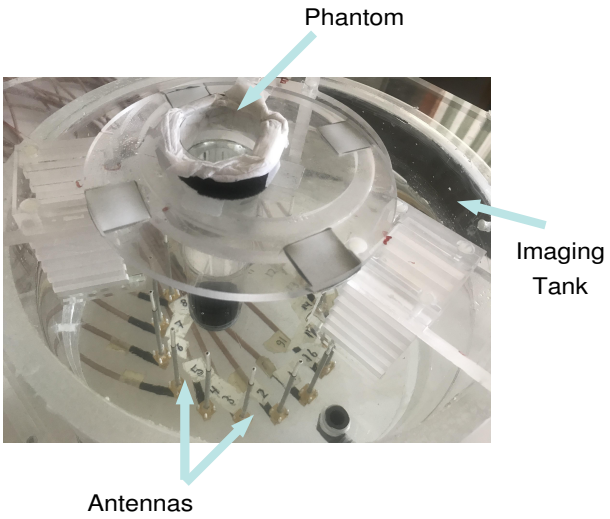

Figure 4.4: The photograph of the measurement setup for the case with a cylindrical inclusion positioned close to antennas #6 and #7. The image is from Paper C.

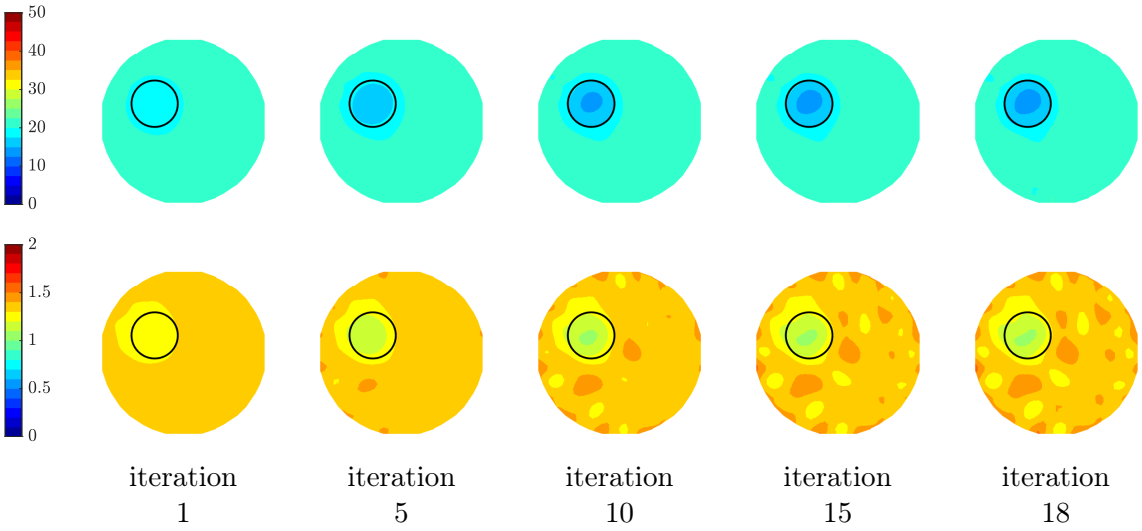

Figure 4.5: Images of reconstructed relative permittivity (top row) and conductivity (S/m) (bottom row) at 1.5 GHz as a function of iteration number. The images are from Paper C.

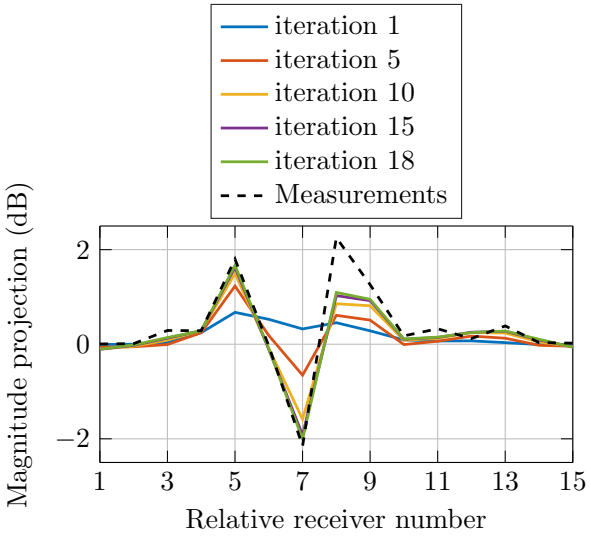

(a)

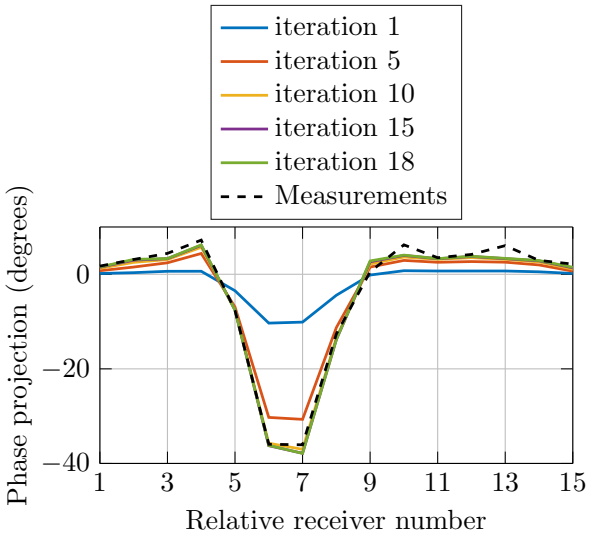

(b)

Figure 4.6: Comparison of calculated (a) magnitude and (b) phase projections of the signals transmitted from Antenna 1 for multiple iterations as a function of receiver number. The actual measurement projection is also shown. The figures are from Paper C.

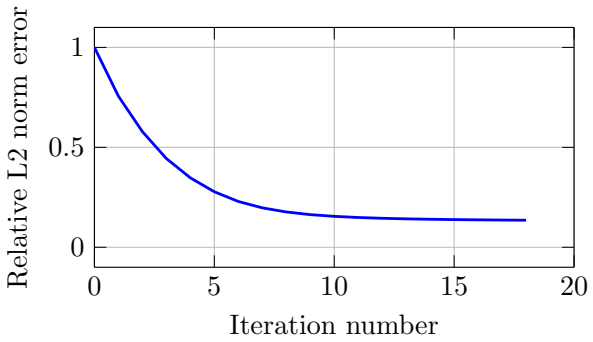

Figure 4.7: Computed relative $L2$ norm error of projections for the experimental study as a function of iteration number. The figure is from Paper C.

Chapter 5

Summary of Papers

5.1 Paper A

In this paper, the novel concept of 2D DDA is introduced and investigated for use as a numerical forward solver in microwave image reconstruction algorithms. The method is evaluated based on a numerical simulation study of breast tumor models. The primary motivation for developing this method is its potential to decrease the computation time. Computation times for 2D DDA are investigated extensively in Paper B.

Paper A starts by formulating the 2D DDA for electric field distributions. A formula for adequate sampling grid size and number of dipoles is proposed based on existing formulas for the 3D case. Three different parameters and their contributions to the accuracy of the 2D DDA are studied. The three parameters are:

- number of dipoles;
- inclusion size;
- dielectric contrast of inclusion.

The finite element solutions from COMSOL Multiphysics software are used to generate simulated baseline results to benchmark the DDA simulations. Measured data acquired from the breast imaging system at Chalmers are also used. The results show that DDA, FE COMSOL, and measurements are comparable regarding both magnitude and phase distributions. We conclude that 2D DDA is accurate for relatively large objects with high contrast permittivity properties when employing the adequate number of dipoles representing the geometry. Thus, the 2D DDA is potentially a very powerful forward solver to include in image reconstruction algorithms. It has the potential to outperform computation times of more conventional FDTD or FE forward solvers.

5.2 Paper B

This paper focuses on computational aspects of the 2D DDA, exploring formulations and the possibility of integrating these with the microwave imaging system.

Paper B starts with a detailed description of the formulations. Next, a system of equations arising in 2D DDA is investigated with the aim of deducing an efficient solution strategy. The iterative conjugate gradient type algorithms, such as the COCG method, are tested and found efficient. The efficiency in each iteration is limited by a matrix-vector multiplication. The matrix-vector multiplication step is formulated in terms of a block Toeplitz matrix, which is particularly favorable for reducing the overall computation time. The idea is to expand each Toeplitz matrix into a circulant matrix, apply the convolution theorem, and utilize the FFT. Additionally, the performance vs. accuracy of the forward solver is studied to optimize the efficiency and accuracy with respect to grid size, number of dipoles, polarizability formulations, and mathematical formulation of the master equation of the DDA.

The results show that this formulation is both accurate and efficient. Comparison of computation times among direct solvers, iterative solvers (COCG and COCR), and the iterative solvers using the FFT (COCG-FFT and COCR-FFT) indicates that this approach significantly decreases the computation time.

To optimize the computational efficiency even further, the grid size and tolerance level in the iterative algorithms are analysed. The results show that the iterative solvers combined with the FFT, suitable grid size, and adjusted tolerance level reduce the computation time of the forward problem to about 0.1 seconds from 57.8 seconds for a direct solver implemented in C++.

5.3 Paper C

The most time-consuming part of the image reconstruction algorithm is the forward problem, and the major portion of time is spent on repeated forward simulations. The second most time-consuming part is the computation of the the Jacobian matrix. Paper C describes a simple and efficient way to calculate the Jacobian matrix. Our formulation is based on the nodal adjoint method previously employed by the Dartmouth imaging group in dual-mesh scheme imaging scenarios. In this case, however, no dual-mesh scheme is used and instead the forward solution mesh and parameter mesh coincide. This novel development is meant to optimize the computational complexity of calculating the Jacobean as much as possible. The Jacobian matrix calculated from the 2D DDA is compared to corresponding computations based on the finite element solutions. The calculation of the Jacobian matrix for the log-magnitude and phase optimization problem is done in two steps. First, the complex Jacobian is calculated. Second, its log-magnitude and phase transformations are calculated.

The comparison of DDA and FE-based Jacobian matrices includes investigating accuracy and computational cost. The comparison shows that our formulation is as accurate as the nodal adjoint method. The methods differ with respect to their magnitudes, but the overall patterns of both Jacobian matrices on the imaging domain are in agreement. As an effect of using the same uniform grid for parameter estimation and forward solution, the calculation of a single row of the complex Jacobian matrix is reduced to a simple vector-vector multiplication multiplied by a constant. Consequently, the computational costs are substantially reduced by several orders of magnitude and the time required to compute the Jacobian matrix is negligible.

5.4 Paper D

This paper proposes a fast microwave tomography reconstruction algorithm based on the 2D DDA (described in Papers A and B) and the efficient calculation of the Jacobian matrix (investigated in Paper C). For the first time image reconstruction with the 2D DDA method from experimental data is demonstrated. The main contributions of the paper include the following: development of the 2D DDA as a forward solver in a microwave imaging application, solving the forward solver with the preconditioned iterative solver combined with FFT, formulating and implementing the Jacobian matrix calculation using a single grid and using it for formulating the reconstruction algorithm as a log-magnitude and phase optimization problem, and demonstrating image reconstruction from simulated and experimental data acquired from breast microwave imaging recently re-built at Chalmers based on the Dartmouth imaging system.

This microwave tomography reconstruction algorithm combines the new forward solver with the log-magnitude and phase format of the optimization problem. The algorithm is tested with two types of data: synthetically simulated and experimentally measured data. These data sets are generated with an FE-based solver, COMSOL Multiphysics, and with the microwave breast imaging system at Chalmers. The simulation setup is designed to resemble the real case scenarios where multiple scatterers with different levels of contrast are present in the imaging domain. The paper also compares the computation times and memory requirements of FE- and DDA-based reconstruction algorithms.

The results show that the algorithm recovers information about position, size, and the relative permittivity and conductivity of scatterers in the imaging domain. Additionally, the algorithm does not have any difficulties with 2D imaging based on measured 3D data. The proposed image reconstruction algorithm is capable of reconstructing an image within a few seconds. The imaging domain has a diameter of 15.2 cm and 1085 nodes, and imaging takes about 8 seconds for 20 iterations. This implementation is a dramatic improvement over previous implementations (which require multiple minutes to hours), providing significant time savings and reduced

memory requirements.

Chapter 6

Conclusion and Future Work

The first part of this thesis studies the 2D DDA method, with a focus on its capability to simulate electric field distributions in a microwave imaging system. The results show that the 2D DDA can be an efficient and accurate forward solver. In Paper A, we have also proposed a formula that can be used to determine the minimum number of dipoles needed to generate a solution with adequate accuracy. The results also show that the method can handle a large contrast range within the forward model zone. However, larger targets with high contrast with respect to the background contribute to larger errors in the field distributions compared to smaller targets with lower contrast. In sum, the 2D DDA is found to be an accurate numerical method for computing the electrical field distributions for the microwave breast imaging system under study.

The main motivation for utilizing the 2D DDA is to reduce the computational complexity in the microwave tomography algorithm and produce images in seconds, where previously 3D implementations have ranged from minutes to hours, with the 3D DDA taking about 20 minutes. To enable such a significant reduction in the reconstruction time, Paper B shows that the linear system of equations arising from the 2D DDA can be solved using conjugate gradient-based iterative algorithms combined with the FFT. The proposed solver turns out to be highly efficient and can generate forward solutions in significantly less time than other traditional methods, like FDTD or FEM, on finely discretized grids. Whether the algorithm is implemented in an interpretive language such as MATLAB or a classic compiler-based code such as C++ impacts simulation times. Although the best performance is achieved with C++ code, MATLAB produces comparable results. Paper B concludes that the new proposed forward solver, the 2D DDA, is highly efficient and significantly decreases the computation time in a single forward solver.

The second part of this thesis implements a microwave tomographic algorithm and demonstrates how it can be used in clinically relevant systems to generate images in real time. To accomplish this, the second important portion of the imaging algorithm

known as the Jacobian matrix is formulated such that its built-up computational cost is not considerable. Within that construct, we examine how best to structure the forward solution grid and the parameter mesh as a means of optimizing the computation time required to form the Jacobian matrix, a key to reducing computation time. Paper C concludes that the computation time of a Jacobian matrix can be negligible when appropriate meshes and methods are used in the forward solutions and the parameter mesh.

After optimizing the forward solver and the Jacobian matrix computation, a log-magnitude and phase version of the microwave tomography algorithm is implemented. Paper D investigates the 2D tomographic imaging algorithm utilizing the 2D DDA forward solver and efficient Jacobian matrix based on the simple and efficient expansion of the nodal adjoint method. The results show that the algorithm has been successfully applied to image reconstruction, yielding a significant speedup over more conventional reconstruction methods. Paper D concludes that employing the 2D DDA and the log-magnitude and phase format of the reconstruction algorithm impacts both the computational complexity and the convergence behavior of the algorithm. The computation time and memory requirements are reduced such that the images are obtained in a few seconds with a possible minimal in-use memory.

The discrete dipole approximation is proved to be highly efficient as a forward solver and yet even more efficient when applied as a forward solver in microwave tomographic image reconstruction algorithms. This algorithm is particularly suitable for use in imaging situations when an image is required in real time. One such situation could be imaging of acute stroke or trauma patients in ambulances. Real time imaging of these patients and their brains already in the ambulances could potentially lead to more informed decisions at an early stage and thereby better care. Additionally, the use of DDA in medical imaging can lead to improvements in healthcare systems in developing countries where resources and computer power are more scarce. The DDA can also be used in industrial applications, such as food processing or other process industries where real-time monitoring of constituents, for example in pipes, are of interest. 2D DDA could very well provide the needed speed-up of image reconstruction that makes real-time imaging feasible.

To improve the images, there is still room to investigate other regularization schemes such as two-step regularization approaches tested in [157] to increase the accuracy of the images, especially when the contrast level in the domain is high. Additionally, even though we have tested multiple formulas from the literature for modeling the molecular polarizability, there is room for improvement. Fundamental knowledge of the involved physics and the relation to modeling particular imaging systems and scattering scenarios might prove to be of essence when developing new application areas and further improving speed, convergence rate, and accuracy.

Bibliography

[1] World Health Organization. [Accessed on 2020-05-12]. [Online]. Available: http://www.who.int/en/

[2] D. Munoz, A. M. Near, N. T. Van Ravesteyn, S. J. Lee, C. B. Schechter, O. Alagoz, D. A. Berry, E. S. Burnside, Y. Chang, G. Chisholm *et al.*, "Effects of screening and systemic adjuvant therapy on ER-specific US breast cancer mortality," *JNCI: Journal of the National Cancer Institute*, vol. 106, no. 11, 2014.

[3] D. A. Berry, K. A. Cronin, S. K. Plevritis, D. G. Fryback, L. Clarke, M. Zelen, J. S. Mandelblatt, A. Y. Yakovlev, J. D. F. Habbema, and E. J. Feuer, "Effect of screening and adjuvant therapy on mortality from breast cancer," *New England Journal of Medicine*, vol. 353, no. 17, pp. 1784–1792, 2005.

[4] American Cancer Society. [Accessed on 2020-12-12]. [Online]. Available: https://www.cancer.org/cancer/breast-cancer/screening-tests-and-early-detection/mammograms/limitations-of-mammograms.html

[5] S. H. Heywang-Köbrunner, A. Hacker, and S. Sedlacek, "Advantages and disadvantages of mammography screening," *Breast Care*, vol. 6, no. 3, pp. 199–207, 2011.

[6] E. C. Fear, S. C. Hagness, P. M. Meaney, M. Okoniewski, and M. A. Stuchly, "Enhancing breast tumor detection with near-field imaging," *IEEE Microwave Magazine*, vol. 3, no. 1, pp. 48–56, 2002.

[7] M. Lazebnik, D. Popovic, L. McCartney, C. B. Watkins, M. J. Lindstrom, J. Harter, S. Sewall, T. Ogilvie, A. Magliocco, T. M. Breslin, W. Temple, D. Mew, J. H. Booske, M. Okoniewski, and S. C. Hagness, "A large-scale study of the ultrawideband microwave dielectric properties of normal breast tissue obtained from reduction surgeries," *Physics in medicine & biology*, vol. 52, no. 10, p. 2637, 2007.

[8] Y. Cheng and M. Fu, "Dielectric properties for non-invasive detection of normal, benign, and malignant breast tissues using microwave theories," *Thoracic Cancer*, vol. 9, no. 4, pp. 459–465, 2018.

[9] A. N. Tikhonov, A. Goncharsky, V. Stepanov, and A. G. Yagola, *Numerical methods for the solution of ill-posed problems.* Dordrecht, Netherlands: Springer Science & Business Media, 1995.

[10] W. C. Chew, *Waves and fields in inhomogeneous media.* New York: IEEE Press, 1995.

[11] T. Isernia, V. Pascazio, and R. Pierri, "On the local minima in a tomographic imaging technique," *IEEE Transactions on Geoscience and Remote Sensing*, vol. 39, no. 7, pp. 1596–1607, 2001.

[12] A. Pettersson, S. E. Hankinson, W. C. Willett, P. Lagiou, D. Trichopoulos, and R. M. Tamimi, "Nondense mammographic area and risk of breast cancer," *Breast Cancer Research*, vol. 13, no. 5, p. R100, 2011.

[13] M. Lokate, P. H. Peeters, L. M. Peelen, G. Haars, W. B. Veldhuis, and C. H. van Gils, "Mammographic density and breast cancer risk: the role of the fat surrounding the fibroglandular tissue," *Breast Cancer Research*, vol. 13, no. 5, p. R103, 2011.

[14] www.breastcancer.org. [Accessed on 2020-12-12]. [Online]. Available: https://www.breastcancer.org/

[15] National Breast Cancer Foundation. [Accessed on 2018-12-12]. [Online]. Available: https://www.nationalbreastcancer.org/types-of-breast-cancer/

[16] American Cancer Society. [Accessed on 2020-12-12]. [Online]. Available: https://www.cancer.org/cancer/breast-cancer/understanding-a-breast-cancer-diagnosis/stages-of-breast-cancer.html

[17] P. Maisonneuve, "Epidemiology, lifestyle, and environmental factors," in *Breast Cancer.* Cham, Switzerland: Springer International Publishing, 2017, pp. 63–72.

[18] U. Veronesi, A. Goldhirsch, P. Veronesi, O. D. Gentilini, and M. C. Leonardi, *Breast cancer: Innovations in research and management.* Cham, Switzerland: Springer International Publishing, 2017.

[19] Global Cancer Observatory. [Accessed on 2020-03-14]. [Online]. Available: http://gco.iarc.fr

[20] International Agency for Research on Cancer. [Accessed on 2020-03-14]. [Online]. Available: https://www.iarc.fr/

[21] S. Shapiro, P. Strax, and L. Venet, "Periodic breast cancer screening in reducing mortality from breast cancer," *Jama*, vol. 215, no. 11, pp. 1777–1785, 1971.

[22] L. Tabár, A. Gad, L. Holmberg, U. Ljungquist, K. C. P. Group, C. Fagerberg, L. Baldetorp, O. Gröntoft, B. Lundström, J. Månson *et al.*, "Reduction in mortality from breast cancer after mass screening with mammography: randomised trial from the breast cancer screening working group of the swedish national board of health and welfare," *The Lancet*, vol. 325, no. 8433, pp. 829–832, 1985.

[23] L. Tabár, B. Vitak, H.-H. Chen, S. W. Duffy, M.-F. Yen, C.-F. Chiang, U. B. Krusemo, T. Tot, and R. A. Smith, "The swedish two-county trial twenty years later: updated mortality results and new insights from long-term follow-up," *Radiologic Clinics of North America*, vol. 38, no. 4, pp. 625–651, 2000.

[24] Swedish Organised Service Screening Evaluation Group, "Reduction in breast cancer mortality from organized service screening with mammography: 1. Further confirmation with extended data," *Cancer Epidemiology Biomarkers & Prevention*, vol. 15, no. 1, p. 45, 2006.

[25] L. Tabár and P. B. Dean, "A new era in the diagnosis and treatment of breast cancer," *The Breast Journal*, vol. 16, pp. S2–S4, 2010.

[26] L. Nyström, S. Wall, L. Rutqvist, A. Lindgren, M. Lindqvist, S. Rydén, J. Andersson, N. Bjurstam, G. Fagerberg, J. Frisell *et al.*, "Breast cancer screening with mammography: overview of swedish randomised trials," *The Lancet*, vol. 341, no. 8851, pp. 973–978, 1993.

[27] R. Rahim, M. J. Michell, V. Londero, C. Zuiani, M. Zanotel, M. Bazzocchi, and C. K. Kuhl, "Innovation in breast cancer radiology," in *Breast Cancer*. Cham, Switzerland: Springer International Publishing, 2017, pp. 205–246.

[28] Canadian Cancer Society. [Accessed on 2018-11-15]. [Online]. Available: http://www.cancer.ca/en/cancer-information/diagnosis-and-treatment/tests-and-procedures/mammography/?region=on

[29] R. D. Rosenberg, W. C. Hunt, M. R. Williamson, F. D. Gilliland, P. W. Wiest, C. A. Kelsey, C. R. Key, and M. N. Linver, "Effects of age, breast density, ethnicity, and estrogen replacement therapy on screening mammographic sensitivity and cancer stage at diagnosis: review of 183,134 screening mammograms in albuquerque, new mexico." *Radiology*, vol. 209, no. 2, pp. 511–518, 1998.

[30] W. A. Berg, L. Gutierrez, M. S. NessAiver, W. B. Carter, M. Bhargavan, R. S. Lewis, and O. B. Ioffe, "Diagnostic accuracy of mammography, clinical examination, US, and MR imaging in preoperative assessment of breast cancer," *Radiology*, vol. 233, no. 3, pp. 830–849, 2004.

[31] S. A. Huettel, A. W. Song, and G. McCarthy, *Functional magnetic resonance imaging*. Sunderland, MA: Sinauer Associates, 2004.

[32] American Cancer Society. [Accessed on 2020-12-17]. [Online]. Available: https://www.cancer.org/cancer/breast-cancer/screening-tests-and-early-detection/breast-mri-scans.html

[33] D. M. Ikeda, D. R. Baker, and B. L. Daniel, "Magnetic resonance imaging of breast cancer: clinical indications and breast MRI reporting system," *Journal of Magnetic Resonance Imaging*, vol. 12, no. 6, pp. 975–983, 2000.

[34] M. A. Perazella, "Gadolinium-contrast toxicity in patients with kidney disease: nephrotoxicity and nephrogenic systemic fibrosis," *Current Drug Safety*, vol. 3, no. 1, pp. 67–75, 2008.

[35] S. G. Orel, M. H. Mendonca, C. Reynolds, M. D. Schnall, L. J. Solin, and D. C. Sullivan, "MR imaging of ductal carcinoma in situ." *Radiology*, vol. 202, no. 2, pp. 413–420, 1997.

[36] S. G. Orel and M. D. Schnall, "MR imaging of the breast for the detection, diagnosis, and staging of breast cancer," *Radiology*, vol. 220, no. 1, pp. 13–30, 2001.

[37] C. M. Sehgal, S. P. Weinstein, P. H. Arger, and E. F. Conant, "A review of breast ultrasound," *Journal of Mammary Gland Biology and Neoplasia*, vol. 11, no. 2, pp. 113–123, 2006.

[38] W. A. Berg, J. D. Blume, J. B. Cormack, E. B. Mendelson, D. Lehrer, M. Böhm-Vélez, E. D. Pisano, R. A. Jong, W. P. Evans, M. J. Morton *et al.*, "Combined screening with ultrasound and mammography vs mammography alone in women at elevated risk of breast cancer," *Jama*, vol. 299, no. 18, pp. 2151–2163, 2008.

[39] E. Seeram, *Computed tomography: physical principles, clinical applications, and quality control*. St. Louis, MO: Elsevier, 2016.

[40] O. Humbert, A. Cochet, B. Coudert, A. Berriolo-Riedinger, S. Kanoun, F. Brunotte, and P. Fumoleau, "Role of positron emission tomography for the monitoring of response to therapy in breast cancer," *The Oncologist*, vol. 20, no. 2, p. 94, 2015.

[41] J. L. Vercher-Conejero, L. Pelegrí-Martinez, D. Lopez-Aznar, and M. D. P. Cózar-Santiago, "Positron emission tomography in breast cancer," *Diagnostics*, vol. 5, no. 1, pp. 61–83, 2015.

[42] G. Paganelli, F. Matteucci, and L. Gilardi, "Nuclear medicine in the clinical management (ROLL, SNB, and PET)," in *Breast Cancer*. Cham, Switzerland: Springer International Publishing, 2017, pp. 247–264.

[43] M. Pastorino, *Microwave imaging*. Hoboken, NJ: John Wiley & Sons, 2010.

[44] P. M. Meaney, M. W. Fanning, D. Li, S. P. Poplack, and K. D. Paulsen, "A clinical prototype for active microwave imaging of the breast," *IEEE Transactions on Microwave Theory and Techniques*, vol. 48, no. 11, pp. 1841–1853, 2000.

[45] X. Li and S. C. Hagness, "A confocal microwave imaging algorithm for breast cancer detection," *IEEE Microwave and Wireless Components Letters*, vol. 11, no. 3, pp. 130–132, 2001.

[46] E. C. Fear, J. Bourqui, C. Curtis, D. Mew, B. Docktor, and C. Romano, "Microwave breast imaging with a monostatic radar-based system: A study of application to patients," *IEEE Transactions on Microwave Theory and Techniques*, vol. 61, no. 5, pp. 2119–2128, 2013.

[47] S. Y. Semenov and D. R. Corfield, "Microwave tomography for brain imaging: Feasibility assessment for stroke detection," *International Journal of Antennas and Propagation*, vol. 2008, 2008, Art. no. 254830.

[48] M. Persson, A. Fhager, H. D. Trefná, Y. Yu, T. McKelvey, G. Pegenius, J.-E. Karlsson, and M. Elam, "Microwave-based stroke diagnosis making global prehospital thrombolytic treatment possible," *IEEE Transactions on Biomedical Engineering*, vol. 61, no. 11, pp. 2806–2817, 2014.

[49] J. Ljungqvist, S. Candefjord, M. Persson, L. Jönsson, T. Skoglund, and M. Elam, "Clinical evaluation of a microwave-based device for detection of traumatic intracranial hemorrhage," *Journal of Neurotrauma*, vol. 34, no. 13, pp. 2176–2182, 2017.

[50] L. E. Larsen and J. H. Jacobi, "Microwave scattering parameter imagery of an isolated canine kidney," *Medical Physics*, vol. 6, no. 5, pp. 394–403, 1979.

[51] S. Y. Semenov, A. E. Bulyshev, V. G. Posukh, Y. E. Sizov, T. C. Williams, and A. E. Souvorov, "Microwave tomography for detection/imaging of myocardial infarction. i. excised canine hearts," *Annals of Biomedical Engineering*, vol. 31, no. 3, pp. 262–270, 2003.

[52] P. M. Meaney, D. Goodwin, A. H. Golnabi, T. Zhou, M. Pallone, S. D. Geimer, G. Burke, and K. D. Paulsen, "Clinical microwave tomographic imaging of the calcaneus: A first-in-human case study of two subjects," *IEEE Transactions on Biomedical Engineering*, vol. 59, no. 12, pp. 3304–3313, 2012.

[53] B. R. Spies and T. M. Habashy, "Sensitivity analysis of crosswell electromagnetics," *Geophysics*, vol. 60, no. 3, pp. 834–845, 1995.

[54] V. Mikhnev and P. Vainikainen, "Microwave imaging of layered structures in civil engineering," in *2002 32nd European Microwave Conference*, Sept 2002, pp. 1–4.

[55] A. J. Bahr, "Nondestructive microwave evaluation of ceramics," *IEEE Transactions on Microwave Theory and Techniques*, vol. 26, no. 9, pp. 676–683, 1978.

[56] L. E. Larsen and J. H. Jacobi, "Medical applications of microwave imaging," IEEE Press, New York, Tech. Rep., 1985.

[57] N. K. Nikolova, "Microwave imaging for breast cancer," *IEEE Microwave Magazine*, vol. 12, no. 7, pp. 78–94, 2011.

[58] H. Kanj and M. Popovic, "A novel ultra-compact broadband antenna for microwave breast tumor detection," *Progress In Electromagnetics Research*, vol. 86, pp. 169–198, 2008.

[59] R. K Amineh, A. Trehan, and N. K. Nikolova, "TEM horn antenna for ultra-wide band microwave breast imaging," *Progress In Electromagnetics Research*, vol. 13, pp. 59–74, 2009.

[60] A. W. Preece, I. Craddock, M. Shere, L. Jones, and H. L. Winton, "MARIA M4: clinical evaluation of a prototype ultrawideband radar scanner for breast cancer detection," *Journal of Medical Imaging*, vol. 3, no. 3, p. 033502, 2016.

[61] E. Porter, M. Coates, and M. Popović, "An early clinical study of time-domain microwave radar for breast health monitoring," *IEEE Transactions on Biomedical Engineering*, vol. 63, no. 3, pp. 530–539, 2016.

[62] A. Fasoula, L. Duchesne, J. Gil Cano, P. Lawrence, G. Robin, and J.-G. Bernard, "On-site validation of a microwave breast imaging system, before first patient study," *Diagnostics*, vol. 8, no. 3, p. 53, 2018.

[63] R. K. Amineh, A. Khalatpour, H. Xu, Y. Baskharoun, and N. K. Nikolova, "Three-dimensional near-field microwave holography for tissue imaging," *International Journal of Biomedical Imaging*, vol. 2012, 2012, Art. no. 291494.

[64] D. M. Sheen, D. L. McMakin, and T. E. Hall, "Three-dimensional millimeter-wave imaging for concealed weapon detection," *IEEE Transactions on Microwave Theory and Techniques*, vol. 49, no. 9, pp. 1581–1592, 2001.

[65] R. K. Amineh, M. Ravan, A. Khalatpour, and N. K. Nikolova, "Three-dimensional near-field microwave holography using reflected and transmitted signals," *IEEE Transactions on Antennas and Propagation*, vol. 59, no. 12, pp. 4777–4789, 2011.

[66] M. Slaney, A. C. Kak, and L. E. Larsen, "Limitations of imaging with first-order diffraction tomography," *IEEE Transactions on Microwave Theory and Techniques*, vol. 32, no. 8, pp. 860–874, 1984.

[67] J. C. Bolomey, C. Pichot, and G. Garboriaud, "Planar microwave imaging camera for biomedical applications: Critical and prospective analysis of reconstruction algorithms," *Radio Science*, vol. 26, no. 2, pp. 541–549, 1991.

[68] L. Jofre, M. S. Hawley, A. Broquetas, E. de Los Reyes, M. Ferrando, and A. R. Elias-Fuste, "Medical imaging with a microwave tomographic scanner," *IEEE Transactions on Biomedical Engineering*, vol. 37, no. 3, pp. 303–312, 1990.

[69] P. M. Meaney, M. W. Fanning, R. M. di Florio-Alexander, P. A. Kaufman, S. D. Geimer, T. Zhou, and K. D. Paulsen, "Microwave tomography in the context of complex breast cancer imaging," in *2010 Annual International Conference of the IEEE Engineering in Medicine and Biology*, Sept. 2010, pp. 3398–3401.

[70] S. Y. Semenov, A. E. Bulyshev, A. E. Souvorov, R. H. Svenson, Y. E. Sizov, V. Vorisov, V. G. Posukh, I. M. Kozlov, A. G. Nazarov, and G. P. Tatsis, "Microwave tomography: Theoretical and experimental investigation of the iteration reconstruction algorithm," *IEEE Transactions on Microwave Theory and Techniques*, vol. 46, no. 2, pp. 133–141, 1998.

[71] S. Chaudhary, "Dielectric properties of normal and malignant human breast tissues at radiowave and microwave frequencies," *Indian Journal of Biochemistry & Biophysics*, vol. 21, pp. 76–79, 1984.

[72] S. Y. Semenov, A. E. Bulyshev, A. Abubakar, V. G. Posukh, Y. E. Sizov, A. E. Souvorov, P. M. van den Berg, and T. C. Williams, "Microwave-tomographic imaging of the high dielectric-contrast objects using different image-reconstruction approaches," *IEEE Transactions on Microwave Theory and Techniques*, vol. 53, no. 7, pp. 2284–2294, 2005.

[73] T. M. Grzegorczyk, P. M. Meaney, P. A. Kaufman, K. D. Paulsen *et al.*, "Fast 3-D tomographic microwave imaging for breast cancer detection," *IEEE Transactions on Medical Imaging*, vol. 31, no. 8, pp. 1584–1592, 2012.

[74] A. J. Surowiec, S. S. Stuchly, J. R. Barr, and A. Swarup, "Dielectric properties of breast carcinoma and the surrounding tissues," *IEEE Transactions on Biomedical Engineering*, vol. 35, no. 4, pp. 257–263, 1988.

[75] A. Campbell and D. Land, "Dielectric properties of female human breast tissue measured in vitro at 3.2 GHz," *Physics in Medicine & Biology*, vol. 37, no. 1, p. 193, 1992.

[76] W. T. Joines, Y. Zhang, C. Li, and R. L. Jirtle, "The measured electrical properties of normal and malignant human tissues from 50 to 900 MHz," *Medical Physics*, vol. 21, no. 4, pp. 547–550, 1994.

[77] J. W. Choi, J. Cho, Y. Lee, J. Yim, B. Kang, K. K. Oh, W. H. Jung, H. J. Kim, C. Cheon, H.-D. Lee *et al.*, "Microwave detection of metastasized breast cancer cells in the lymph node; potential application for sentinel lymphadenectomy," *Breast Cancer Research and Treatment*, vol. 86, no. 2, pp. 107–115, 2004.

[78] A. Martellosio, M. Pasian, M. Bozzi, L. Perregrini, A. Mazzanti, F. Svelto, P. Summers, G. Renne, and M. Bellomi, "0.5–50 GHz dielectric characterisation of breast cancer tissues," *Electronics Letters*, vol. 51, no. 13, pp. 974–975, 2015.

[79] A. Martellosio, M. Pasian, M. Bozzi, L. Perregrini, A. Mazzanti, F. Svelto, P. E. Summers, G. Renne, L. Preda, and M. Bellomi, "Dielectric properties characterization from 0.5 to 50 GHz of breast cancer tissues," *IEEE Transactions on Microwave Theory and Techniques*, vol. 65, no. 3, pp. 998–1011, 2016.

[80] T. Sugitani, S.-i. Kubota, S.-i. Kuroki, K. Sogo, K. Arihiro, M. Okada, T. Kadoya, M. Hide, M. Oda, and T. Kikkawa, "Complex permittivities of breast tumor tissues obtained from cancer surgeries," *Applied Physics Letters*, vol. 104, no. 25, p. 253702, 2014.

[81] M. Hussein, F. Awwad, D. Jithin, H. El Hasasna, K. Athamneh, and R. Iratni, "Breast cancer cells exhibits specific dielectric signature in vitro using the open-ended coaxial probe technique from 200 MHz to 13.6 GHz," *Scientific Reports*, vol. 9, no. 1, pp. 1–8, 2019.

[82] T. Rydholm, *Experimental Evaluation of a Microwave Tomography System for Breast Cancer Detection.* Licentiate dissertation, Chalmers University of Technology, 2018.

[83] A. Taflove and S. C. Hagness, *Computational electrodynamics: the finite-difference time-domain method.* Norwood, MA: Artech House, 2005.

[84] A. Fhager, *Microwave tomography.* Ph.D. dissertation, Chalmers University of Technology, 2006.

[85] S. C. Hagness, A. Taflove, and J. E. Bridges, "Two-dimensional FDTD analysis of a pulsed microwave confocal system for breast cancer detection: Fixed-focus and antenna-array sensors," *IEEE Transactions on Biomedical Engineering*, vol. 45, no. 12, pp. 1470–1479, 1998.

[86] ——, "Three-dimensional FDTD analysis of a pulsed microwave confocal system for breast cancer detection: Design of an antenna-array element," *IEEE Transactions on Antennas and Propagation*, vol. 47, no. 5, pp. 783–791, 1999.

[87] M. Popovic, S. C. Hagness, A. Taflove, and J. Bridges, "2-D FDTD study of fixed-focus elliptical reflector system for breast cancer detection: Frequency window for optimum operation," in *IEEE Antennas and Propagation Society International Symposium. 1998 Digest. Antennas: Gateways to the Global Network. Held in conjunction with: USNC/URSI National Radio Science Meeting (Cat. No. 98CH36)*, vol. 4, 1998, pp. 1992–1995.

[88] M. Gustafsson and S. He, "An optimization approach to two-dimensional time domain electromagnetic inverse problems," *Radio Science*, vol. 35, no. 2, pp. 525–536, 2000.

[89] S. Nordebo, A. Fhager, M. Gustafsson, and M. Persson, "A systematic approach to robust preconditioning for gradient-based inverse scattering algorithms," *Inverse Problems*, vol. 24, no. 2, p. 025027, 2008.

[90] D. Kurrant and E. Fear, "Defining regions of interest for microwave imaging using near-field reflection data," *IEEE Transactions on Microwave Theory and Techniques*, vol. 61, no. 5, pp. 2137–2145, 2013.

[91] G. Bindu and S. Semenov, "2D fused image reconstruction approach for microwave tomography: a theoretical assessment using the FDTD model," *Computer Methods in Biomechanics and Biomedical Engineering: Imaging & Visualization*, vol. 1, no. 3, pp. 147–154, 2013.

[92] D. R. Lynch, *Numerical partial differential equations for environmental scientists and engineers: a first practical course.* New York: Springer Science & Business Media, 2004.

[93] K. D. Paulsen, P. M. Meaney, M. J. Moskowitz, and J. M. Sullivan, "A dual mesh scheme for finite element based reconstruction algorithms," *IEEE Transactions on Medical Imaging*, vol. 14, no. 3, pp. 504–514, 1995.

[94] A. Abbosh, B. Mohammed, and K. Bialkowski, "Differential microwave imaging of the breast pair," *IEEE Antennas and Wireless Propagation Letters*, vol. 15, pp. 1434–1437, 2015.

[95] M. Jalilvand, X. Li, L. Zwirello, and T. Zwick, "Ultra wideband compact near-field imaging system for breast cancer detection," *IET Microwaves, Antennas & Propagation*, vol. 9, no. 10, pp. 1009–1014, 2015.

[96] E. A. Aydın and M. Kaya Keleş, "Breast cancer detection using K-nearest neighbors data mining method obtained from the bow-tie antenna dataset," *International Journal of RF and Microwave Computer-Aided Engineering*, vol. 27, no. 6, p. e21098, 2017.

[97] H. DeVoe, "Optical properties of molecular aggregates. I. Classical model of electronic absorption and refraction," *The Journal of Chemical Physics*, vol. 41, no. 2, pp. 393–400, 1964.

[98] E. M. Purcell and C. R. Pennypacker, "Scattering and absorption of light by nonspherical dielectric grains," *The Astrophysical Journal*, vol. 186, pp. 705–714, 1973.

[99] B. T. Draine, "The discrete-dipole approximation and its application to interstellar graphite grains," *The Astrophysical Journal*, vol. 333, pp. 848–872, 1988.

[100] B. T. Draine and J. Goodman, "Beyond Clausius-Mossotti-Wave propagation on a polarizable point lattice and the discrete dipole approximation," *The Astrophysical Journal*, vol. 405, pp. 685–697, 1993.

[101] B. T. Draine and P. J. Flatau, "Discrete-dipole approximation for scattering calculations," *Journal of the Optical Society of America A*, vol. 11, no. 4, pp. 1491–1499, 1994.

[102] P. Flatau and B. T. Draine, "Fast near field calculations in the discrete dipole approximation for regular rectilinear grids," *Optics Express*, vol. 20, no. 2, pp. 1247–1252, 2012.

[103] DDSCAT, light scattering code. [Accessed on 2020-12-23]. [Online]. Available: http://ddscat.wikidot.com/

[104] M. A. Yurkin, V. P. Maltsev, and A. G. Hoekstra, "Convergence of the discrete dipole approximation. I. Theoretical analysis," *Journal of the Optical Society of America A*, vol. 23, no. 10, pp. 2578–2591, 2006.

[105] ——, "Convergence of the discrete dipole approximation. II. An extrapolation technique to increase the accuracy," *Journal of the Optical Society of America A*, vol. 23, no. 10, pp. 2592–2601, 2006.

[106] ——, "The discrete dipole approximation for simulation of light scattering by particles much larger than the wavelength," *Journal of Quantitative Spectroscopy and Radiative Transfer*, vol. 106, no. 1-3, pp. 546–557, 2007.

[107] M. A. Yurkin and A. G. Hoekstra, "The discrete-dipole-approximation code adda: capabilities and known limitations," *Journal of Quantitative Spectroscopy and Radiative Transfer*, vol. 112, no. 13, pp. 2234–2247, 2011.

[108] ——, "The discrete dipole approximation: an overview and recent developments," *Journal of Quantitative Spectroscopy and Radiative Transfer*, vol. 106, no. 1-3, pp. 558–589, 2007.

[109] M. A. Yurkin, *Discrete dipole simulations of light scattering by blood cells*. Ph.D. dissertation, University of Amsterdam, 2007.

[110] A. Lakhtakia, "Strong and weak forms of the method of moments and the coupled dipole method for scattering of time-harmonic electromagnetic fields," *International Journal of Modern Physics C*, vol. 3, no. 03, pp. 583–603, 1992.

[111] F. M. Kahnert, "Numerical methods in electromagnetic scattering theory," *Journal of Quantitative Spectroscopy and Radiative Transfer*, vol. 79, pp. 775–824, 2003.

[112] C. A. Balanis, *Advanced engineering electromagnetics*. Hoboken, NJ: John Wiley & Sons, 2012.

[113] W. C. Gibson, *The method of moments in electromagnetics*. Boca Raton, FL: Chapman and Hall/CRC, 2007.

[114] P. W. Atkins and J. De Paula, *Physical Chemistry*. Oxford, UK: Oxford University Press, 2006.

[115] R. R. Pethig, *Dielectrophoresis: Theory, methodology and biological applications*. Hoboken, NJ: John Wiley & Sons, 2017.

[116] A. Rahmani, P. C. Chaumet, and G. W. Bryant, "On the importance of local-field corrections for polarizable particles on a finite lattice: application to the discrete dipole approximation," *The Astrophysical Journal*, vol. 607, no. 2, p. 873, 2004.

[117] V. A. Markel, "Maxwell Garnett approximation (advanced topics): tutorial," *Journal of the Optical Society of America A*, vol. 33, no. 11, pp. 2237–2255, 2016.

[118] A. Sihvola, "Mixing rules with complex dielectric coefficients," *Subsurface Sensing Technologies and Applications*, vol. 1, no. 4, pp. 393–415, 2000.

[119] A. H. Sihvola, "Peculiarities in the dielectric response of negative-permittivity scatterers," *Progress In Electromagnetics Research*, vol. 66, pp. 191–198, 2006.

[120] J. Steffan and K. Richter, "A numerical verification of the Clausius-Mossotti relation," *IEEE Transactions on Magnetics*, vol. 26, no. 2, pp. 528–531, 1990.

[121] L. N. Trefethen and D. Bau III, *Numerical linear algebra*. Philadelphia: SIAM, 1997.

[122] M. Clemens and T. Weiland, "Iterative methods for the solution of very large complex symmetric linear systems of equations in electrodynamics," Front Range Scientific Computations, Lakewood, CO, Tech. Rep., 1996.

[123] H. A. van der Vorst and J. B. Melissen, "A Petrov-Galerkin type method for solving Ax=b, where A is symmetric complex," *IEEE Transactions on Magnetics*, vol. 26, no. 2, pp. 706–708, 1990.

[124] T. Sogabe and S.-L. Zhang, "A COCR method for solving complex symmetric linear systems," *Journal of Computational and Applied Mathematics*, vol. 199, no. 2, pp. 297–303, 2007.

[125] R. W. Freund, "Conjugate gradient-type methods for linear systems with complex symmetric coefficient matrices," *SIAM Journal on Scientific and Statistical Computing*, vol. 13, no. 1, pp. 425–448, 1992.

[126] Y. Saad, *Iterative methods for sparse linear systems*. Philadelphia: SIAM, 2003.

[127] M. Benzi, "Preconditioning techniques for large linear systems: a survey," *Journal of Computational Physics*, vol. 182, no. 2, pp. 418–477, 2002.

[128] O. Axelsson, "A generalized SSOR method," *BIT Numerical Mathematics*, vol. 12, no. 4, pp. 443–467, 1972.

[129] T. Kailath and A. H. Sayed, *Fast reliable algorithms for matrices with structure*. Philadelphia: SIAM, 1999.

[130] M. Frigo and S. G. Johnson, "The design and implementation of FFTW3," *Proceedings of the IEEE*, vol. 93, no. 2, pp. 216–231, 2005.

[131] J. Hadamard, *Lectures on Cauchy's Problem in Linear Partial Differential Equations*. New Haven, CT: Yale University Press, 1923.

[132] D. Colton and R. Kress, *Inverse acoustic and electromagnetic scattering theory*. New York: Springer Science & Business Media, 2012.

[133] R. C. Conceição, J. J. Mohr, and M. O'Halloran, Eds., *An introduction to microwave imaging for breast cancer detection*. Cham, Switzerland: Springer International Publishing, 2016.

[134] M. Born and E. Wolf, *Principles of optics: electromagnetic theory of propagation, interference and diffraction of light*. Cambridge, UK: Cambridge University Press, 1999.

[135] W. C. Chew and Y.-M. Wang, "Reconstruction of two-dimensional permittivity distribution using the distorted born iterative method," *IEEE Transactions on Medical Imaging*, vol. 9, no. 2, pp. 218–225, 1990.

[136] S. Noghanian, A. Sabouni, T. Desell, and A. Ashtari, *Microwave Tomography*. New York: Springer Science & Business Media, 2014.

[137] P. M. Van Den Berg and R. E. Kleinman, "A contrast source inversion method," *Inverse Problems*, vol. 13, no. 6, p. 1607, 1997.

[138] P. Van den Berg, "Nonlinear scalar inverse scattering: algorithms and applications," in *Scattering*. London: Academic Press, 2002, pp. 142–161.

[139] P. E. Gill, W. Murray, and M. H. Wright, *Practical optimization*. London: Academic Press, 1981.

[140] J. M. Ortega and W. C. Rheinboldt, *Iterative solution of nonlinear equations in several variables*. Philadelphia: SIAM, 2000.

[141] T. Rubæk, P. M. Meaney, P. Meincke, and K. D. Paulsen, "Nonlinear microwave imaging for breast-cancer screening using Gauss–Newton's method and the CGLS inversion algorithm," *IEEE Transactions on Antennas and Propagation*, vol. 55, no. 8, pp. 2320–2331, 2007.

[142] J. H. Holland, "Genetic algorithms and adaptation," in *Adaptive Control of Ill-Defined Systems*. Boston: Springer, 1984, pp. 317–333.

[143] M. Wahde, *Biologically inspired optimization methods: an introduction*. Southampton, UK: WIT Press, 2008.

[144] R. Eberhart and J. Kennedy, "A new optimizer using particle swarm theory," in *MHS'95. Proceedings of the Sixth International Symposium on Micro Machine and Human Science*, 1995, pp. 39–43.

[145] S.-H. Son, N. Simonov, H.-J. Kim, J.-M. Lee, and S.-I. Jeon, "Preclinical prototype development of a microwave tomography system for breast cancer detection," *ETRI Journal*, vol. 32, no. 6, pp. 901–910, 2010.

[146] P. M. Meaney, Q. Fang, T. Rubaek, E. Demidenko, and K. D. Paulsen, "Log transformation benefits parameter estimation in microwave tomographic imaging," *Medical Physics*, vol. 34, no. 6, pp. 2014–2023, 2007.

[147] D. Constales, G. S. Yablonsky, D. R. D'hooge, J. W. Thybaut, and G. B. Marin, *Advanced data analysis and modelling in chemical engineering.* Amsterdam: Elsevier, 2016.

[148] N. Andreasson, M. Patriksson, and A. Evgrafov, *An introduction to continuous optimization: foundations and fundamental algorithms.* Stockholm: Studentlitteratur AB, 2013.

[149] P. M. Meaney, K. D. Paulsen, B. W. Pogue, and M. I. Miga, "Microwave image reconstruction utilizing log-magnitude and unwrapped phase to improve high-contrast object recovery," *IEEE Transactions on Medical Imaging*, vol. 20, no. 2, pp. 104–116, 2001.

[150] Q. Fang, P. M. Meaney, and K. D. Paulsen, "Viable three-dimensional medical microwave tomography: Theory and numerical experiments," *IEEE Transactions on Antennas and Propagation*, vol. 58, no. 2, pp. 449–458, 2010.

[151] M. Cocchi, *Data fusion methodology and applications.* Amsterdam: Elsevier, 2019.

[152] A. N. Tikhonov, "Solution of incorrectly formulated problems and the regularization method," *Soviet Mathematics Doklady*, vol. 4, pp. 1035–1038, 1963.

[153] N. Joachimowicz, C. Pichot, and J. P. Hugonin, "Inverse scattering: an iterative numerical method for electromagnetic imaging," *IEEE Transactions on Antennas and Propagation*, vol. 39, no. 12, pp. 1742–1753, 1991.

[154] A. Franchois and C. Pichot, "Microwave imaging-complex permittivity reconstruction with a Levenberg-Marquardt method," *IEEE Transactions on Antennas and Propagation*, vol. 45, no. 2, pp. 203–215, 1997.

[155] D. W. Marquardt, "An algorithm for least-squares estimation of nonlinear parameters," *Journal of the Society for Industrial and Applied Mathematics*, vol. 11, no. 2, pp. 431–441, 1963.

[156] Q. Fang, P. M. Meaney, and K. D. Paulsen, "The multidimensional phase unwrapping integral and applications to microwave tomographical image reconstruction," *IEEE Transactions on Image Processing*, vol. 15, no. 11, pp. 3311–3324, 2006.

[157] P. M. Meaney, S. D. Geimer, and K. D. Paulsen, "Two-step inversion with a logarithmic transformation for microwave breast imaging," *Medical Physics*, vol. 44, no. 8, pp. 4239–4251, 2017.

[158] T. M. Grzegorczyk, P. M. Meaney, S. I. Jeon, S. D. Geimer, and K. D. Paulsen, "Importance of phase unwrapping for the reconstruction of microwave tomographic images," *Biomedical Optics Express*, vol. 2, no. 2, pp. 315–330, 2011.

[159] C. Pichot, L. Jofre, G. Peronnet, and J. Bolomey, "Active microwave imaging of inhomogeneous bodies," *IEEE Transactions on Antennas and Propagation*, vol. 33, no. 4, pp. 416–425, 1985.

[160] T. Sugitani, S. Kubota, A. Toya, X. Xiao, and T. Kikkawa, "A compact 4×4 planar UWB antenna array for 3-D breast cancer detection," *IEEE Antennas and Wireless Propagation Letters*, vol. 12, pp. 733–736, 2013.

[161] H. Song, S. Sasada, T. Kadoya, M. Okada, K. Arihiro, X. Xiao, and T. Kikkawa, "Detectability of breast tumor by a hand-held impulse-radar detector: performance evaluation and pilot clinical study," *Scientific Reports*, vol. 7, no. 1, pp. 1–11, 2017.

[162] T. Rydholm, A. Fhager, M. Persson, and P. M. Meaney, "A first evaluation of the realistic Supelec-breast phantom," *IEEE Journal of Electromagnetics, RF and Microwaves in Medicine and Biology*, vol. 1, no. 2, pp. 59–65, 2017.

[163] S. P. Rana, M. Dey, G. Tiberi, L. Sani, A. Vispa, G. Raspa, M. Duranti, M. Ghavami, and S. Dudley, "Machine learning approaches for automated lesion detection in microwave breast imaging clinical data," *Scientific Reports*, vol. 9, no. 1, pp. 1–12, 2019.

[164] T. Rydholm, A. Fhager, M. Persson, S. Geimer, and P. Meaney, "Effects of the plastic of the realistic GeePS-L2S-breast phantom," *Diagnostics*, vol. 8, no. 3, p. 61, 2018.

[165] P. M. Meaney, C. J. Fox, S. D. Geimer, and K. D. Paulsen, "Electrical characterization of glycerin: Water mixtures: Implications for use as a coupling medium in microwave tomography," *IEEE Transactions on Microwave Theory and Techniques*, vol. 65, no. 5, pp. 1471–1478, 2017.

[166] N. Joachimowicz, C. Conessa, T. Henriksson, and B. Duchêne, "Breast phantoms for microwave imaging," *IEEE Antennas and Wireless Propagation Letters*, vol. 13, pp. 1333–1336, 2014.

[167] M. Habibi, D. P. Klemer, and V. Raicu, "Two-dimensional dielectric spectroscopy: Implementation and validation of a scanning open-ended coaxial probe," *Review of Scientific Instruments*, vol. 81, no. 7, p. 075108, 2010.

[168] J. Garrett and E. Fear, "Stable and flexible materials to mimic the dielectric properties of human soft tissues," *IEEE Antennas and Wireless Propagation Letters*, vol. 13, pp. 599–602, 2014.

[169] P. M. Meaney, K. D. Paulsen, S. D. Geimer, S. A. Haider, and M. W. Fanning, "Quantification of 3-D field effects during 2-D microwave imaging," *IEEE Transactions on Biomedical Engineering*, vol. 49, no. 7, pp. 708–720, 2002.